Materials Technology Reports

https://ojs.acad-pub.com/index.php/MTR

2023 VOLUME 1 ISSUE 1
ISSN: 3029-2646 (Online)

1

Editorial Board

Editor-in-Chief

Editorial Board Member

Volume 1 Issue 1 • 2023

Materials Technology Reports

ACADEMIC
ACADEMIC PUBLISHING PTE LTD

2023 | Volume 1 | Issue 1

Materials Technology Reports

https://ojs.acad-pub.com/index.php/MTR

Contents

Original Research Articles

1 **Manganese and iron-doped yttrium borate as an excellent multifunctional inorganic material**
Pankaj Gupta1, Mohit Sahni

14 **Effect of the welding procedure on the deformation of superposed welds of a low carbon steel**
Rafael Humberto Mota de Siqueira, Sheila Medeiros de Carvalho, Milton Sergio Fernandes de Lima

23 **Examination of surface contamination and impurities in tinplate samples, both passivated and non-passivated**
Amirhossein Meysami, Reza Amini Najafabadi, Ehsan Nemati Varnoosfaderani, Erfan Aghili, Aliasghar Foroughifar

35 **Effects of pyrolyzed Buxus sempervirens ingredient as micro and bio fillers on polystyrene: Spectroscopic characteristics**
Hamed Nazarpour Fard

Review Articles

42 **A brief review on systematic approach to polymer selection for development of capillary/hollow-fibre membrane for practical applications**
Vijay Suresh Mamtani, Asim Kumar Ghosh, Asis Kumar Adak

55 **From desolvation-induced self-organization on the MALDI anchor target chip surfaces to laser-induced self-organization in MALDI techniques: Correlation-spectral analysis and complex wavelet analysis of tesiographic spots on the anchor chips**
Theodor K. Orekhov, Oleg V. Gradov

65 **Reaction-diffusion effects and spatiotemporal oscillations under SEM, STM and AFM-assisted charging in fiber-like and wire-like systems: From molecular and quantum wires to cooperative ferroelectric nanofibers and microfibers**
Eugene D. Adamovich, Eugenia L. Buryanskaya, Margaret A. Gradova, Oleg V. Gradov

Materials Technology Reports 2023; 1(1): 377.
Original Research Article

Manganese and iron-doped yttrium borate as an excellent multifunctional inorganic material

Pankaj Gupta[1,*,†], Mohit Sahni[2,*,†]

[1] *Department of Chemistry and Biochemistry, SBSR, Sharda University, Uttar Pradesh 201310, India*

[2] *Department of Physics, SBSR, Sharda University, Uttar Pradesh 201310, India*

*** Corresponding author:** Pankaj Gupta, pankaj.chemistry2019@gmail.com; Mohit Sahni, mohit.sahni@sharda.ac.in

† Both the authors have equal contribution.

ARTICLE INFO

Received: 24 September 2023
Accepted: 26 October 2023
Available online: 12 December 2023

doi: 10.59400/mtr.v1i1.377

ABSTRACT: Manganese and iron-doped π-YBO_3 have been synthesized using a modified epoxide-mediated gel method. The PXRD pattern evaluated the formation of the desired phase and the structural changes. EDS spectra determined the elemental analysis of undoped and doped samples. Raman spectra observed the stretching and bending modes of B-O bonds. The direct band gaps for doped samples were 1.47 and 2.07 eV, respectively, lower than the band gap value of 5.81 eV for π-YBO_3. The green and blue indigo emission bands were observed in the photoluminescence spectra. Doped samples showed good magnetic properties as they are antiferromagnetic and ferromagnetic at low temperature (T = 5 K) M-H plot and SQUID measurement. An indigenously built Sawyer-Tower circuit is used to measure ferroelectric hysteresis. Photodegradation studies of RhB were conducted under UV-visible irradiation.

KEYWORDS: borate; sol-gel; magnetic; photocatalytic; ferroelectric; phosphor

1. Introduction

Transition metal borates have recently attained enormous attention due to their significant properties and potential applications[1–3]. Transition metal borates can be classified into metal orthoborates and metal oxyborates. The metal-rich oxyborates, containing six coordinated metal ion of mixed valence and trigonal planar BO_3^{3-} unit, adopts two warwickite and pinakiolite type structure[4], and the metal: borate ratio of warwickite is 2:1. In contrast, pinakiolite type has a ratio of 3:1. The mixture of divalent and trivalent metal ions, the composition $M_2^{II}M^{III}OBO_3$ and $M_2^{II}M^{III}O_2BO_3$, where metals are iron, cobalt and manganese, can cause the formation of homometallic oxyborates and mixed valence in solid state. The known homometallic oxyborates are manganese oxyborates (Mn_2OBO_3 and $Mn_2^{II}Mn^{III}O_2BO_3$), iron oxyborates (Fe_2OBO_3 and $Fe_2^{II}Fe^{III}O_2BO_3$) and cobalt oxyborates (Co_2OBO_3 and $Co_2^{II}Co^{III}O_2BO_3$) which adopt warwickite and pinakiolite structure[4–7].

The name warwickite is applied to an unusual family of orthorhombic minerals having space group *Pnma* and ideal composition ($M_2O_3BO_3$ (M = Mn^{2+}, Fe^{3+}, Mg^{2+}, Ti^{4+}, and Al^{3+})), warwickite structure was first investigated by Takeuchi et al. in 1950 having composition $(Mg,Fe)_{1.5}Ti_{0.5}OBO_3$[4]. Mg_2InBO_5 belongs to the category of M_3BO_5, having a ludwigite structure with a space group of *Pbam*. The M_3BO_5 (where M can be divalent ions such as Mg^{2+}, Fe^{2+}, Co^{2+}, Ni^{2+} and Zn^{2+} or tri- and tetravalent ions as Al^{3+},

V^{3+}, Cr^{3+}, Mn^{3+}, Fe^{3+}, Ga^{3+}, Mn^{4+}, Sn^{4+}, Ge^{4+}, Zr^{4+} and Ti^{4+}) belongs to oxyborate family having ludwigite type structure has already been studied in the past. These all materials such that the cations (transition metal ions) are distributed over four crystallographic distinct octahedral sites, but in some cases, two different atoms can occupy the complementary sites[8,9]. Rare earth ortho-borates show excessive polymorphism, where most structures have explicitly been determined. The following is a survey of previous work[10–13]. Levin et al.[14] 1961 described the vaterite type- orthoborate π-$REBO_3$ (RE: Y, Nd, Sm-Lu). The structure of π-$REBO_3$ was proposed to be hexagonal with a coordination number greater than three. A new phase μ-YBO_3 was proposed, which was isostructural with vaterite form and possibly in a pseudohexagonal phase. Newnham et al.[15] considered two hexagonal structures of π-YBO_3, one distorted with the space group of $P6_3/mmc$ and the other ordered with a space group of $P6_3/mcm$). In both structures, rare earth ions were coordinated with eight oxygen atoms, forming a distorted cube. Spectroscopic techniques such as IR, NMR and Raman studies of π-*ortho-borates* confirmed the tetrahedral coordination of boron in the $B_3O_9^-$ ring[16–20]. The hexagonal space group $P6c2$ at low temperatures was proposed by Bradley et al.[21], and at high temperatures, it described the $P6_322$ space group. In 1977, the pseudohexagonal model for π-YBO_3 orthoborate was proposed by Morgan et al.[13], and it favoured the psuedowollastonite-type structure over the vaterite type. In 1997, Chadeyron et al.[22] restudied the structure of π-YBO_3 using single-crystal diffraction techniques where hexagonal cell, a = 3.776 Å and c = 8.806 Å with space group of $P6_3/m$ was observed. Ren et al.[23] introduced two other space groups for π- and μ-$REBO_3$, where π-YBO_3 was identified as a sub cell of a rhombohedral structure. In this way, a fully ordered structure in the rhombohedral space group $R32$ was accomplished. The study results of Cohen-Adad et al.[24] in 2000 were consistent with all possible hexagonal space groups $P6_3/mmc$, $P6c2$, $P6_3/mcm$ and $P6_3/m$, while the best agreement could be accounted for in $P6c2$. For μ-$GdBO_3$, hexagonal space group $P6_322$ was assumed. Lin et al.[12] surveyed the powder data of the $Y_{0.92}Er_{0.02}BO_3$ sample by neutron diffraction, and it was found that a monoclinic structure was observed with space group of $C2/c$ for both low- and high-temperature. In 2008, Hosokawa et al.[25] presented the space group $P6_3/m$ for orthoborate powder synthesized by gyrothermal reaction, which was previously determined by Chadeyron et al.[22]. We know that literature has yet to be published on doping transition metals in YBO_3. The use of the sol-gel process is quite beneficial for creating superior materials. The result of the sol-gel method is an improvement in the processing of traditional materials and their properties, as well as the synthesis of new materials. Due to its low-temperature nature, the organic-inorganic hybrids sol-gel technique is beneficial for creating high-performance liquid chromatography. The following benefits of the sol-gel technique are Easy procedure, the creation of highly pure products, the efficiency of synthesis is very high, more thorough surface coverage, the creation of low-cost and high-quality materials, etc.[26]. In the present study, transition metal doped YBO_3 has been synthesized by epoxide gel route. Following this, photoluminescence, magnetic, ferroelectric, and photocatalytic properties have been studied thoroughly. In the present study, transition metal doped YBO_3 has been synthesized by epoxide gel route. Following this, photoluminescence, magnetic, ferroelectric, and photocatalytic properties have been studied thoroughly.

2. Experimental

2.1. Synthesis

To synthesize π-YBO_3, $YCl_{3.6}H_2O$ (99.9%, Sigma Aldrich), H_3BO_3 (99.9%, BDH) and Propylene Oxide (99%, Alfa Aesar, Massachusetts) as the starting materials, we dissolved 0.3056 g (1 mmol) of $YCl_{3.6}H_2O$ in 5 mL of absolute ethanol and 0.061 g of H_3BO_3 (1 mmol), and constantly stirred the

mixture at room temperature. Then, we added 0.69 mL (10 mmol) of propylene oxide drop by drop while stirring the solution. After a few minutes of ultrasonication, the mixture produced a colourless xerogel. We calcined the samples in a muffle furnace at 900 ℃ for 4 h, with the heating rate set to 20 ℃/min. Finally, we allowed the samples to cool naturally to room temperature by turning off the furnace[27].

Use 0.0192 g (10 mmol) $MnCl_{2.4}H_2O$ (99%, Alfa Aesar), 0.0410 g (10 mmol) $Fe(NO_3)_{3.9}H_2O$ (98%, CDH), 0.281 g (0.9 mmol) $YCl_{3.6}H_2O$ and 0.061 g H_3BO_3 with 0.69 mL (10 mmol) of propylene oxide to produce xerogels of composition of $Y_{0.90}M_{0.10}BO_3$ (M = Mn^{2+} and Fe^{2+}) following the same procedure described for the synthesis of π-YBO_3.

2.2. Characterization

A high-resolution Bruker D-8 Advanced X-ray diffractometer was used to record the powder X-ray diffraction (PXRD) patterns. The obtained PXRD data was subjected to structure refinement via the Le Bail method, which used TOPAS3 software. Renishaw spectrometer was adopted to record the Raman spectra using a microscope system operating with an Nd: YAG laser (λ = 532 nm). Diffuse reflectance spectra were collected for the samples on a Perkin-Elmer Lambda-35 UV-visible spectrophotometer with an attached integrating sphere, taking $BaSO_4$ as the reference transformed to absorbance via selecting KM Function to perform this. The conventional excitation and emission spectral measurements of the samples were performed adopting Horiba Jobin Yvon Fluorolog-modular spectrofluorometer at room temperature with a continuing-wave xenon lamp source and Cary Eclipse Fluorescence Spectrophotometer G9800AA. Low-temperature magnetic measurements were recorded using MPMS (Magnetic Properties Measurement System) Excel manufacturing quantum design USA in temperatures ranging between 5 to 320 K under an applied field of ±1 Tesla. Magnetization measurements were performed using a vibrating sample magnetometer (Magnetic Properties Measurement System excel manufacturing quantum design USA) at 5 K and 300 K under an applied field of ±7 Tesla. An indigenously built Sawyer-Tower circuit was used to measure the ferroelectric hysteresis, and a lock-in amplifier drove the circuit. Further, a photodegradation study of dye molecules was done in the presence of a catalyst in an immersion type, in-house fabricated reactor under UV-visible radiation adopting a 125 W capacity mercury vapour lamp (Philips, India). A solid sample (50 mg) was added to a 10 μM aqueous solution of RhB (pH ~ 7) dye, formed by adopting double distilled water. Firstly, the suspension was stirred under the dark for almost 20 min to attain equilibrium, then turned on the UV-visible radiation and shined on the suspension. A 5–6 mL quantity of aliquots was withdrawn periodically from the reaction mixture. Then, solutions were centrifuged, and the concentration of the solution was obtained by measuring the absorbance at λmax = 556 nm for (Rh-B) using a UV-visible spectrometer (Shimadzu UV-1601).

PXRD patterns of 10% manganese and iron-doped π-YBO_3, were compared with those of pure π-YBO_3, in **Figure 1**. The xerogel is amorphous, and the calcined product exhibited reflections that matched well with hexagonal π-YBO_3, regarding position and intensity profile (JCPDS File No. 83-1205).

The PXRD pattern of this sample was successfully refined using the Le-Bail method in the $P6_3/m$ space group. The resulting lattice parameters were a = 3.7756 (15) and c = 8.8138 (25) with no uncounted reflections[15,16,22,25]. The crystallite size (D) was estimated to be 27 nm using Scherrer's formula D = 0.89 λ/βCosθ, (where λ is the wavelength of the X-ray, θ is the diffraction angle, and β is half peak width). The

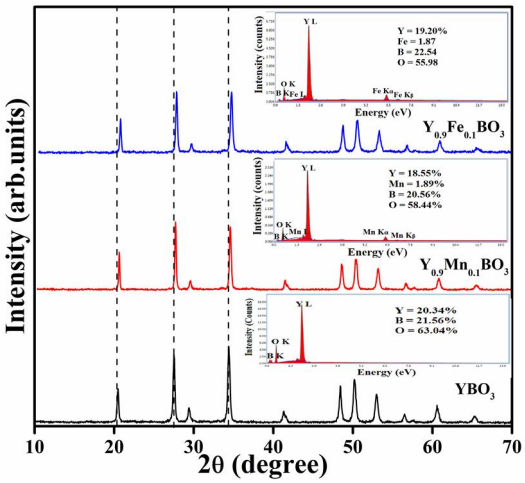

Figure 1. PXRD patterns of product calcination of xerogels from the attempts to make π-YBO_3, manganese and iron doped π-YBO_3, samples. Inset showing the EDS spectra.

doped samples showed peaks only about hexagonal π-YBO_3, with no additional reflections and a systematic shifting of the diffracted peaks toward higher 2θ values was observed. From the Le-Bail refinement of the PXRD pattern, we derived unit cell constants of a = 3.7701 (18) and c = 8.8025 (11) Å for the manganese-doped sample, a = 3.7616 (20) and c = 8.8011 (18) Å for the iron-doped sample (**Figure 2**). This suggests the inclusion of smaller-sized manganese (0.83 Å) and iron (0.78 Å) for Y^{3+} in six-fold coordination. The crystallite size of π-YBO_3, increased with the doping of transition metal ions, with crystallite sizes of 36 nm and 38 nm deduced for the manganese and iron-doped samples, respectively. EDS analysis of the π-YBO_3 sample showed that approximately 21%, 22%, and 63% of Y, B, and O were present in the sample, respectively, which was close to the expected ratio of 1:1:3. For the doped samples, 10% manganese and iron were confirmed to be present about the amount of yttrium.

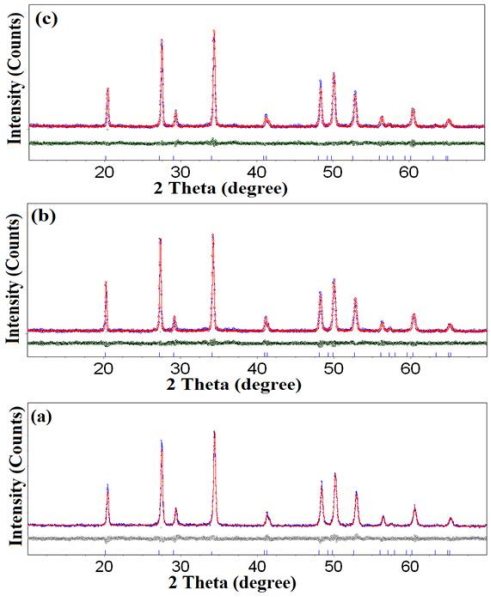

Figure 2. Le-Bail refinement of **(a)** π-YBO_3, **(b)** π-$Y_{0.90}Mn_{0.10}BO_3$ and **(c)** π-$Y_{0.90}Fe_{0.10}BO_3$.

Raman spectra of Mn^{2+} and Fe^{2+} doped π-YBO_3 samples have been compared with π-YBO_3, in **Figure 3**. Translations of Y^{3+}, B_3O_9 units and vibrational modes of B_3O_9 units within the structure contribute to the bands visible between 180 and 250 cm^{-1}. Moreover, the existence of B_3O_9 rings was

attributed to the bands present at 414 and 513 cm^{-1}. B-O-B bending of the BO_4 units and $B_3O_9^{9-}$ borate ring deformation modes were visible at 615 and 839 cm^{-1}. Stretching vibration of tetrahedral BO_4 groups exists as a part of the $B_3O_9^{9-}$ ring displayed as a band at 1006 cm^{-1}[27–29]. All the Raman peaks shifted toward lower values for Mn^{2+} and Fe^{2+} doped samples, confirming their incorporation.

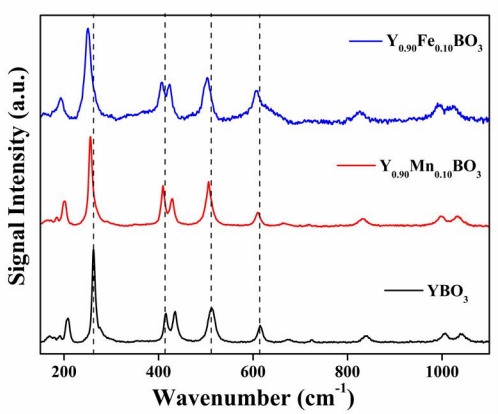

Figure 3. Raman spectra of undoped and doped π-YBO_3.

UV-visible spectra of Mn^{2+} and Fe^{2+} doped π-YBO_3 are presented in **Figure 4**. The band centred at 235, 360, 402 and 498 nm for the manganese doped samples corresponded to transitions from $^6A_{1g}$(S) to $^4A_{1g}$(F), $^4T_{2g}$(D), ^4E_g(D) and $^4T_{1g}$(G), respectively[30]. On the other hand, the broad band centred at 534 nm and 885 nm for the iron doped π-YBO_3 corresponded to $^5A \rightarrow {}^5E$ and $^6A_1 \rightarrow {}^4T_1$ (^4G) transitions of iron, respectively[31].

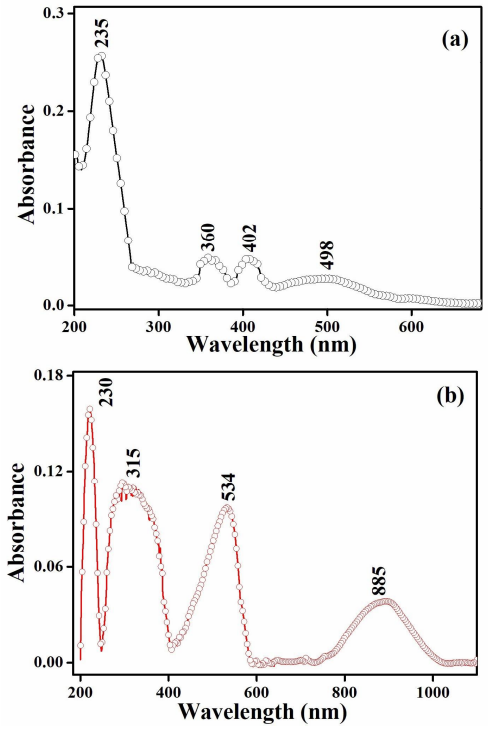

Figure 4. UV-visible spectra for (**a**) π-$Y_{0.90}Mn_{0.10}BO_3$ and (**b**) π-$Y_{0.90}Fe_{0.10}BO_3$.

The direct band gaps for Mn^{2+} and Fe^{2+} doped samples, calculated using Tauc plot $((\alpha h\nu)^2$ $(eV/cm)^2$ versus hν (eV)), were 1.47 and 2.07 eV, respectively. They were lower than the value of 5.81 eV for

π-YBO_3. Pure π-YBO_3 was off-white, whereas brown and reddish-brown colours were acquired by Mn^{2+} and Fe^{2+} doped samples (**Figure 5**). PL spectra of Mn^{2+} and Fe^{2+} doped π-YBO_3 have been presented in **Figure 6(a)**. Blue indigo emissions at 412, 438 and 454 nm were observed for the Fe^{2+} doped sample[32]. The green emission band in the region of 500 nm to 630 nm was assigned to the $^6A_{1g}$ (^6S) → $^4T_{1g}$ (^4G) transition of Mn^{2+} doped π-YBO_3[33].

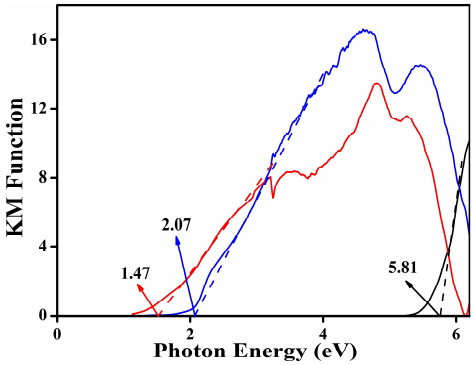

Figure 5. Bandgap estimation for π-YBO_3 (Black), π-$Y_{0.90}Mn_{0.10}BO_3$ (Red) and π-$Y_{0.90}Fe_{0.10}BO_3$ (Blue).

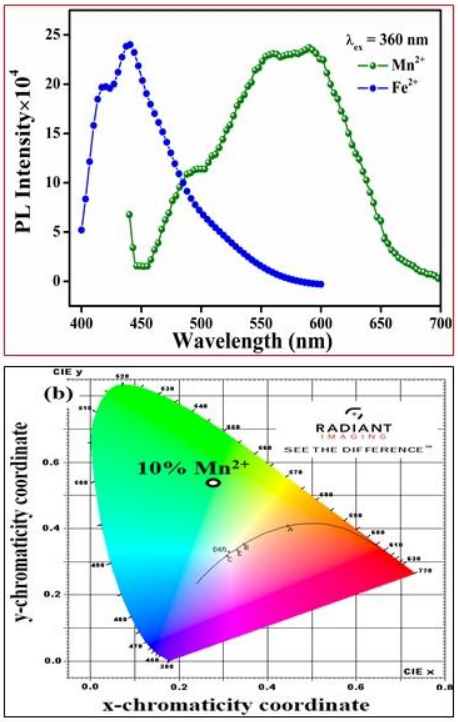

Figure 6. (a) PL spectra of π-$Y_{0.90}Mn_{0.10}BO_3$ and π-$Y_{0.90}Fe_{0.10}BO_3$ and **(b)** CIE coordinate of colour intensity of Mn^{2+} doped π-YBO_3.

The CIE 1931 XY coordinate plot for the Mn^{2+} doped sample as per their emission maxima has been presented in **Figure 6(b)**, which fell in the green region.

3. Magnetic properties

In **Figure 7(a)**, the Magnetic properties of π-$Y_{0.90}Mn_{0.10}BO_3$ have been investigated at 200 K. The sample exhibited a hysteresis loop with an immense coercivity value (H ≈ 31.5 K Oe), indicating ferromagnetic solid ordering[34]. The magnetic susceptibility of the sample was studied in zero field-cooled (ZFC) and field-cooled (FC) conditions. The ZFC measurements revealed antiferromagnetic ordering with a Neel temperature (T_N) of 108 K. Below T_N, the sample showed antiferromagnetic

behaviour, while above T_N, it showed paramagnetic behaviour. On the other hand, FC measurements showed ferromagnetic behaviour below Curie temperature (TC ≈ 171 K), indicating the existence of large domains in the same direction. These results provide important insights into the magnetic properties of π-$Y_{0.90}Mn_{0.10}BO_3$ at 200 K.

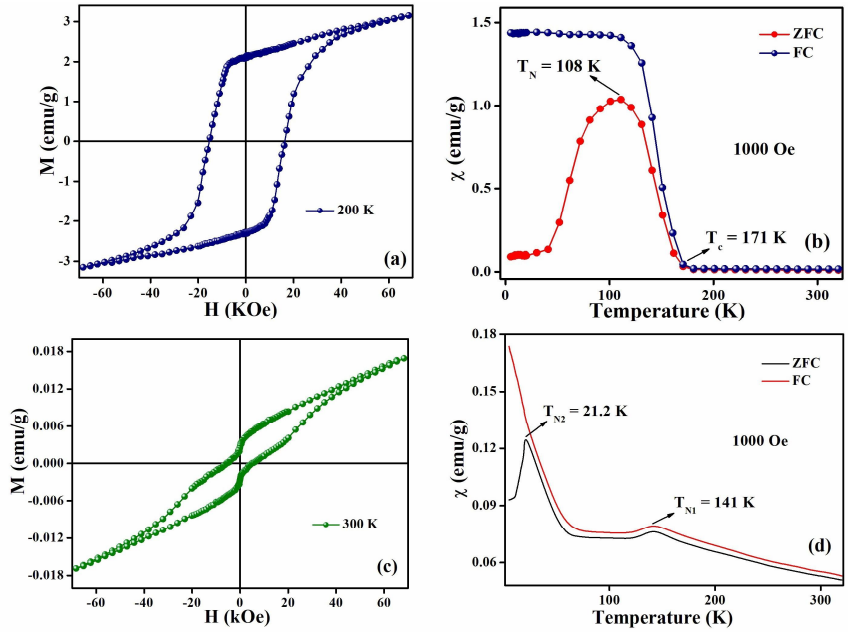

Figure 7. (a) and **(c)** show the magnetization versus magnetic field for π-$Y_{0.90}Mn_{0.10}BO_3$ and π-$Y_{0.90}Fe_{0.10}BO_3$. **(b)** and **(d)** represent the variation of magnetic susceptibility with temperature under zero field and at an applied field of 1000 Oe for π-$Y_{0.90}Mn_{0.10}BO_3$ and π-$Y_{0.90}Fe_{0.10}BO_3$.

The zero field-cooled (ZFC), and field cooled (FC) samples showed significant differences at low temperatures in the curve. This could be due to an inhomogeneous mixture of ferromagnetic and antiferromagnetic ordering in the sample and frustration in the lattice. Similar magnetic behaviour has been reported in the literature[35,36]. **Figure 7(c)** shows iron-doped samples' magnetization versus magnetic field. A small hysteresis loop suggests the presence of antiferromagnetic ordering in the sample at 300 K[37]. The magnetic susceptibility of π-$Y_{0.90}Fe_{0.10}BO_3$ under ZFC and FC conditions has been presented in **Figure 7(d)**. For Fe^{2+} doped π-YBO_3, the magnetic susceptibility was increased with a decrease in temperature from 320 K and exhibited a small cusp at around 141 K, indicating the presence of antiferromagnetic ordering. Below 133 K, magnetic susceptibility was again increased and exhibited a curve around 21.2 K before falling rapidly as the temperature approached 5 K. The cooled (FC) plot showed similar behaviour above 21.2 K temperature. The bifurcation in both ZFC and FC curves above 141 K might be due to the anisotropy in the system, which appeared well above T_N[38,39]. The ZFC/FC bifurcation also exhibited local spin or anti/ferromagnetic domain growth clustering. Such bifurcation behaviour was noticed for Fe_3BO_3 in the literature[40].

The magnetic moment value for the manganese doped sample was plotted with a temperature range of 5 K to 300 K (**Figure 8**). Magnetic moment increased with temperature up to 74 K and showed a decreasing trend. The magnetic moment (μ_{eff}) values were 5.74 BM at 74 K, corresponding to the +2-oxidation state of manganese. This was due to the orientation of domains at low temperatures, which became random at room temperature[41]. For the iron-doped sample, the magnetic moment increased with temperature. At room temperature, it was found to be 4.81 BM, corresponding to the only value of Fe^{2+} (d^6 configuration, 4 unpaired electrons).

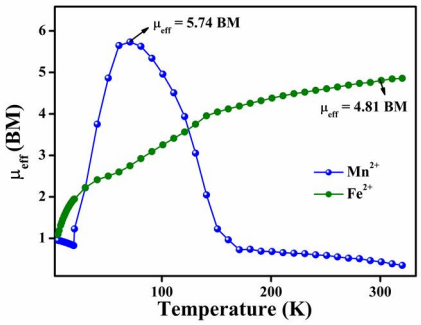

Figure 8. Magnetic moment versus temperature plot for manganese and iron, doped π-YBO_3.

3.1. Ferroelectric properties

The combine P-E loops of Mn^{2+} and Fe^{2+} doped sample at 7 V/cm potential have been shown in **Figure 9**. It was observed that π-YBO_3 doped with Mn^{2+} exhibited ferroelectric polarization, with $P_r \approx 9.52 \times 10^{-2}$ μC/cm^2 as the P-E loop's remnant polarisation value. The iron-doped sample also displayed ferroelectric polarization, with a remnant polarization value of 1.90×10^{-1} at zero electric fields[37,42].

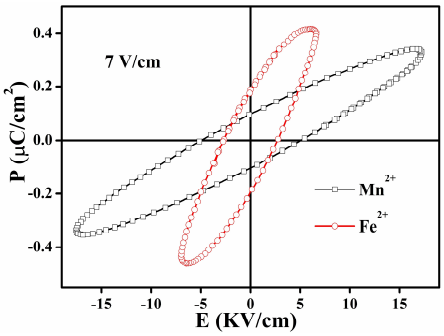

Figure 9. Ferroelectric hysteresis loop (P-E) curve for π-$Y_{0.90}Mn_{0.10}BO_3$ and π-$Y_{0.90}Fe_{0.10}BO_3$ at 7 V/cm.

3.2. Photocatalytic properties

The catalytic role of π-$Y_{0.90}Mn_{0.10}BO_3$ and π-$Y_{0.90}Fe_{0.10}BO_3$ for the photodegradation of RhB dye solution was studied. Temporal changes in absorbance maxima at λ = 549 nm (for RhB dye) in the presence of undoped and doped samples after shining with UV-visible radiation have been shown in **Figure 10(a–c)**.

The reduction in intensity of absorbance maxima confirmed their catalytic role in the presence of these samples. Approximately 57%, 93% and 87% of dye was observed to degrade in 90 min of exposure with undoped and doped samples, respectively (**Figure 10(d)**). The concentration of dye was computed using the expression,

$$C = C_0 \, exp \, (-kt)$$

C—concentration of dye at time *t*, C_0—concentration at $t = 0$ min, *k*—rate constant and *t*—time in minutes. Pseudo-first-order rate constants (*k*) for these experiments employing π-YBO_3, π-$Y_{0.90}Mn_{0.10}BO_3$ and π-$Y_{0.90}Fe_{0.10}BO_3$ as catalysts were 9.16×10^{-3}, 3.01×10^{-2} and 2.54×10^{-2} min^{-1}, whereas in the absence of catalyst (photolysis experiments), observed rate constant was found 5.14×10^{-4} min^{-1} (**Figure 10(e)**). The excitation of electrons from the valance band (VB) to the conduction band (CB) and generation of electron-hole ($e^- - h^+$) pairs is predicted due to the narrow bandgap[28].

$$\text{Catalyst} + h\nu \rightarrow e^- + h^+$$

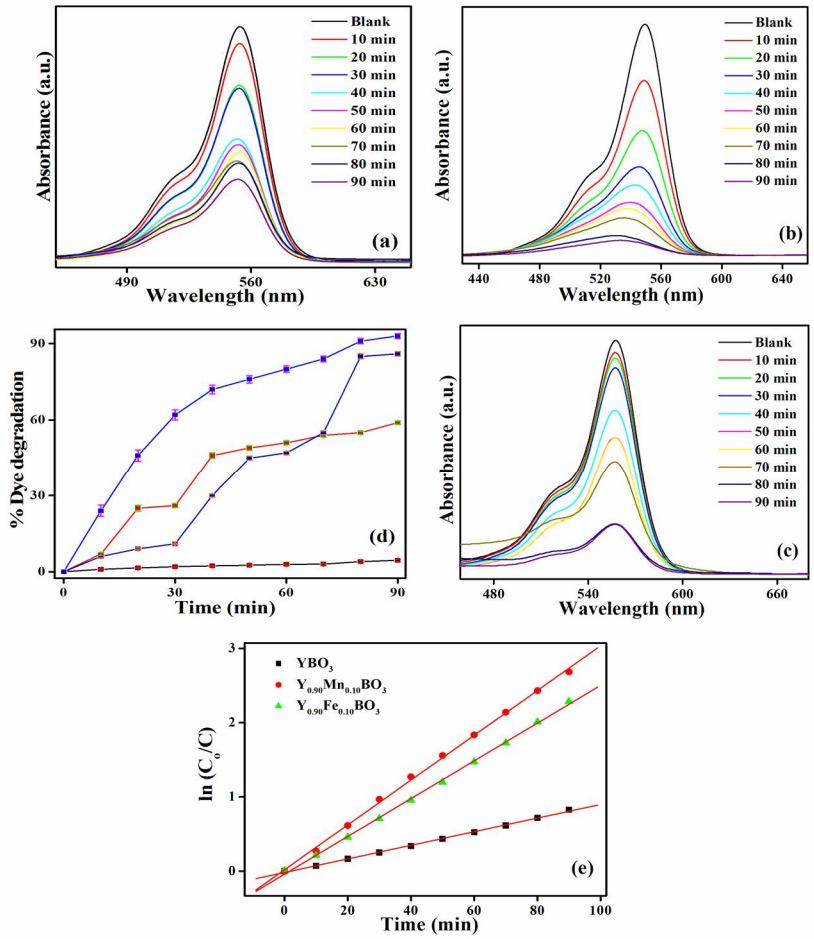

Figure 10. (a–c) Photocatalytic degradation of RhB under UV-visible irradiation, in presence of π-YBO_3, π-$Y_{0.90}Mn_{0.10}BO_3$ and π-$Y_{0.90}Fe_{0.10}BO_3$, **(d)** Dye degradation plot (Black = photolysis, Royal = π-YBO_3, Red = $Y_{0.90}Mn_{0.10}BO_3$ and Blue = π-$Y_{0.90}Fe_{0.10}BO_3$) and **(e)** ln (C_0/C) plot.

The holes (h^+) generated in the valance band will react with H_2O and hydroxyl anion (OH^-) acting as electron donors to form hydroxide radical ($OH^\bullet$). In the conduction band, electrons will react with electron acceptor species, i.e., oxygen molecule ($O_2^\bullet$) leading to the formation of reactive oxygen anion radical ($O_2^\bullet$).

Afterwards, reactive hydroperoxyl radical ($HO_2^\bullet$) will form. At the end, $OH^\bullet$, $O_2^{\bullet-}$, $HO_2^\bullet$ radicals will attack the dye molecule, leading to the intermediate with the formation of the final product. Photodegradation of dye through radical mechanism has already been reported in the literature[28,43].

$$RhB + (OH^\bullet), (O_2^{\bullet-}), (HO_2^\bullet) \rightarrow \text{intermediate} \rightarrow CO_2 + H_2O$$

The comparison study of magnetic and photocatalytic properties of our material with other literature is mentioned in the tabular form (**Table 1**).

To check the stability of our catalyst, we have performed a reusability experiment for the manganese and iron-doped samples (**Figure 11**). The results show that the catalyst degrades the same amount of dye solution until the 4th run. The high degradation of dye and stability is better performed by the manganese-doped sample over iron.

Table 1. Comparison of performance of manganese and iron doped orthoborate catalyst with the other photocatalyst.

Compound	Dye	Concentration (M)	Rate constant (min^{-1})	Efficiency (%)	Time (min)	Ref.
TiO_2 (P25)	RhB	2×10^{-5}	5.7×10^{-2}	85	20	[44]
$Co_{0.75}Fe_{2.25}O_4$	RhB	14×10^{-6}	2.41×10^{-1}	54.4	100	[45]
g-C_3N_4	RhB	5×10^{-2}	6.9×10^{-8}	95	320	[46]
Spray deposited ZnO	MB	5×10^{-2}	6.9×10^{-8}	95	60	[47]
ZnO-$ZnWO_4$	Crystal Violet	1×10^{-3}	2.96×10^{-8}	82	160	[48]
ZnO	RhB	4.17×10^{-5}	2×10^{-4}	8	120	[49]
6% Indium ZnO	RhB	4.17×10^{-5}	1.01×10^{-2}	76	120	[49]
γ-MnO_2	RhB	2×10^{-5}	-	90	270	[50]
$Y_{0.90}Mn_{0.10}BO_3$	RhB	1×10^{-5}	3.01×10^{-2}	93	90	Our work
$Y_{0.}90Fe_{0.10}BO_3$	RhB	1×10^{-5}	2.54×10^{-2}	87	90	Our work

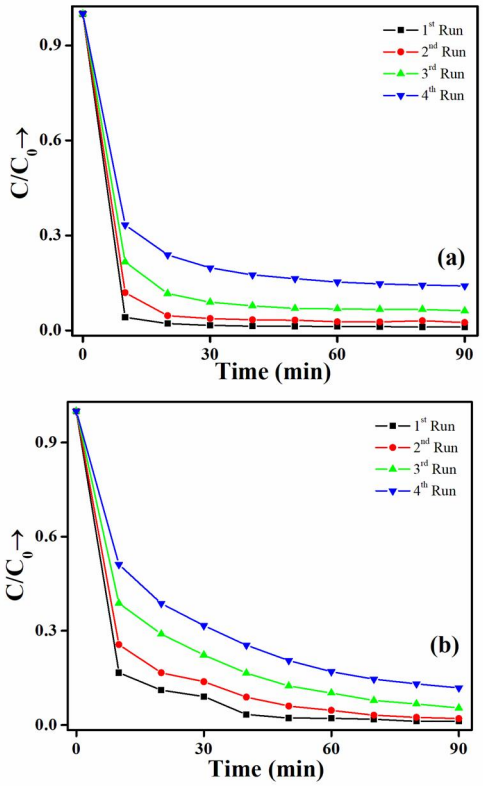

Figure 11. (a) Reusability experiment for manganese doped and **(b)** reusability experiment for iron doped sample.

4. Conclusions

The application of epoxide-mediated gel synthesis of crystalline π-YBO_3, transition metal doped π-YBO_3, has been demonstrated successfully. The PXRD patterns confirmed the inclusion of 10% manganese and iron in π-YBO_3. The optical and PL studies of doped samples have confirmed the presence of manganese and iron. Emission in the green region was observed in the CIE 1931 XY coordination plot for the manganese-containing sample. Magnetic susceptibility versus magnetic field data showed the ferromagnetic and antiferromagnetic behaviour for manganese and iron-doped samples. For doped samples, ferroelectric and at room temperature (300 K) were also observed. The photocatalytic properties of RhB under UV-visible irradiation in the presence of manganese and iron doped π-YBO_3, have been observed.

Author contributions

Conceptualization, PG and MS; methodology, PG; software, PG; validation, PG and MS; formal analysis, PG; investigation, PG; resources, PG; data curation, PG; writing—original draft preparation, PG; writing—review and editing, PG; visualization, PG; supervision, PG; project administration, PG; funding acquisition, MS. All authors have read and agreed to the published version of the manuscript.

Research data policy and data availability statement

The manuscript has associated data in a data repository.

Acknowledgments

The authors thank Sharda University for providing an Industrial Project Grant (SU/SF/2023/25).

Conflict of interest

The authors do the work, and have mutual consent to send it as a research paper for review. The authors do not have any conflict of interest.

References

1. Rowsell JLC, Gaubicher J, Nazar LF. A new class of materials for lithium-ion batteries: Iron (III) borates. *Journal of Power Sources* 2001; 97–98: 254–257. doi: 10.1016/S0378-7753(01)00532-8
2. Kurtzig AJ, Wolfe R, LeCraw RC, Nielsen JW. Magneto-optical properties of a green room-temperature ferromagnet: $FeBO_3$. *Applied Physics Letters* 1969; 14(11): 350–352. doi: 10.1063/1.1652682
3. Bither TA, Frederick CG, Gier TE, et al. Ferromagnetic VBO_3 and antiferromagnetic $CrBO_3$. *Solid State Communications* 1970; 8(2): 109–112. doi: 10.1016/0038-1098(70)90582-X
4. Takéuchi Y, Watanabe T, Ito T. The crystal structures of warwickite, ludwigite and pinakiolite. *Acta Crystallographica* 1950; 3: 98–107. doi: 10.1107/S0365110X50000252
5. Norrestam R, Kritikos M, Sjödin A. Manganese (II, III) oxyborate, Mn_2OBO_3: A distorted homometallic warwickite—Synthesis, crystal structure, band calculations, and magnetic susceptibility. *Journal of Solid State Chemistry* 1995; 114(2): 311–316. doi: 10.1006/jssc.1995.1049
6. Attfield JP, Clarke JF, Perkins DA. Magnetic and crystal structures of iron borates. *Physica B: Condensed Matter* 1992; 180–181: 581–584. doi: 10.1016/0921-4526(92)90401-D
7. Bertaut EF. Structures des boroferrites. *Acta Crystallographica* 1950; 3: 473–474. doi: 10.1107/S0365110X50001312
8. Li HK, Wang L, Cai GM, et al. Synthesis and crystal structure of a novel ludwigite borate: Mg_2InBO_5. *Journal of Alloys and Compounds* 2013; 575: 104–108. doi: 10.1016/j.jallcom.2013.04.024
9. Perkins DA, Attfield JP. Resonant powder X-ray determination of the cation distribution in $FeNi_2BO_5$. *Journal of the Chemical Society, Chemical Communications* 1991; 4: 229–231. doi: 10.1039/C39910000229
10. Fuchs B, Schröder F, Heymann G, et al. Crystal structure re-determination, spectroscopy, and photoluminescence of π-YBO_3: Eu^{3+}. *Journal of Inorganic and General Chemistry* 2021; 647(22): 2035–2046. doi: 10.1002/zaac.202100229
11. Pitscheider A, Kaindl R, Oeckler O, Huppertz H. The crystal structure of π-$ErBO_3$: New single-crystal data for an old problem. *Journal of Solid State Chemistry* 2011; 184(1): 149–153. doi: 10.1016/j.jssc.2010.11.018
12. Lin J, Sheptyakov D, Wang Y, Allenspach P. Structures and phase transition of vaterite-type rare earth orthoborates: A neutron diffraction study. *Chemistry of Materials* 2004; 16(12): 2418–2424. doi: 10.1021/cm0499388
13. Morgan PED, Carroll PJ, Lange FF. Crystal structure of $YSiO_2N$ and a reappraisal of the "vaterite" type, YBO_3. *Materials Research Bulletin* 1977; 12(3): 251–259. doi: 10.1016/0025-5408(77)90142-8
14. Levin EM, Roth RS, Martin JB. Polymorphism of ABO_3 type rare earth borates. *American Mineralogist: Journal of Earth and Planetary Materials* 1961; 46(9–10): 1030–1055.
15. Newnham RE, Redman MJ, Santoro RP. Crystal structure of yttrium and other rare-earth borates. *Journal of the American Ceramic Society* 1963; 46(6): 253–256. doi: 10.1111/j.1151-2916.1963.tb11721.x

16. Weir CE, Lippincott ER. Infrared studies of aragonite, calcite, and vaterite type structures in the borates, carbonates, and nitrates. *Journal of Research of the National Bureau of Standards. Section A, Physics and Chemistry* 1961; 65A(3): 173–180. doi: 10.6028/jres.065A.021
17. Weir CE, Schroeder RA. Infrared spectra of the crystalline inorganic borates. *Journal of Research of the National Bureau of Standards–A. Physics and Chemistry* 1964; 68A(5): 465–487. doi: 10.6028/jres.068A.045
18. Laperches JP, Tarte P. Infrared absorption spectra of rare earth borates (French). *Spectrochimica Acta* 1966; 22(7): 1201–1210. doi: 10.1016/0371-1951(66)80023-1
19. Kriz HM, Bray PJ. On the crystal structure of YBO_3, a vaterite-type borate. *The Journal of Chemical Physics* 1969; 51(8): 3624–3625. doi: 10.1063/1.1672566
20. Denning JH, Boss SD. The vibrational spectra and structures of some rare-earth borates. *Spectrochimica Acta Part A: Molecular Spectroscopy* 1972; 28(9): 1775–1785. doi: 10.1016/0584-8539(72)80148-X
21. Bradley WF, Graf DL, Roth RS. The vaterite-type ABO_3 rare-earth borates. *Acta Crystallographica* 1966; 20: 283–287. doi: 10.1107/S0365110X66000549
22. Chadeyron G, El-Ghozzi M, Mahiou R, Cousseins JC. Revised structure of the orthoborate YBO_3. *Journal of Solid State Chemistry* 1997; 128(2): 261–266. doi: 10.1006/jssc.1996.7207
23. Ren M, Lin JH, Dong Y, et al. Structure and phase transition of $GdBO_3$. *Chemistry of Materials* 1999; 11(6): 1576–1580. doi: 10.1021/cm990022o
24. Cohen-Adad MT, Aloui-Lebbou O, Goutaudier C, et al. Gadolinium and yttrium borates: Thermal behavior and structural considerations. *Journal of Solid State Chemistry* 2000; 154(1): 204–213. doi: 10.1006/jssc.2000.8837
25. Hosokawa S, Tanaka Y, Iwamoto S, Inoue M. Morphology and structure of rare earth borate ($REBO_3$) synthesized by glycothermal reaction. *Journal of Materials Science* 2008; 43: 2276–2285. doi: 10.1007/s10853-007-2023-x
26. Mahato SS, Mahata D, Panda S, Mahata S. Perspective chapter: Sol-gel science and technology in context of nanomaterials—Recent advances. *Sol-Gel Method-Recent Advances* 2023. doi: 10.5772/intechopen.111378
27. Gupta P, Sahni M, Chauhan S. Enhanced photoluminescence properties of rare earth elements doped $Y_{0.50}Gd_{0.50}BO_3$ phosphor and its application in red and green LEDs. *Optik* 2021; 240: 166810. doi: 10.1016/j.ijleo.2021.166810
28. Gupta P, Tomar R, Singh NB. Chromium-doped $Y_{0.50}Gd_{0.50}BO_3$ as an excellent photocatalytic and magnetic material. *Bulletin of Materials Science* 2021; 44: 251. doi: 10.1007/s12034-021-02541-z
29. Gu GX, Wang D, Lv XS, et al. In situ study on the structural transition in YBO_3 through Raman spectroscopy. *Materials Chemistry and Physics* 2011; 131(1–2): 274–277. doi: 10.1016/j.matchemphys.2011.09.041
30. Boonchom B, Baitahe R. Synthesis and characterization of nanocrystalline manganese pyrophosphate $Mn_2P_2O_7$. *Materials Letters* 2009; 63(26): 2218–2220. doi: 10.1016/j.matlet.2009.07.028
31. Orhan A, Aydin C, Aydin H, et al. Synthesis and optical properties of iron doped gallium nitride nanostructures by sol gel method. *Microsystem Technologies* 2015; 21: 1219–1224. doi: 10.1007/s00542-014-2273-x
32. Lever ABP. *Inorganic Electronic Spectroscopy*, 2nd ed. Elsevier; 1984.
33. You H, Zhang J, Hong G, Zhang H. Luminescent properties of Mn^{2+} in hexagonal aluminates under ultraviolet and vacuum ultraviolet excitation. *The Journal of Physical Chemistry C* 2007; 111(28): 10657–10661. doi: 10.1021/jp071889+
34. Li RK, Greaves C. $YCa_3(MnO)_3(BO_3)_4$: A manganese borate containing ferromagnetic chains on a kagomé lattice. *Physical Review B* 2003; 68(17): 172403. doi: 10.1103/PhysRevB.68.172403
35. Continentino MA, Pedreira AM, Guimaraes RB, et al. Specific heat and magnetization studies of Fe_2OBO_3, Mn_2OBO_3 and $MgScOBO_3$. *Physical Review B* 2001; 64: 014406. doi: 10.1103/PhysRevB.64.014406
36. Sultan K, Ikram M, Gautam S, et al. Electrical and magnetic properties of the pulsed laser deposited Ca doped $LaMnO_3$ thin films on Si (100) and their electronic structures. *RSC Advances* 2015; 5(85): 69075–69085. doi: 10.1039/C5RA08028B
37. Kumari K. Magnetic and dielectric properties of Fe_3BO_6 nanoplates prepared through self-combustion method. *Journal of Advanced Dielectrics* 2017; 7(6): 1750043. doi: 10.1142/S2010135X17500436
38. Matteppanavar S, Angadi B, Rayaprol S. Low temperature magnetic studies on $PbFe_{0.5}Nb_{0.5}O_3$ multiferroic. *Physica B: Condensed Matter* 2014; 448: 229–232. doi: 10.1016/j.physb.2014.04.024
39. Rivas-Murias B, Rivadulla F, Sánchez-Andújar M, et al. Role of t_{2g} versus e_g interactions in the physical properties of A_2OBO_3 (A = Mn, Fe). *Chemistry of Materials* 2006; 18(19): 4547–4552. doi: 10.1021/cm0609698
40. Maignan A, Lainé F, Guesdon A, et al. Charge ordering and multiferroicity in Fe_3BO_5 and Fe_2MnBO_5 oxyborates. *Journal of Solid State Chemistry* 2017; 246: 209–213. doi: 10.1016/j.jssc.2016.11.034
41. Karmakar R, Neogi SK, Midya N, et al. Magnetic properties of Mn doped ZnO: The role of synthesis route. *Journal of Materials Science: Materials in Electronics* 2016; 27: 6371–6381. doi: 10.1007/s10854-016-4572-8

42. Ke S, Lin P, Zeng X, et al. Tuning of dielectric and ferroelectric properties in single phase $BiFeO_3$ ceramics with controlled Fe^{2+}/Fe^{3+} ratio. *Ceramics International* 2014; 40(4): 5263–5268. doi: 10.1016/j.ceramint.2013.10.098
43. Tomar R, Abdala AA, Chaudhary RG, et al. Photocatalytic degradation of dyes by nanomaterials. *Materials Today: Proceedings* 2020; 29: 967–973. doi: 10.1016/j.matpr.2020.04.144
44. Zhong HE, Shaogui Y, Yongming JU, et al. Microwave photocatalytic degradation of rhodamine B using TiO_2 supported on activated carbon: Mechanism implication. *Journal of Environmental Sciences* 2009; 21(2): 268–272. doi: 10.1016/S1001-0742(08)62262-7
45. Su S, Guo W, Leng Y, et al. Heterogeneous activation of Oxone by $CoxFe_{3-x}O_4$ nanocatalysts for degradation of rhodamine B. *Journal of Hazardous Materials* 2013; 244–245: 736–742. doi: 10.1016/j.jhazmat.2012.11.005
46. Yadav AA, Kang SW, Hunge YM. Photocatalytic degradation of rhodamine B using graphitic carbon nitride photocatalyst. *Journal of Materials Science: Materials in Electronics* 2021; 32: 15577–15585. doi: 10.1007/s10854-021-06106-y
47. Hunge YM. Photoelectrocatalytic degradation of methylene blue using spray deposited ZnO thin films under UV illumination. *MOJ Polymer Science* 2017; 1(4): 135–139. doi: 10.15406/mojps.2017.01.00020
48. Kale V, Hunge YM, Kamble SA, et al. Modification of energy level diagram of nano-crystalline ZnO by its composites with $ZnWO_4$ suitable for sunlight assisted photo catalytic activity. *Materials Today Communications* 2021; 26: 102101. doi: 10.1016/j.mtcomm.2021.102101
49. Pradeev Raj K, Sadaiyandi K, Kennedy A, Sagadevan S. Photocatalytic and antibacterial studies of indium-doped ZnO nanoparticles synthesized by co-precipitation technique. *Journal of Materials Science: Materials in Electronics* 2017; 28: 19025–19037. doi: 10.1007/s10854-017-7857-7
50. Moulai F, Fellahi O, Messaoudi B, et al. Electrodeposition of nanostructured γ-MnO_2 film for photodegradation of rhodamine B. *Ionics* 2018; 24: 2099–2109. doi: 10.1007/s11581-018-2440-7

Materials Technology Reports 2023; 1(1): 288.
Original Research Article

Effect of the welding procedure on the deformation of superposed welds of a low carbon steel

Rafael Humberto Mota de Siqueira[1], Sheila Medeiros de Carvalho[2], Milton Sergio Fernandes de Lima[1,3,*]

[1] *Photonics Division, Institute for Advanced Studies, 12228-001 São José dos Campos, SP, Brazil*

[2] *Department of Mechanical Engineering, Federal University of Espirito Santo, 29075-910 Vitoria, ES, Brazil*

[3] *Thematic Network in Materials Engineering, Federal University of Ouro Preto, 35400-000 Ouro Preto, MG, Brazil*

*** Corresponding author:** Milton Sergio Fernandes de Lima, msflima@gmail.com

ARTICLE INFO

Received: 1 November 2023
Accepted: 23 November 2023
Available online: 19 December 2023

doi: 10.59400/mtr.v1i1.288

ABSTRACT: This study compared gas-metal arc welding (GMAW) and laser beam welding (LBW) for the superposed joining of two low-carbon steels. The motivation was to reduce the visible defects (notches) in the external part of one of the sheets. Both welding processes produced sound welds characterized by ferrite and pearlite; however, the notch disappeared when LBW was used. The hardness values of the fusion and heat-affected zones were similar for both processes, but the tensile strengths were very different. The shear tensile strengths of the LBW and GMAW were 415 and 84 MPa, respectively. Finite element analysis simulations indicated a more diffuse distribution of the von Mises stress throughout the welded component. The GMAW FEA model also presented a defect because of excessive heat transfer and residual stresses. In conclusion, LBW can replace GMAW in this particular case with improvements in appearance, productivity, and mechanical strength.

KEYWORDS: gas-metal arc welding; laser beam welding; low-carbon steel; automotive

1. Introduction

Several joining techniques have been exploited in the transportation industry and have attained a high level of automation and quality control. For automotive construction, arc, electrical resistance, friction, and laser methods have been widely employed for tailored-blank and body-in-white welds[1]. None of these methods except for minor defects should be considered for the purpose of the component. For example, a small undercut in a mid-floor auto blank can be considered less critical than an inconsistent weld in a door beam. In other cases, the part should attain a cosmetic appearance along with mechanical and metallurgical qualities. For example, this is the case for a truck bumper, which is usually a gas-metal arc weld (GMAW) to a clip in the body frame; however, the external appearance of the bumper should be as flat as possible for aesthetic reasons. These components are sometimes painted black at the end of the manufacturing line, and the appearance of small surface deformations is apparent to the client. In addition to the aesthetic question, GMAW seems to be sufficient to fulfill the requirements of the component during the truck lifetime[2].

In the present work, laser beam welding (LBW) is proposed as a replacement for GMAW for steel bumper clip joining. This replacement aims to overcome the small delamination at the free surface resulting from arc welding, together with enhanced automation potential and process speed. Mechanical tests were performed to evaluate the performance of each method.

A comparison between arc and laser methods has been reported in the literature. Sakai et al.[3] compared GTAW (gas-tungsten arc welding), plasma, and laser sources for the welding of SAE 300 M steel. For the authors, the choice of source did not change the tensile mechanical behavior or hardness.

Antunes and de Lima[4] compared GMAW, laser, and hybrid welding (laser plus GMAW) for the welding of 2.16 mm thick Dual Phase (DP) 600 steel. These authors reported that GMAW is not a suitable route because of the massive tempering of the base material, which results in premature failure. Similarly, both laser and hybrid techniques are recommended according to the microstructure, hardness, and tensile behavior standards.

Hashemzadeh et al.[5] studied the question of finite element models for GMAW and LBW steel sheets. Although the simulations seem to be a good fit to the experimental data, the question of deformation is missing, and according to the authors, a more robust model must be considered.

The novelty aspect of the present contribution concerns the comparison of steel superposed weld coupons from numerical computation results, which provides further robustness to the decision of automakers to consider one method or another.

The residual stresses in laser beam-welded C-Mn steel blanks were considered by Derakhshan et al.[6]. According to these authors, the residual stresses and deformations are linked to the heat input when comparing arc welding to laser welding. Similar results were reported by Pavan for austenitic stainless steels[7].

The objective of the present work is to verify whether laser beam welding (LBW) can replace gas-metal arc welding (GMAW) for superposed welding of 1.9 mm low-carbon steel sheets in terms of final deformations, microstructure, and mechanical behavior.

2. Experimental

A 1.9 mm thick low-carbon steel sheet with a composition of Fe-0.02_{max}C-0.25_{max}Mn-0.01_{max}Al-0.02_{max}P-0.30_{max}Ti (weight %), was used in the as-annealed state. According to the manufacturer, steel has a yield strength (YS) between 140 and 180 MPa, an ultimate tensile strength (UTS) between 270 and 330 MPa, a maximum elongation (ME) of 40%, and a hardness of approximately 48 HRB.

The welds were prepared according to the geometries required for application. GMAW realized a flat-position lap joint using an ESAB source and manual procedures. The arc welding parameters were 17.2 V, 76 A, wire speed of 6.3 mm/s, and argon gas shielding (8 L/min). The OK AristoRod 12.63 ESAB_filler wire (classification EN ISO 14341-A) had a diameter of 0.8 mm and a typical composition (Fe as the balance) of 0.074% C, 1.68% Mn, and 0.95% Si.

For LBW, a Yb:glass fiber laser (IPG Photonics, model YLR-2000) was used. The geometry was superposed sheets with the laser focus on the top of the upper sheet (0.1 mm spot diameter). After some free trials, the laser power was fixed at 1800 W, and the weld speed was 25 mm/s.

The welds were analyzed using an optical microscope (Zeiss, model Axio Imager.A2m) after polishing and etching with a solution of 2% nitric acid in ethanol. The hardness of the different regions was acquired using a FutureTech model FM-700 microhardness tester with a 100-gf load and a dwell time of 10 s. Tensile strength tests were carried out in an Instron universal mechanical testing machine (DL 10'000), with an axial speed of 1 mm/min. Three tensile coupons were tested for comparison purposes.

Finite element analysis (FEA) simulations were performed using Sysweld Software©[8]. Sysweld is

FEA software specially designed for welding and heat treatment of metals and alloys. For the current purpose, a mesh refined around the laser or arc path was designed, and the actual experimental conditions were considered. The material properties in the database were low-carbon steel grade DC04 (1.0338) for both the base sheets and wire.

3. Results and discussion

Figure 1 shows two micrographs of the transverse cut after GMAW and LBW. The GMAW joint, shown in **Figure 1(a)**, has a 5.2 mm wide weld bead with a resolidified material height of 2.8 mm and melts through the lower sheet of approximately 0.4 mm. A pore is perceived at the interface between the sheets, which is due to the pumping of gases into the gap. Large grains around the welded zone are shown in **Figure 1(a)**, owing to the heat input. **Figure 1(a)** also shows an arrow indicating a notch on the external surface of the bottom sheet. The notch dimensions are 0.27 mm wide and 0.03 mm deep, which is relatively small but easily noticed by a visual inspection of the component. **Figure 1(b)** shows an LBW cross-sectional micrograph with a typical heyhole shape. The laser-weld bead dimensions are 1.78 mm wide and 2.93 mm deep, with a maximum width of 0.6 mm in the heat-affected zone. Some small pores appear in the laser weld bead, but adjacent to the joint, as in the GMAW case. The free surface of the bottom sheet does not exhibit a notch, as shown in **Figure 1(a)**.

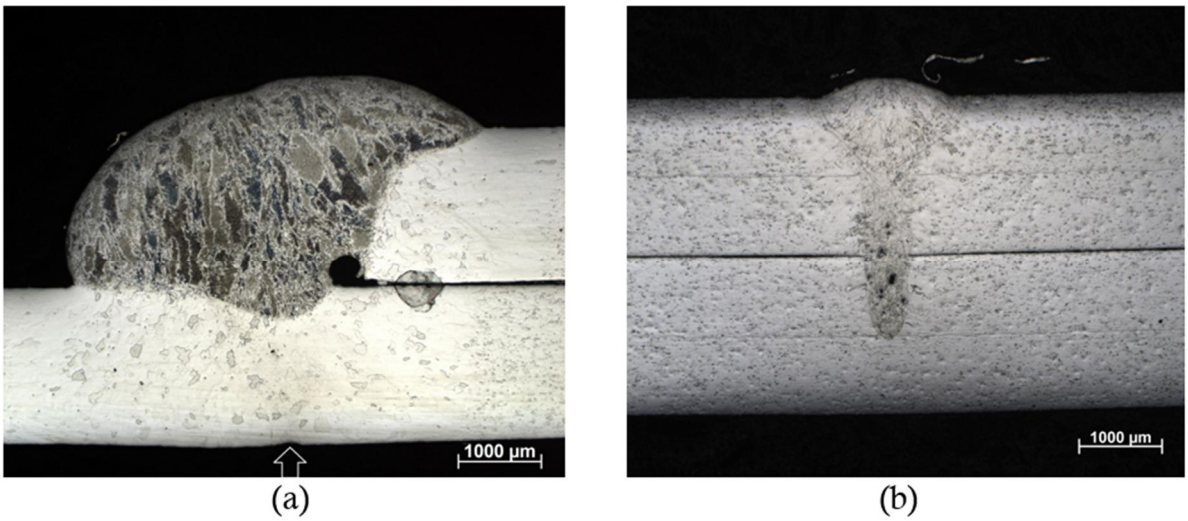

Figure 1. Optical micrographs of **(a)** GMAW and **(b)** LBW welds. The arrow indicates the notch at the bottom surface of the component.

Figure 2 shows two typical microstructures observed in the fusion zone (FZ) of the weld beads. The GMA weld beads (**Figure 2(a)**) were marked by the wire composition because the dilution of the base material was relatively low (**Figure 1(a)**). GMAW is characterized by grain boundaries, acicular ferrites, and pearlite in the middle of the grains (**Figure 2(a)**), in accordance with Boumerzoug et al.[9] and Bodude and Momohjimoh[10]. The laser beam-welded FZ (**Figure 2(b)**) presented ferritic (light gray) and pearlite (dark gray) grains, which also corroborates the literature[11,12].

Table 1 presents the average Vickers hardness (HV) values for the base material (BM), heat-affected zone (HAZ), and fusion zone (FZ) for different types of weld beads. The hardness of the base metal increased in the HAZ and FZ of the GMAW as a result of grain refinement. In the LBW case, the HV slightly increased in the FZ and HAZ because of the grain size.

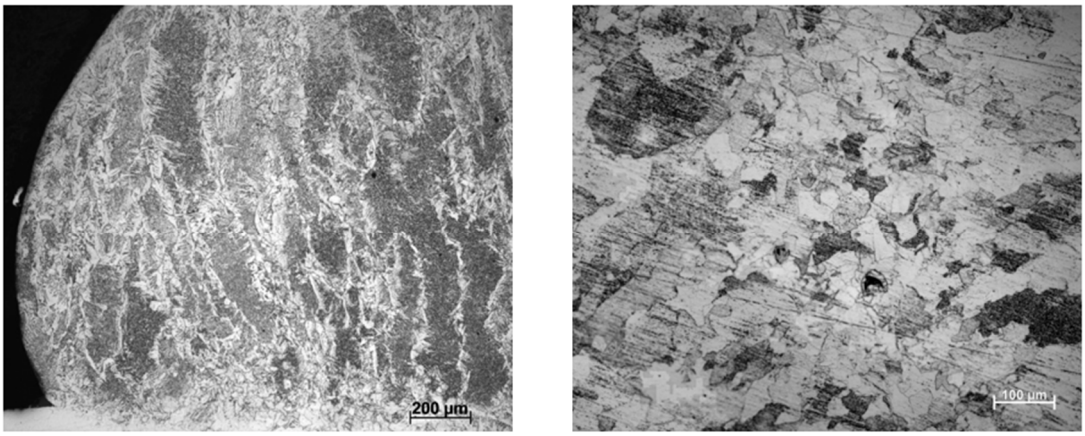

Figure 2. Optical microscopy images of the center of the fusion zone for **(a)** GMAW and **(b)** LBW.

Table 1. Hardness values for each region of the welds.

Region	GMAW	LBW
BM	100 ± 10	100 ± 10
HAZ	140 ± 10	110 ± 20
FZ	140 ± 10	150 ± 10

The stress-strain curves for a representative lap joint-type tensile test are presented in **Figure 3**. The shape and maximum strain points did not change significantly between the three tests under the same conditions. The maximum strengths of the LBW and GMAW coupons were 415 MPa and 84 MPa, respectively. In contrast, the maximum strains obtained for LBW and GMAW were 2.6% and 7.9%, respectively. In terms of toughness moduli, given by the area under the curves, LBW and GMAW are 2.9 MPa and 0.9 MPa, respectively.

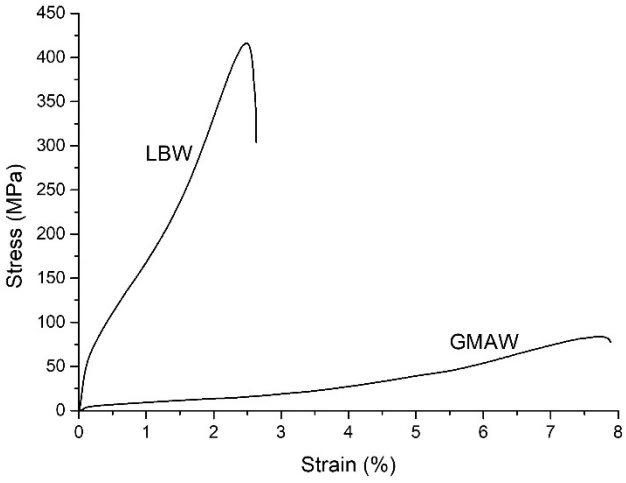

Figure 3. Lap-joint shear stress-strain curves representative of the LBW and GMAW samples.

The temperature profile in the middle of the welding process is shown in **Figure 4**. As can be seen, the GMAW case distributes the arc energy through a large portion of the component. For example, the temperature at the bottom of the lower sheet was 1200 °C in the GMAW case compared to the ambient temperature of the LBW case. The simulated dimensions of the melt pool (red areas in **Figure 4**) resemble the actual welds in both cases (**Figure 1**). Heat-affected zones (HAZ) are less visible because of the

ferritic base material. However, the presence of grain growth around the fusion region, as shown in **Figure 1(a)**, is indicative of the HAZ. Comparing **Figure 1(a)** and **Figure 4(a)**, it can be considered that the HAZ extends to approximately 1200 °C. This temperature was reported by Thaulow et al.[13] around the grain growth HAZ in low-carbon steels. The HAZ in the LBW case was much narrower than that in the GMAW case, approximately 300 μm in the optical micrograph (**Figure 1(b)**), giving approximately 700 °C in the simulated cross section (**Figure 4(b)**). This temperature was reported to be approximately equal to the A1 temperature of low-carbon steel[14]. In the literature by Oh et al.[15], these temperatures were sufficient to produce a hard and brittle HAZ composed of martensite. However, the very low carbon content kept the hardness level (**Table 1**) compatible with ferritic grains in the HAZ.

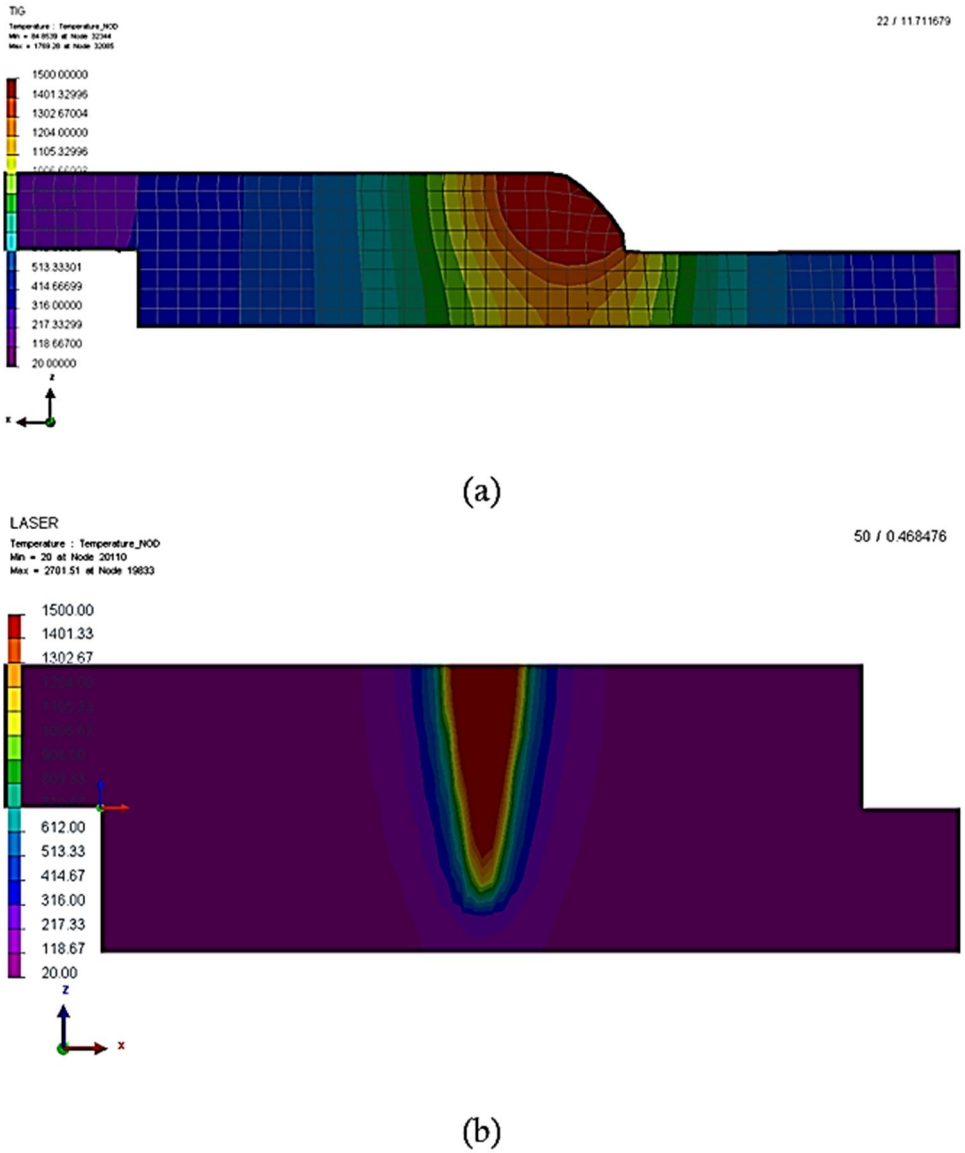

Figure 4. Temperature profiles for GMAW and Laser welds in the middle of the component.

From a thermomechanical point of view, **Figure 5** presents the Von Mises residual stresses for GMAW and LBW, as estimated from the upper free surface. The maximum residual stresses were approximately 220 MPa and 470 MPa for GMAW and LBW, respectively. Although the LBW stresses doubled the GMAW case, the laser beam weld confined the highest values, and the GMAW spread the stress lines far from the joint. As a result, the final displacement of the FEA mesh was much more

perceptible in the GMAW case than in the LBW case (**Figure 6**). In particular, a notch on the opposite face of the weld was visible in the GMAW simulation (**Figure 6(b)**). In the simulations, the volume was free to expand, and the notch was presented as a protuberance at the lower surface of the component (**Figure 6(b)**). This is exactly the inverse of the experimental evidence (arrow in **Figure 1(a)**) because, under real conditions, the sheets are not free to expand. Consequently, residual strain notches the surface at the bottom.

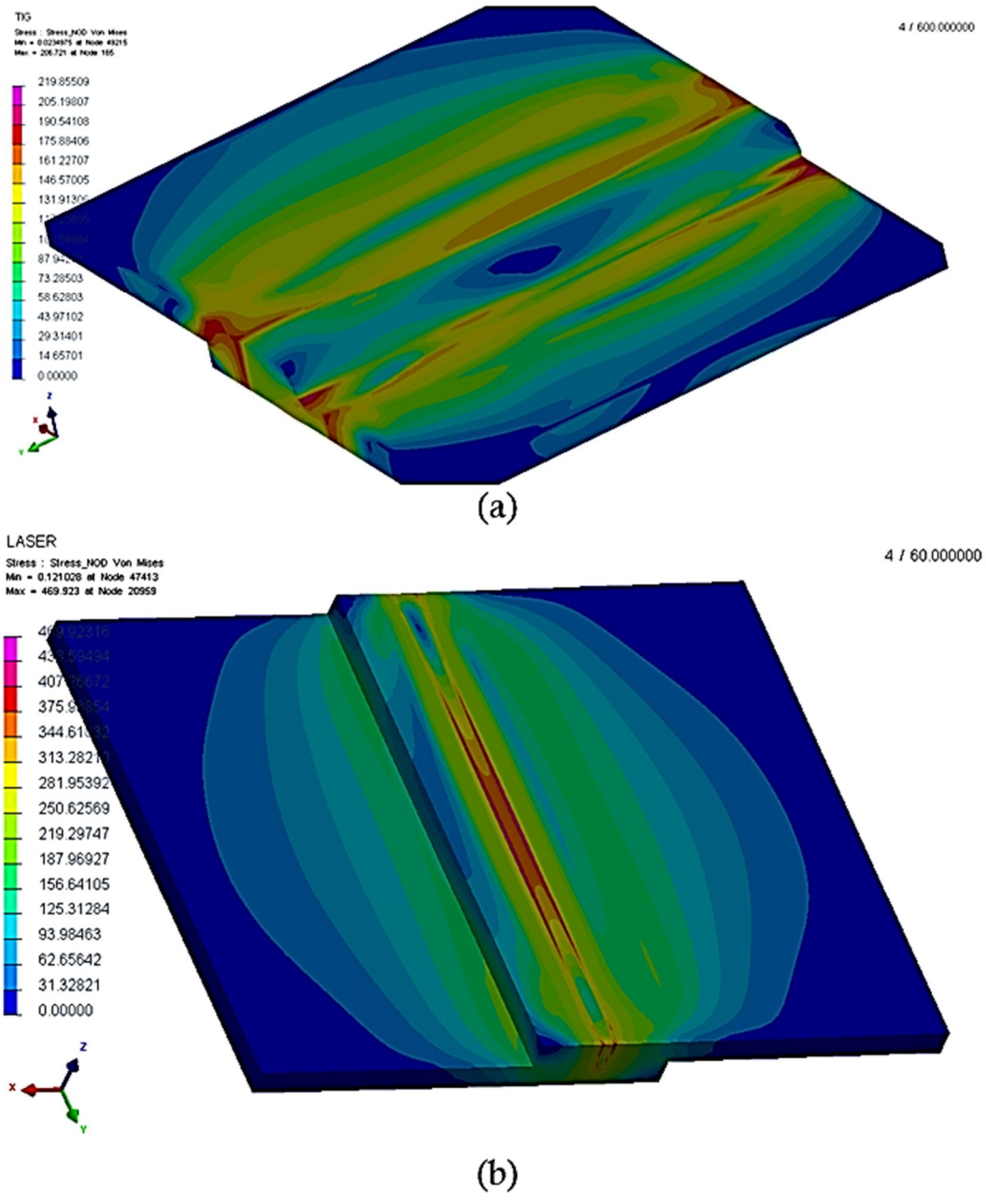

Figure 5. Von Mises stresses at the end of the simulation for **(a)** GMAW and **(b)** LBW.

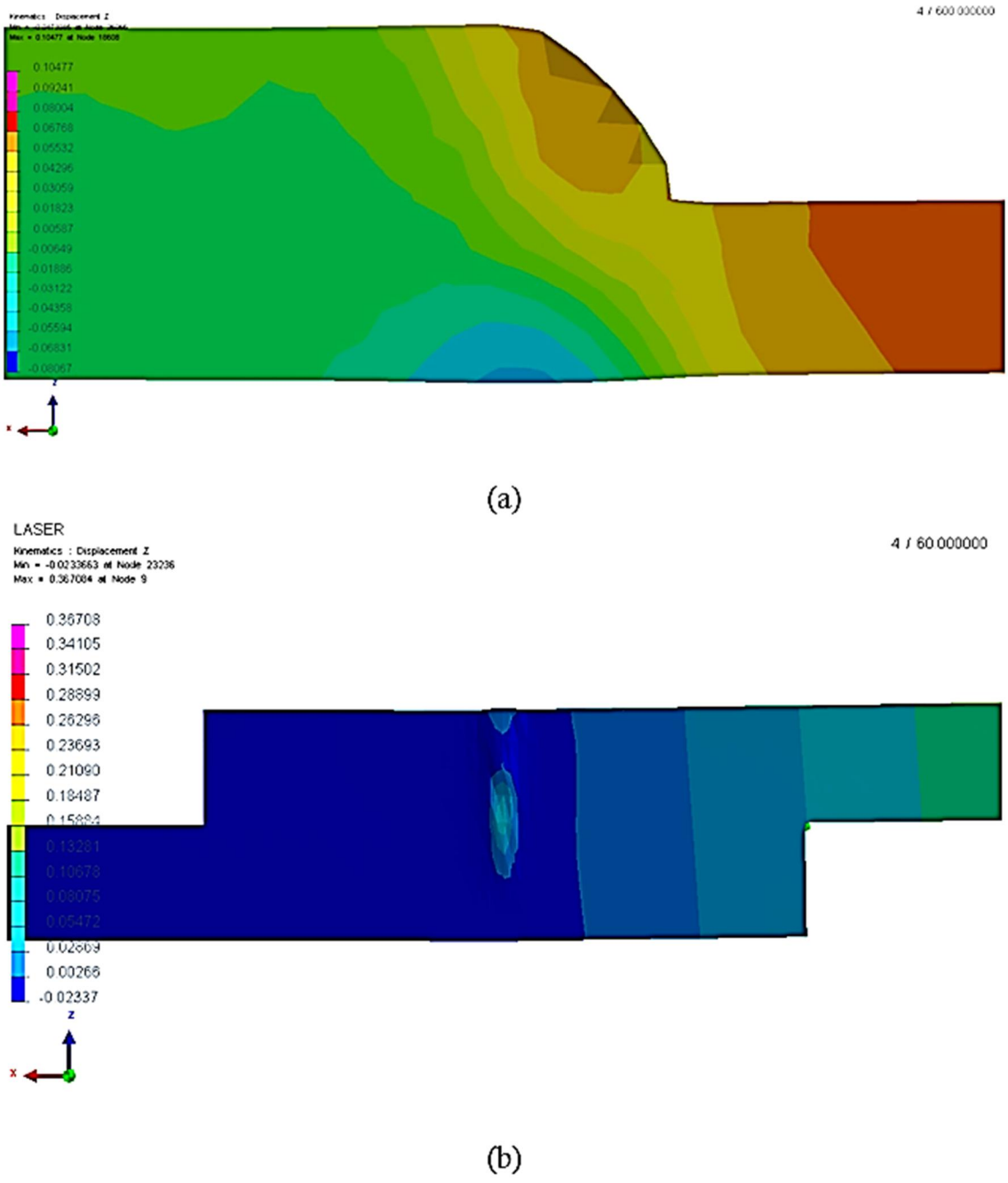

Figure 6. Final displacement of nodes in Z-direction (orthogonal to weld line) for **(a)** GMAW and **(b)** LBW.

4. Conclusions

The following conclusions were drawn:

Gas-metal arc welding (GMAW) and laser beam welding (LBW) were performed for superposed sheets of low-carbon steel.

The microstructures of the fusion zone are ferritic (LBW) or ferritic-pearlitic (GMAW), because the latter accounts for wire dilution.

The surface opposite the GMAW presented a notch as a visible defect, which was not present in the LBW.

The hardnesses of the base material, heat-affected zone, and fusion zone were similar (100–150 HV) owing to the majority of ferrite grains.

In terms of lap-shear tensile strength, LBW coupons were stronger (415 MPa) than GMAW coupons (84 MPa), but with a reduction in the final elongation from 7.9% to 2.6%.

Finite element analysis (FEA) indicated that the lateral heat exchange for GMAW was excessive, attaining 1200 °C at the face opposite to the weld. In the case of LBW, the opposite surface was maintained at room temperature.

The mechanical results of the FEA indicated a high von Mises maximum residual stress for LBW compared with GMAW. However, residual stresses were confined to the weldment. Owing to the intense heat input and residual stress, the GMAW presented a defect on the opposite surface.

Author contributions

Conceptualization, MSFdL; methodology, RHMdS; software, MSFdL; formal analysis, SMdC; investigation, MSFdL, SMdC and RHMdS; data curation, SMdC and RHMdS; writing—original draft preparation, MSFdL; writing—review and editing, SMdC; visualization, RHMdS; supervision, MSFdL; project administration, MSFdL; funding acquisition, MSFdL. All authors have read and agreed to the published version of the manuscript.

Acknowledgments

The authors acknowledge the São Paulo State Foundation (FAPESP) for financial support.

Conflict of interest

No conflict of interest was reported by all authors.

References

1. Hong KM, Shin YC. Prospects of laser welding technology in the automotive industry: A review. *Journal of Materials Processing Technology* 2017; 245: 46–69. doi: 10.1016/j.jmatprotec.2017.02.008
2. Baratzadeh F, Tay YY, Patil S, Lankarani HM. An experimental and numerical investigation into the dynamic crash testing of vehicle bumper fabricated using friction stir welding and gas metal arc welding. *International Journal of Crashworthiness* 2014; 19(4): 371–384. doi: 10.1080/13588265.2014.904062
3. Sakai PR, Lima MSF, Fanton L, et al. Comparison of mechanical and microstructural characteristics in maraging 300 steel welded by three different processes: LASER, PLASMA and TIG. *Procedia Engineering* 2015; 114: 291–297. doi: 10.1016/j.proeng.2015.08.071
4. Antunes WD, de Lima MSF. Experimental development of dual phase steel laser-arc hybrid welding and its comparison to laser and gas metal arc welding. *Soldagem & Inspeção* 2016; 21(3): 379–386. doi: 10.1590/0104-9224/SI2103.12
5. Hashemzadeh M, Chen BQ, Guedes Soares C. Comparison between different heat sources types in thin-plate welding simulation. In: Soares G, Peña L (editors). *Developments in Maritime Transportation and Exploitation of Sea Resources*. Taylor & Francis Group; 2014. pp. 329–335.
6. Derakhshan ED, Yazdian N, Craft B, et al. Numerical simulation and experimental validation of residual stress and welding distortion induced by laser-based welding processes of thin structural steel plates in butt joint configuration. *Optics & Laser Technology* 2018; 104: 170–182. doi: 10.1016/j.optlastec.2018.02.026
7. Pavan AR, Arivazhagan B, Vasudevan M, Sharma GK. Numerical simulation and validation of residual stresses and distortion in type 316L(N) stainless steel weld joints fabricated by advanced welding techniques. *CIRP Journal of Manufacturing Science and Technology* 2022; 39: 294–307. doi: 10.1016/j.cirpj.2022.08.010
8. ESI Group. Sysweld. Available online: https://www.esi-group.com/products/sysweld (accessed on 15 December 2023).
9. Boumerzoug Z, Derfouf C, Baudin T. Effect of welding on microstructure and mechanical properties of an industrial low carbon steel. *Engineering* 2010; 2(7): 502–506. doi: 10.4236/eng.2010.27066

10. Bodude MA, Momohjimoh I. Studies on effects of welding parameters on the mechanical properties of welded low-carbon steel. *Journal of Minerals and Materials Characterization and Engineering* 2015; 3(3): 55220. doi: 10.4236/jmmce.2015.33017
11. Yilbas BS, Arif AFM, Aleem BJA. Laser welding of low carbon steel and thermal stress analysis. *Optics & Laser Technology* 2010; 42(5): 760–768. doi: 10.1016/j.optlastec.2009.11.024
12. Deng D. FEM prediction of welding residual stress and distortion in carbon steel considering phase transformation effects. *Materials & Design* 2009; 30(2): 359–366. doi: 10.1016/j.matdes.2008.04.052
13. Thaulow C, Pauuw AJ, Guttormsen K. The heat affected zone toughness of low carbon microalloyed steels. *Metal Construct* 1985; 17(2): 94–99.
14. Zhang W, Roy GG, Elmer JW, DebRoy T. Modeling of heat transfer and fluid flow during gas tungsten arc spot welding of low carbon steel. *Journal of Applied Physics* 2003; 93(5): 3022–3033. doi: 10.1063/1.1540744
15. Oh HS, Kang J, Tasan CC. Enhancing damage-resistance in low carbon martensitic steels upon dual-pass laser treatment. *Scripta Materialia* 2021; 192: 13–18. doi: 10.1016/j.scriptamat.2020.09.047

Materials Technology Reports 2023; 1(1): 293.
Original Research Article

Examination of surface contamination and impurities in tinplate samples, both passivated and non-passivated

Amirhossein Meysami[1], Reza Amini Najafabadi[1,*], Ehsan Nemati Varnoosfaderani[2], Erfan Aghili[1], Aliasghar Foroughifar[3]

[1] *Materials Engineering Group, Golpayegan College of Engineering, Isfahan University of Technology, 87717-67498 Golpayegan, Iran*

[2] *Advanced Materials Research Center, Department of Materials Engineering, Najafabad Branch, Islamic Azad University, 85141-43131 Najafabad, Iran*

[3] *Department of Mechanical Engineering, Golpayegan College of Engineering, Isfahan University of Technology, 87717-67498 Golpayegan, Iran*

*** Corresponding author:** Reza Amini Najafabadi, r.amini@iut.ac.ir

ARTICLE INFO

Received: 3 November 2023
Accepted: 22 November 2023
Available online: 19 December 2023

doi: 10.59400/mtr.v1i1.293

ABSTRACT: This study examined the surfaces of non-passivated and passivated tinplate samples, as well as the impurities present on them, using SEM, EDS, and GDOES. Additionally, solutions were analyzed using ICP in order to identify any correlations between the elements present in the solutions and on the strip surfaces. The results from GDOES indicated the presence of unwanted elements, such as Sn, S, Cr, N, P, Zn, Fe, Mn, C, and Si, on both the passivated and non-passivated sample surfaces. SEM analysis of the passivated sample revealed light and dark regions in parallel lines, which were observed ahead of the rolling direction. EDS analysis indicated that the light areas were rich in Sn while the dark areas were rich in Fe, and C was identified as an unwanted element in both areas. O and Cr were only found in the dark areas. EDS analysis of the impurities revealed Na, S, Cl, Ca, Mg, Si, N, and Al as unwanted elements. The results suggest that unwanted elements are transferred from the steel strip surface to different solutions in the tinplate line, causing pollution in various solutions.

KEYWORDS: tinplate surface; surface impurities; unwanted elements; passive

1. Introduction

Food contact surfaces play a critical role in ensuring food safety and quality[1–3]. As such, it is essential to identify and minimize potential sources of contamination, including the presence of unwanted elements on the surface of the tinplate. In identifying sources of pollution, several criteria are utilized, encompassing factors like chemical composition, environmental impact, and concentration levels[4,5]. Elements or compounds known for their harmful effects on the environment or human health are typically labeled as pollutants. However, the exclusion of substances such as viruses, bacteria, and certain compounds often stems from their biological nature or the focus on chemical pollutants. While these biological agents can cause contamination and health issues, they might not align with conventional pollutant definitions. In the context of addressing contamination on the surface of tinplate, the emphasis could be on chemical elements or compounds that adhere to the surface,

potentially impacting its use or posing risks upon contact, thus prioritizing their identification and mitigation over biological contaminants. This focus allows for more effective control and management of contamination in industrial settings, aligning with the specific concerns related to surface pollutants in manufacturing or processing.

Previous studies have utilized various analytical techniques to investigate the surface layer of commercial tinplate[6–10]. For instance, in addition to the XPS method with argon ion sputtering used by Chen et al.[11], Sun et al.[12], and Azzerri et al.[13], other studies have employed techniques such as Raman spectroscopy[14], atomic force microscopy[15], and X-ray diffraction[16] to analyze the surface composition and structure of tinplate.

In this study, we employed SEM, GDOES, and EDS to investigate the presence of unwanted elements and components on both passivated and non-passivated samples of tinplate. These techniques allowed us to identify the different elements present on the surface and determine their distribution and concentration. We also utilized ICP to analyze the elements in the process solutions of the tinplate line, which helped us understand the sources of these unwanted elements and their correlation with the elements present on the polluted tinplate surface. The surface of tinplate is susceptible to contamination from a variety of sources. One major contributor is the use of raw materials that are not properly screened for impurities. Contaminants from the raw materials can find their way onto the surface of the tinplate during production, leading to an inferior product. Inadequate cleaning procedures can also be a source of unwanted elements on the surface of the tinplate. If the equipment used in the manufacturing process is not thoroughly cleaned between batches, residual contaminants can build up and transfer onto the surface of the tinplate. This can have a negative impact on the appearance and quality of the final product. Poor passivation techniques can also lead to the transfer of unwanted elements onto the surface of the tinplate. Passivation is a process used to create a protective layer on the surface of the tinplate, which helps prevent corrosion and other types of damage. If this process is not properly executed, contaminants can become trapped within the passivation layer and eventually make their way to the surface of the tinplate. To mitigate these issues, it is crucial to establish and maintain effective quality control measures throughout the production process. This includes rigorous screening of raw materials, implementing and enforcing thorough cleaning procedures, and ensuring proper execution of passivation techniques. By doing so, manufacturers can optimize their production process and deliver high-quality tinplate that is free from contamination. The novelty of this study lies in the comprehensive investigation of the presence of unwanted elements and components on both passivated and non-passivated tinplate samples using various analytical techniques such as SEM, GDOES, EDS, and ICP. While previous studies have used the XPS method with argon ion sputtering to analyze the surface layer of commercial tinplate, this study goes further by examining the potential correlation between unwanted elements in the solution used in the production and the elements present on the polluted tinplate surface. The findings of this study can contribute to the development of effective strategies to reduce the pollution of tinplate surfaces, improve production quality, and enhance customer satisfaction.

2. Experimental method

In this study, various methods were utilized to investigate the chemical composition and elements present on the surface of tinplate. Two types of samples were prepared, including non-passivated tinplate (free from any surface contamination) and passivated tinplate (with surface pollution), with dimensions of 50 mm × 50 mm × 0.25 mm and a coating mass of 2.8 g/m^2. Scanning electron

microscopy (SEM) with the ZEISS EVO MA18 model from Germany was used to examine the samples using secondary electrons, electron back-scattered electrons, luminescence cathodes, and back-scattered separation detectors. For quantitative analysis, energy-dispersive X-ray spectroscopy (EDS) was utilized with the same device. To detect elements in solution samples, inductively coupled plasma spectrometry (ICP) with Integra XL construction company GBC Australia was employed. To investigate the chemical composition of the very thin layer on the surface of tinplate samples, glow discharge optical emission spectroscopy (GDOES) with the GDA 750 HR SPECTRUMA ANALYTIK GMBH company was used, which is capable of identifying up to 79 elements with a resolution of one nanometer in the analysis and can cover a depth of 200 microns. One of the novelties of this study is the utilization of GDOES to study the chemical composition of the very thin layer on the surface of tinplate samples. Moreover, the combination of SEM, EDS, ICP, and GDOES analysis provided a comprehensive understanding of the elements present on the surface of tinplate and their behavior in different solutions, which can be helpful in improving the quality and safety of food packaging materials.

3. Results and discussion

The surface morphology and microstructure of both passivated and non-passivated samples were examined using SEM and EDS analysis. The SEM and EDS results of the non-passivated sample are illustrated in **Figure 1** and **Figure 2**. The surface exhibits burrs, notches, and impurities. EDS analysis revealed the presence of O, Sn, and Fe, with Fe accounting for around 13 atomic%. As a result of the presence of impurities on the surface, further investigation was necessary. SEM analysis showed that impurities A and B were present on the surface of the non-passivated sample, as shown in **Figure 3** and **Figure 4**.

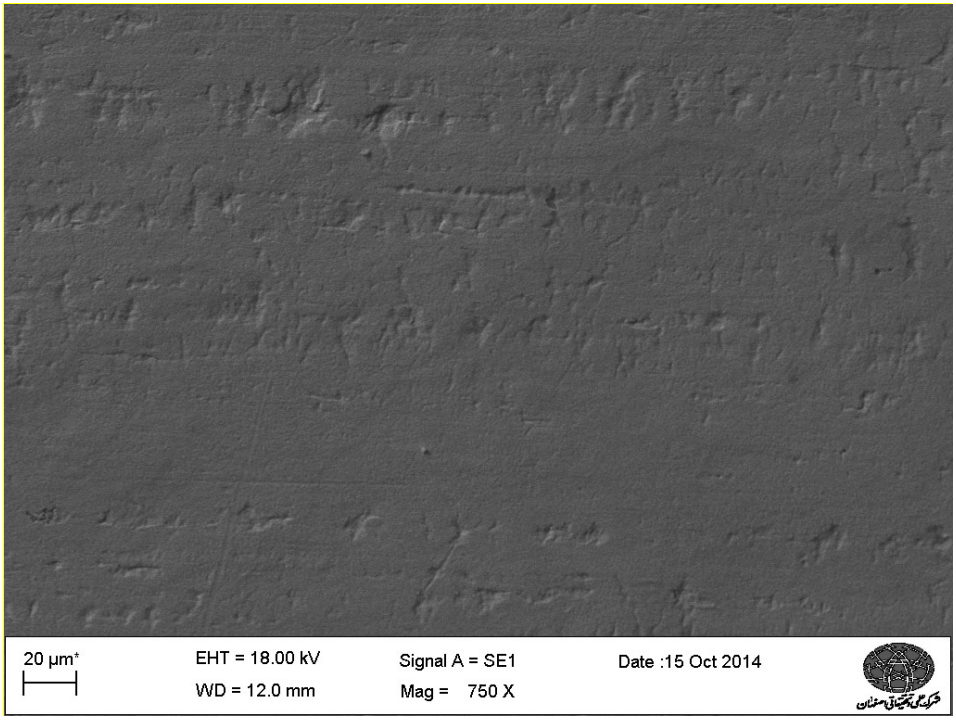

Figure 1. SEM of non-passivated sample.

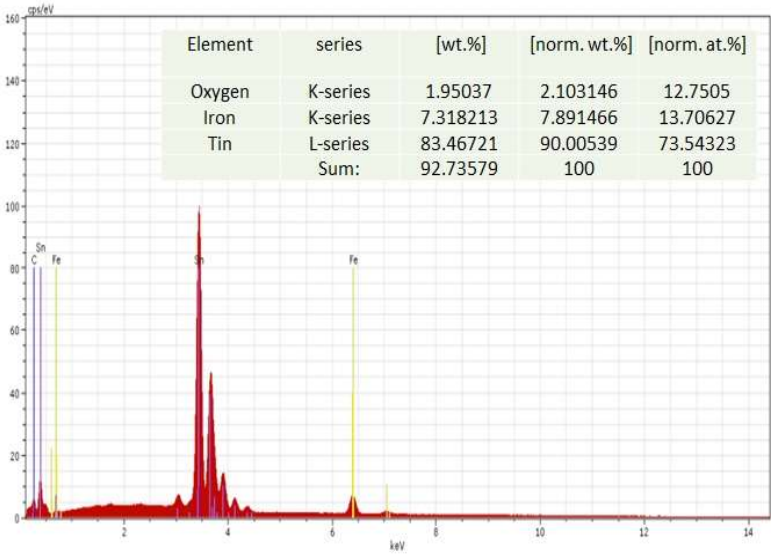

Figure 2. EDS result of non-passivated sample.

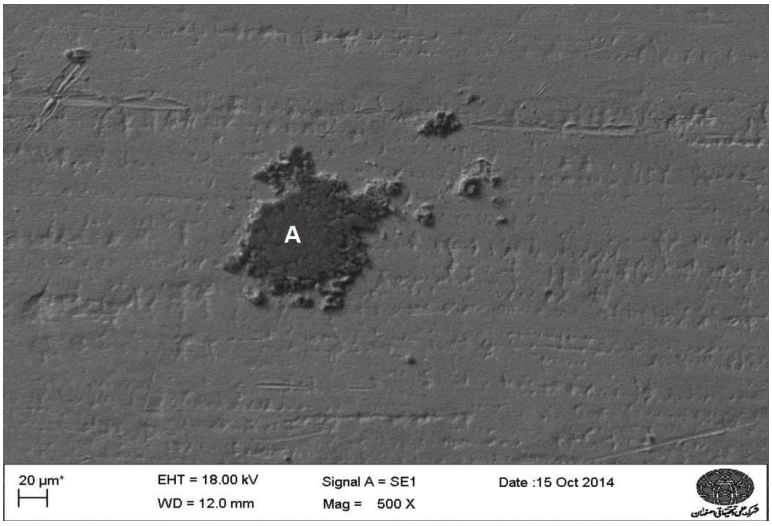

Figure 3. SEM of impurity (A) on the non-passivated sample.

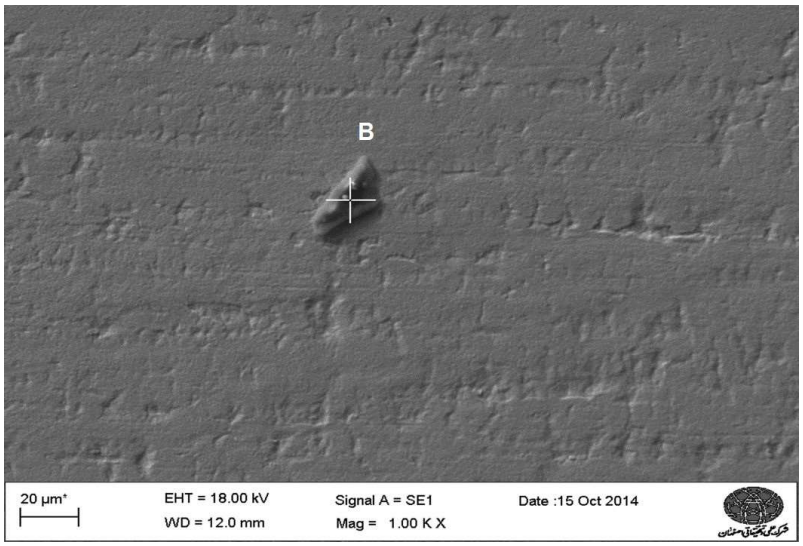

Figure 4. SEM of impurity (B) on the non-passivated sample.

The EDS analysis of these impurities (A and B) is presented in **Figure 5** and **Figure 6**. Unwanted elements, including Cl, O, Fe, S, C, Mg, Al, Si, Ca, and Na, were detected. The turbulence of the coating electrolyte may cause impurities to transfer to the strip surface. These impurities can then move to adjacent cells through the strip and contaminate their solutions as well.

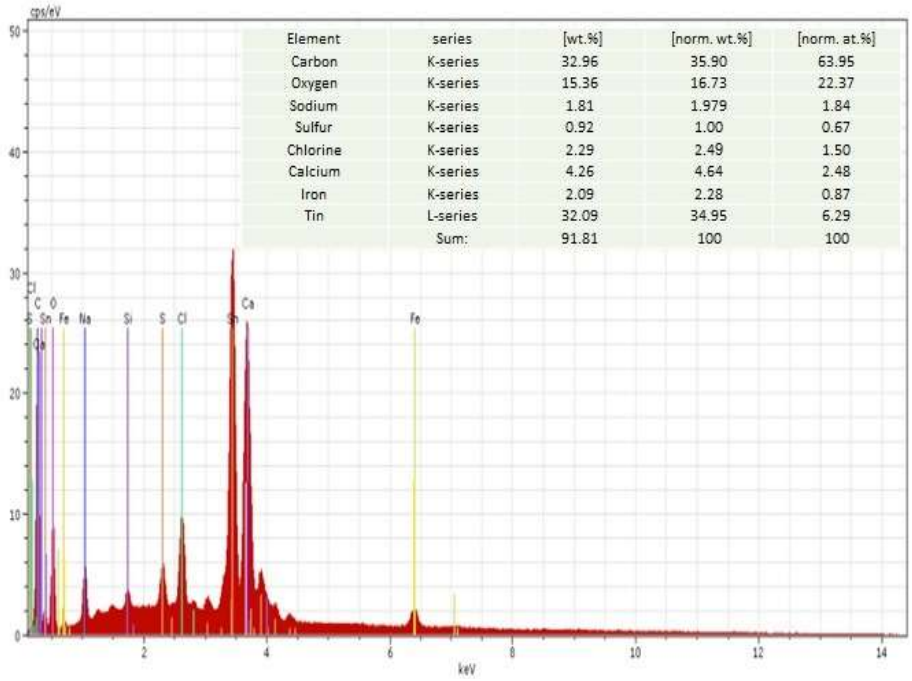

Element	series	[wt.%]	[norm. wt.%]	[norm. at.%]
Carbon	K-series	32.96	35.90	63.95
Oxygen	K-series	15.36	16.73	22.37
Sodium	K-series	1.81	1.979	1.84
Sulfur	K-series	0.92	1.00	0.67
Chlorine	K-series	2.29	2.49	1.50
Calcium	K-series	4.26	4.64	2.48
Iron	K-series	2.09	2.28	0.87
Tin	L-series	32.09	34.95	6.29
	Sum:	91.81	100	100

Figure 5. EDS result of impurity (A) on the non-passivated sample.

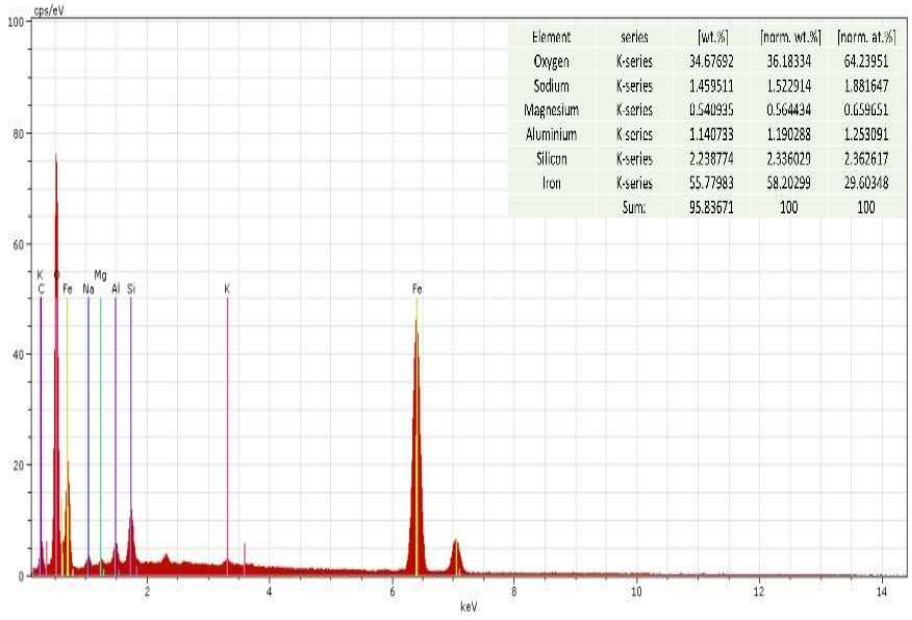

Element	series	[wt.%]	[norm. wt.%]	[norm. at.%]
Oxygen	K-series	34.67692	36.18334	64.23951
Sodium	K-series	1.459511	1.522914	1.881647
Magnesium	K-series	0.540935	0.564434	0.659651
Aluminium	K-series	1.140733	1.190288	1.253091
Silicon	K-series	2.238774	2.336029	2.362617
Iron	K-series	55.77983	58.20299	29.60348
	Sum:	95.83671	100	100

Figure 6. EDS result of impurity (B) on the non-passivated sample.

The SEM result of the passivated sample is displayed in **Figure 7**. Dark and light parallel areas, indicating the rolling direction, were observed in **Figure 8**. The EDS analysis of the light and dark areas is presented in **Figure 9** and **Figure 10**, which confirmed that the dark areas were enriched in Fe with a

high concentration of C as an unwanted element. Cr was also observed in the dark areas. The light areas were rich in Sn, with a high concentration of C as an unwanted element, similar to the dark areas.

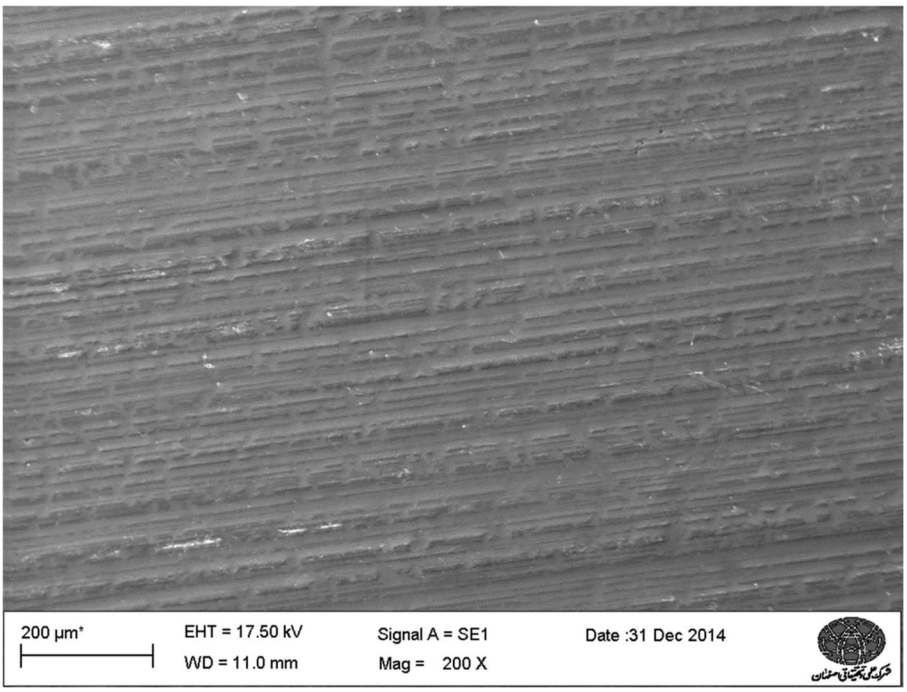

Figure 7. SEM of passivated sample.

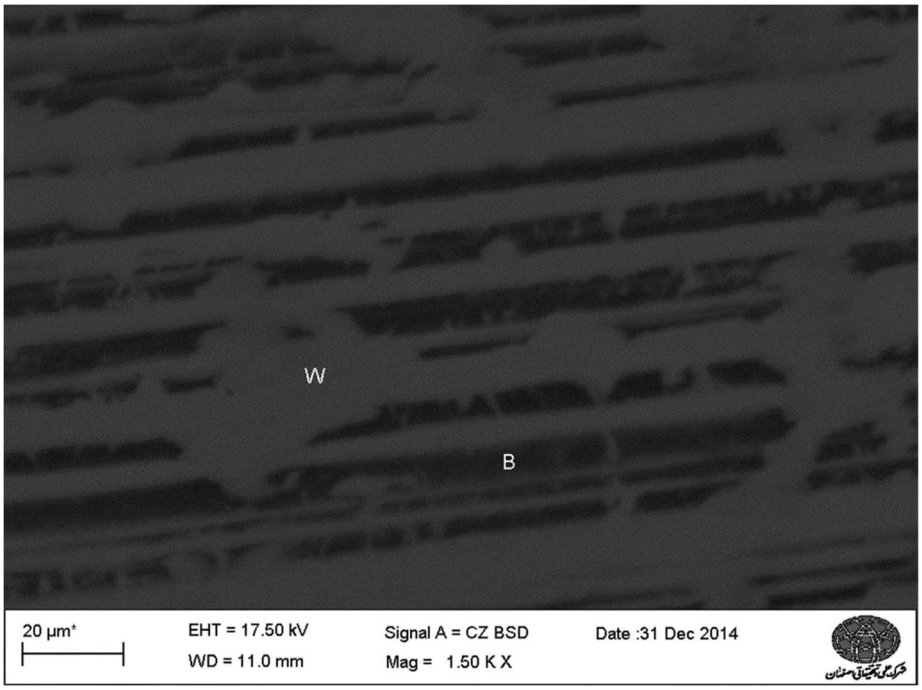

Figure 8. SEM of passivated sample on dark & light areas.

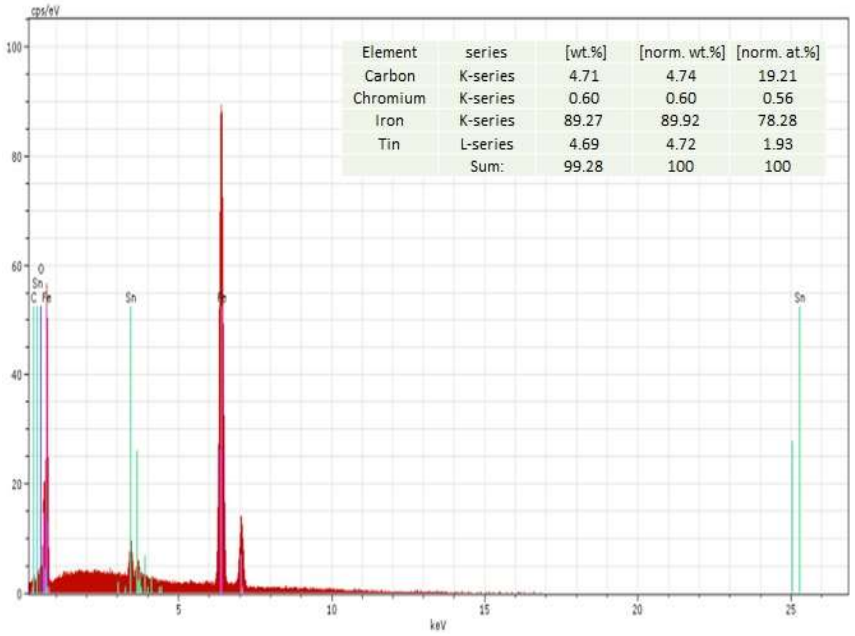

Figure 9. EDS of B point (dark area) on passivated sample.

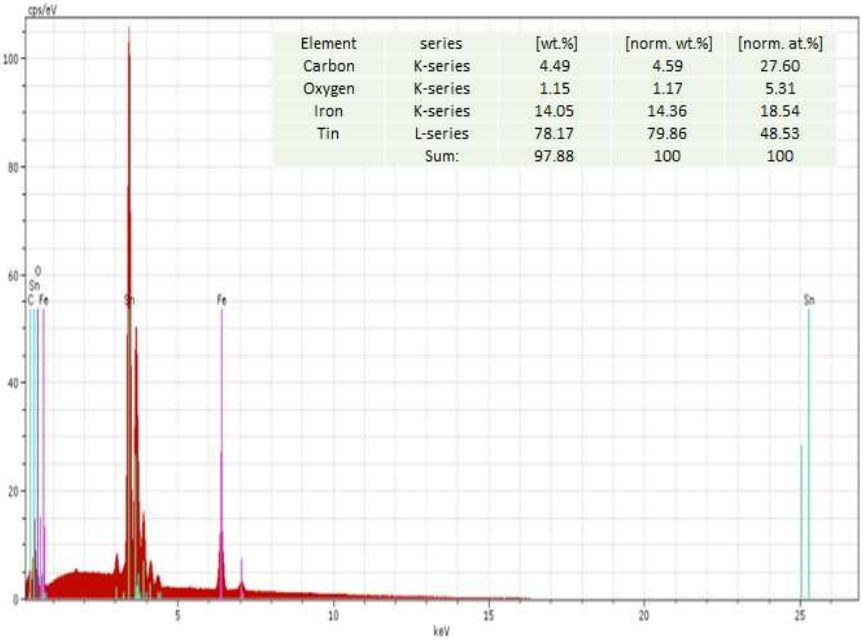

Figure 10. EDS of W point (light area) on passivated sample.

The oxygen content in the bright area depicted in **Figure 8** is relatively low. The relatively low oxygen content in the passive area of the tin plate can be attributed to the formation of a protective layer or film that impedes further oxidation. Tin plates often develop a passive layer. This layer acts as a barrier, reducing direct contact between the underlying metal and the surrounding environment. Consequently, the availability of oxygen for further oxidation reactions on the surface decreases, resulting in a relatively low oxygen content in the passive area of the tin plate. This protective layer helps maintain the metal's integrity while limiting the extent of oxygen interaction, thereby keeping the oxygen content comparatively low in the passive region.

There was no oxygen in the dark areas, but in the light areas, it was significantly present. Oxygen was observed due to the presence of the tin oxides SnO and SnO_2 on the surface. There was no Cr in the

light areas. ICP has been used for investigating tinplate lines with different cell solutions and GDOES for the surfaces of passivated and non-passivated samples.

The chemical composition of the plating electrolyte is shown in **Table 1**. The elements Sn, S, C, and Fe in small amounts due to the dissolution of the steel strip are expected. This result is shown in the significant unwanted elements Fe, Pb, Mn, Cr, Si, and Ca. The source of the very high amount of Fe, Mn, and Si in the electrolyte is due to the frequent stoppages of steel strips in acidic plating electrolytes during the long age of this solution. At the time of the test, the solution to this study was about 12 years old.

Table 1. ICP result of plating electrolyte.

Element	Quantity (ppm)
Fe	3100
Pb	33.2
Zn	2.15
Mn	56.4
Cr	8.4
Sn	25,600
Si	10
Ni	4.6
Ca	8
S	260

The presence of Pb, Ca, and Cr is also caused by impurities in the raw materials PSA and ENSA, as well as tin anodes consumed during the life of the electrolyte. The chemical composition of the passivation solution is shown in **Table 2**. As expected, the main ingredient in the chemical composition of the solution is Cr. But the presence of Sn, Si, S, and Fe in concentrations is remarkable. According to the above results, the transmission of different elements from plating cells to the next cells by the strip surface is observable. Also, the high age of the plating electrolyte causes contamination of the solution due to the raw materials PSA, ENSA, and Sn anodes and strip stoppages.

Table 2. ICP result of passivation solution.

Element	Quantity (ppm)
Fe	3.90
Pb	0.30
Zn	0.10
Mn	0.75
Cr	1950
Sn	5.00
Si	4.00
Ni	0.50
Ca	0.50
S	5.00

The GDOES test was used for quantitative analysis of elements present on the surface layer of the

sample. The results showed that for the non-passivated surface, S was detected in the first moment, and then Sn was exposed to large amounts as specified in **Figure 11**. N, P, Zn, C, and Fe were also present. In this experiment, Si and Mn were not observed. After the preliminary detection of C, it was reduced to zero by test time. In terms of priority element detection by the device, S, N, Sn, P, Zn, C, and Fe were detected on the surface in the first moments of the test. As mentioned above, a large amount of S, N, and Sn was available on the surface.

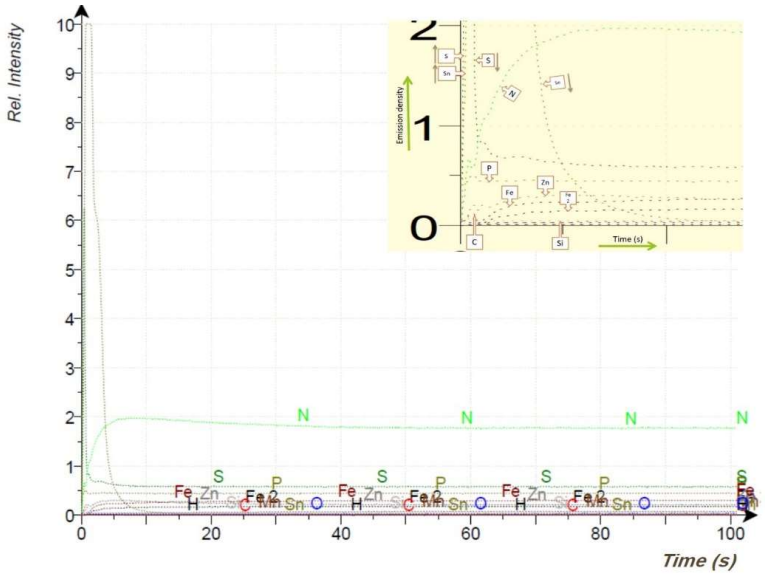

Figure 11. GDOES result of non-passivated sample.

The GDOES graph in **Figure 12** reveals the chemical composition of the pollution on the passivated surface. Upon closer inspection of the graph, high peak intensities of C, S, Zn, and Si were observed in the first moments along with abundant Sn, which declined over time. Cr also had a strong peak that completely dropped with time. Based on the peaks of N, P, Zn, Fe, and Si in the early moments, of the test, it can be concluded that in very thin profiles of the surface, Sn, S, Cr, N, P, Zn, Fe, Mn, C, and Si exist, representing the chemical composition of the pollution on the surface. In terms of priority element detection, Sn, S, N, P, Cr, Zn, Fe, Mn, and Si were the most apparent.

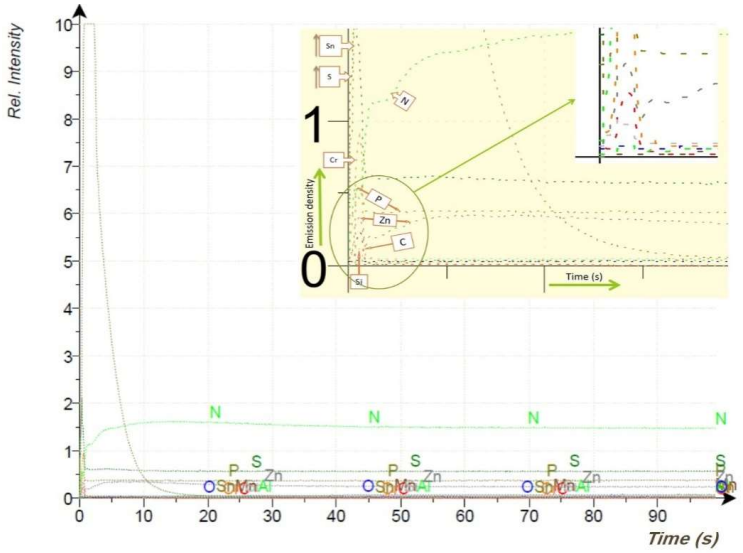

Figure 12. GDOES result of passivated sample.

Comparing the ICP results with the GDOES results shows remarkable similarities in the elements that represent the placement of unwanted elements on the Sn coating layer during electrolysis.

Applying a coefficient of 50 times on the display of S, P, and N, S and before Sn are revealed as the first element in the non-passivated sample in GDOES. This suggests that S exists on the surface of the entry strip to the passivation cell, which can prevent a correct cathodic dichromate passivation process and also dissolve in the passivating solution, infecting it as an unwanted element. S is also observable in the ICP results of the plating electrolyte as well as the passivation solution. According to GDOES analysis, nitrogen and phosphorus were found to be located beneath the strip surface, following the detection of sulfur and tin. The increase in nitrogen emissions and decrease in tin emissions suggest that the nitrogen source may be either the tin plating or surface melting sections. Phosphorus, on the other hand, is believed to have been transferred from the cleaning section to the plating section during strip processing. Si was observed in the passivation solution ICP results (**Table 2**) and contributed to an early peak in the GDOES results of the passivated sample (**Figure 12**). Cr, as well as Sn, S, N, and P, were detected in the passivated sample results. The presence of Sn in the GDOES results was attributed to its presence in the passivation solution rather than the coating process. The sequence of element detection in the passivated sample revealed the interference of C and Zn in the passivation process, with C and Zn being detected after Cr. The significant presence of C in both the EDS and GDOES results of the passivated sample indicates that the strip carries a certain amount of plating electrolyte as it passes through the cells in the line.

The experimental findings necessitate several key recommendations to enhance food packaging material quality and safety. These include the implementation of stringent monitoring protocols throughout the manufacturing process, focusing on critical stages like passivation, and refining processes to minimize the transfer of unwanted elements between different manufacturing cells. Thorough evaluation of raw materials before their use, alongside establishing stringent quality assurance measures and investing in ongoing research to explore alternative surface treatment methods, are also crucial. By adopting these measures, the study aims to reduce the presence of contaminants on tin plate surfaces, ultimately ensuring safer food contact and compliance with stringent regulatory standards. This proactive approach not only mitigates risks associated with potential contamination but also fosters long-term consumer confidence in the safety and quality of packaged food products.

4. Conclusion

The outcomes from the previous chapter's discussions are as follows:

The SEM analysis of passivated samples uncovered rolling grooves on the surface, displaying alternating dark and light areas. The tall areas in the dark regions contained elevated levels of Fe and unwanted C, while both dark and light areas revealed the presence of Cr. The light regions, rich in Sn and significant amounts of unwanted C but lacking O, indicated the presence of Sn oxide in these areas. The melting process on the surface resulted in differential Sn thickness between dip and tall regions due to the liquid Sn filling the lower areas. For non-passivated samples, impurities adhered solely to the Sn layer, indicating transfer from plating cells. EDS analysis of these impurities showcased unwanted elements in sequence—O, Fe, Cl, S, C, Mg, Al, Si, Ca, and Na. The ICP analysis of plating electrolyte coating uncovered significant unwanted elements caused by the steel strip stoppage during its 14 years of use, alongside impurities in raw materials (PSA, ENSA, Sn anode). GDOES highlighted the detection sequence—S, N, Sn, P, Zn, C, and Fe—on non-passivated samples, indicating their transfer between cells. Passivation solution ICP results emphasized Cr as the major element, with notable

amounts of Sn, Si, S, and Fe. S, N, and P were detected beneath the surface layer in both passivated and non-passivated samples, while GDOES of passivated samples indicated initial high-intensity peaks of various elements, diminishing over time due to surface pollution's chemical composition. These findings suggest the transfer of unwanted elements from previous process cells during passivation electrolysis, adsorbing on the surface due to polarization and compounding surface elements at the passivation cell entrance.

Author contributions

Conceptualization, AM and RAN; methodology, ENV; software, AM; validation, RAN, AF and EA; formal analysis, AM; investigation, ENV; resources, AM; data curation, ENV; writing—original draft preparation, ENV; writing—review and editing, AM; visualization, RAN; supervision, RAN; project administration, RAN; funding acquisition, RAN. All authors have read and agreed to the published version of the manuscript.

Conflict of interest

The authors declare no conflict of interest.

References

1. Wester PA. Chapter 3—Hazards, the hazard analysis, and the food safety plan. In: *Hazard Analysis and Risk Based Preventative Controls: Building a (Better) Food Safety Plan*. Academic Press; 2018. pp. 43–65. doi: 10.1016/B978-0-12-810500-9.00003-5
2. Akyil C, Akdas G, Afsin P, Ürgen M. Freestanding SnO_2 films produced with anodic polarization in acidic media containing colloidal tin hydroxides. *Materials Chemistry and Physics* 2019; 221: 263–271. doi: 10.1016/j.matchemphys.2018.09.062
3. Al-Ghamdi S, Rasco B, Tang J, et al. Role of package headspace on multilayer films subjected to high hydrostatic pressure. *Packaging Technology and Science* 2019; 32(5): 247–257. doi: 10.1002/pts.2432
4. Ren Y, Huang Z, Wang Y, et al. Friction-induced rapid amorphization in a wear-resistant $(CoCrNi)_{88}Mo_{12}$ dual-phase medium-entropy alloy at cryogenic temperature. *Composites Part B: Engineering* 2023; 263: 110833. doi: 10.1016/j.compositesb.2023.110833
5. Zhou Q, Hua D, Li S, et al. Design and characterization of metallic glass/graphene multilayer with excellent nanowear properties. *Friction* 2022; 10(11): 1913–1926. doi: 10.1007/s40544-021-0581-6
6. Melvin C, Jewell E, Miedema J, et al. Identifying interlayer surface adhesion failure mechanisms in tinplate packaging steels. *Packaging Technology and Science* 2019; 32(7): 345–355. doi: 10.1002/pts.2443
7. Xu F, Shi Y, Yang J, Yan S. Corrosion failure analysis of lightweight tinplate in protein beverage. *IOP Conference Series: Materials Science and Engineering* 2019; 538(1): 012018. doi: 10.1088/1757-899X/538/1/012018
8. Zhao Y, Yin X, Shen P, et al. Passivation and chemical conversion combined multi-elements coating on low Sn-coated steel for corrosion protection. *Journal of the Electrochemical Society* 2022; 169(8): 082501. doi: 10.1149/1945-7111/ac7efa
9. Cova Caiazzo F, Brambilla L, Montanari A, Mischler S. Chemical and morphological characterization of commercial tinplate for food packaging. *Surface and Interface Analysis* 2018; 50(4): 430–440. doi: 10.1002/sia.6386
10. Wang M, Wang Z, Li D, Li N. Study of topography and distribution state of the nanoscale passivation film on a rough tinplate surface. *Coatings* 2018; 8(3): 94. doi: 10.3390/coatings8030094

11. Chen S, Xie L, Xue S. X-ray photoelectron spectroscopy investigation of commercial passivated tinplate surface layer. *Applied Surface Science* 2013; 276: 454–457. doi: 10.1016/j.apsusc.2013.03.115
12. Sun J, Qi GC, Tan Y, An CQ. Characterization of chromate conversion film on tinplate substrate by XPS and electrochemistry methods. *Surface and Interface Analysis* 2009; 41(6): 449–452. doi: 10.1002/sia.3040
13. Azzerri N, Ingo G, Battistoni C, et al. A critical evaluation of electroanalysis methods for the determination of chromium species in passivation layers on tinplate by X-ray photoelectron spectroscopy. *Surface Technology* 1984; 21(4): 391–404. doi: 10.1016/0376-4583(84)90137-7
14. Chang KH, Hurley BL, Pascall MA, Frankel GS. Corrosion in tinplate cans used for food storage, part 3: Effects of cysteine, NaCl, and tomatoes on corrosion of tin, iron, and tinplate. *Corrosion* 2022; 78(2): 127–141. doi: 10.5006/3963
15. Cui GF, Wang JH, Li N, Huang XQ. A single precursor pit for pitting corrosion on defect of tinplate alloy layer visualized by atomic force microscopy. *Materials Chemistry and Physics* 2006; 97(2–3): 488–493. doi: 10.1016/j.matchemphys.2005.08.052
16. Černík M, Gburík R, Hrabčáková L, Vranec P. Texture analysis of tinplate steel and its application in production of double reduced high strength tinplate grades with controlled earing properties. *IOP Conference Series: Materials Science and Engineering* 2015; 82(1): 012108. doi: 10.1088/1757-899X/82/1/012108

Materials Technology Reports 2023; 1(1): 459.
Original Research Article

Effects of pyrolyzed Buxus sempervirens ingredient as micro and bio fillers on polystyrene: Spectroscopic characteristics

Hamed Nazarpour Fard

Department of Organic Chemistry, Faculty of Chemistry, Lorestan University, Khoram -Abad 6815544316, Iran; Nazarpoorfard@gmail.com

ARTICLE INFO

Received: 20 September 2023
Accepted: 27 October 2023
Available online: 20 December 2023

doi: 10.59400/mtr.v1i1.459

ABSTRACT: In this study, *Buxus sempervirens* leaf ingredient (LP) and the carbon (LC) and the ash (LA) were obtained, which are the bio-originated materials. Carbon and ash obtained from this natural plant were prepared by heating and pyrolysis for 2 h at 250 ℃ and 700 ℃, respectively. Then, the solution casting method was used to prepare the composites of these bio-additives with polystyrene. Next, the effects of the additives on diffuse reflectance spectroscopy (DRS) and X-ray diffraction (XRD) spectra of polystyrene were investigated. In addition, the additives led to noticeable changes in X-ray diffraction results, implying a change in the morphology of the polymer. All of these observations imply the uniform formation of the polystyrene (PS) composites with the micro and bio-fillers.

KEYWORDS: polystyrene; Buxus sempervirens ingredient; bio-composite; spectroscopy

1. Introduction

Agricultural and vegetable wastes are associated with some environmental issues that need to be solved. Using these residual materials in various composite materials is a way utilized in many research and industrial applications. For example, Nazarpour-Fard et al. used *Buxus sempervirens* ingredients for modifying the polyvinylpyrrolidone (PVP) properties[1]. Also, they utilized the rice husk ash for modifying the thermal, hydrophilicity, and spectroscopic characteristics of polyvinylpyrrolidone and polystyrene[2,3], thermal characteristics of chitosan[4], and mechanical properties of linear low-density and high-density polyethylene[5].

Polystyrene is one of the famous thermoplastics used in various fields and its composites with various micro and nano materials have been studied and practically used. It should be noted that the suspension method is one of the common and widely used methods in the synthesis of polystyrene[6,7].

Solution casting is the most common method used to prepare polymer and non-polymer composites. In this procedure, all components of the composite are dissolved in a suitable solvent, and after the evaporation of the solvent and drying of the sample, the desired composite is prepared. For example, we can refer to many research studies such as the preparation of graphene oxide/polyaniline/polystyrene composites[8]. Moreover, Yadav et al.[9] employed this procedure for preparing poly (methylmethacrylate)-$BiFeO_3$Polystyrene-2% divinyl benzene composites[9].

The preparation of polymer composites from biomaterials has attracted increasing attention due to the excessive consumption and exploitation of non-renewable resources such as coal and oil. In this context, the composite compounds obtained from plant wastes have received more attention owing to their abundance and in order to protect the environment. For instance, the leaves of various plants are widely used resources that can be utilized in many research and industrial fields[10,11]. In other studies,

chitosan/pectin-rich vegetable waste composites were successfully prepared for use in the active packaging of dry foods[12]. Also, Cherkashina et al. employed *Hazelnut Shells* as a valuable additive for modifying polystyrene properties[13]. Moreover, Nazarpour-Fard used bio-additives prepared from rice husk to modify the polystyrene and polyvinylpyrrolidone characteristics and obtained valuable results[1–5].

Here, based on the above-mentioned explanations and for protecting the environment and the correct use of plant and environmental wastes, it was decided to use the waste of *Buxus sempervirens* ingredient (which is left into the environment as a waste originated from biomaterial) as an additive for polystyrene composites. Its carbon and ash derivatives obtained by thermal pyrolysis, were also used as bio-derived and valuable additives to prepare polystyrene composites. These additives showed the observable effects on the DRS and XRD spectra of the polymer, which will be discussed detailly in the next sections.

2. Experimental

2.1. Materials

Polystyrene was synthesized by suspension polymerization method based on the published article[14], as its schematic representation has been shown in **Figure 1**. Toluene (used to dissolve polystyrene) was manufactured by Merck, Germany. The carbon and ash materials were obtained by thermal pyrolysis method in a laboratory furnace as previously reported by Nazarpour-Fard et al.[1–5].

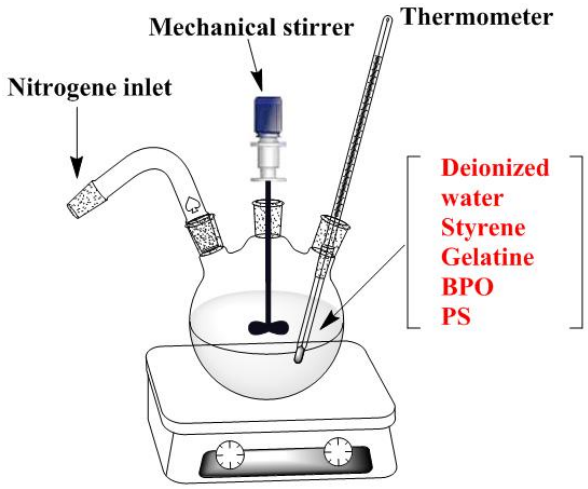

Figure 1. Schematic of the system for polystyrene synthesis.

2.2. Instrumentation

The sonication of the solutions was carried out by using an ultrasonic bath (Sono Swiss, Sw3H, Switzerland). Knauer Instrument (Germany) was used as gel permeation chromatography (GPC) for determining the average molecular weight and polydispersity index of the prepared polystyrene. X-ray diffraction (XRD) analysis was performed on a Philips diffractometer (PW1840 made in Holland Netherlands) with Cu-Kα radiation. burning the plant waste to provide the favorite carbon and ash was done by using a Nabertherm furnace (made in Germany) adjustable up to the temperature of 3000 °C. Visible Reflection Transmission Spectra (DRS) was taken using a Shimadzu UV-2100 spectrometer.

2.3. Polystyrene synthesis

The process of polymer synthesis was carried out as radical suspension polymerization. Here, deionized water (250 cm^3) and gelatine (1.25 g) were poured into a 500 cm^3 three-neck glass reactor fitted with a nitrogen inlet, a stirrer, and a condenser. 20 $cm^3$of styrene was mixed with 0.5 g of benzoyl peroxide (BPO) and then added into the reactor. The reaction medium was mechanically agitated to prepare the uniform condition for polymerization. The temperature inside the reactor was continuously computed by a thermometer fixed to the reactor system. The temperature of the suspension reaction was gradually enhanced to 95 °C, where the polymerization was done for 3.5 h under nitrogen atmosphere. Then, the synthesized PS particles as uniform granules were filtered and separated, washed with deionized water, and dried in an oven at 60 °C. The example of synthesized PS granules has been reported by Slobodian et al.[14].

2.4. Preparation of carbon and ash from the plant waste

In order to prepare carbon and ash from the waste of plant leaves, the dried waste was first powdered with the size of fine particles by using a ball mill (**Figure 2(a)**). Then it was heated in a laboratory furnace at the temperature of 250 °C for 2 h to turn into a carbon material (**Figure 2(b)**). Additionally, it was passed through a sieve with 200 mesh to be used in the preparation of polymer composites as a bio-additive. The process of ash preparation (**Figure 2(c)**) was also done in the same way but at the temperature of 700 °C.

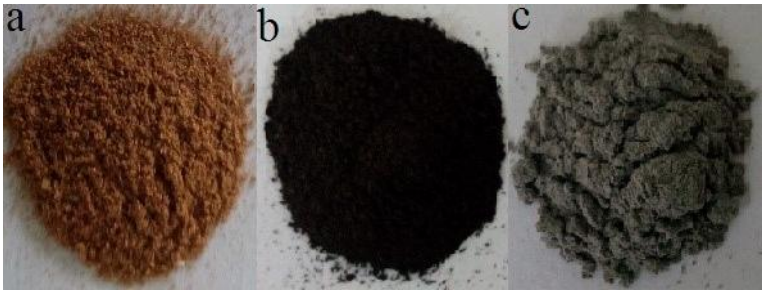

Figure 2. Image of **(a)** *Buxus sempervirens* leaf ingredient, and **(b)** carbon and **(c)** ash obtained from this type of plant waste.

2.5. Preparation of polystyrene composites with the additives

To prepare a polystyrene composite, a polystyrene solution was obtained in toluene solvent at ambient temperature. Then, using mechanical and ultrasonic stirring methods, the additives were well distributed in the polystyrene solution. The polystyrene composites with *Buxus sempervirens* leaf ingredient (PS-L), carbon (PS-C), and ash (PS-A) were prepared through the evaporation of toluene by drying process at a suitable temperature. The composition of the additives in all the composites was 2 wt%.

3. Results and discussion

3.1. Identification of polystyrene by gel permeation chromatography (GPC)

The molecular weight and molecular weight distribution (PDI) of the synthesized polystyrene were determined through gel permeation chromatography analysis. The results of these investigations are shown in **Figure 3** and **Table 1**. As it is clear that, the weight and number average molecular weights are 33,949 and 19,905 g mol^{-1}, respectively. It was found that the polydispersity index (molecular weight distribution) value of the synthesized polystyrene (1.705) was in accordance with that of commercial PS as formerly reported by Chen et al.[15].

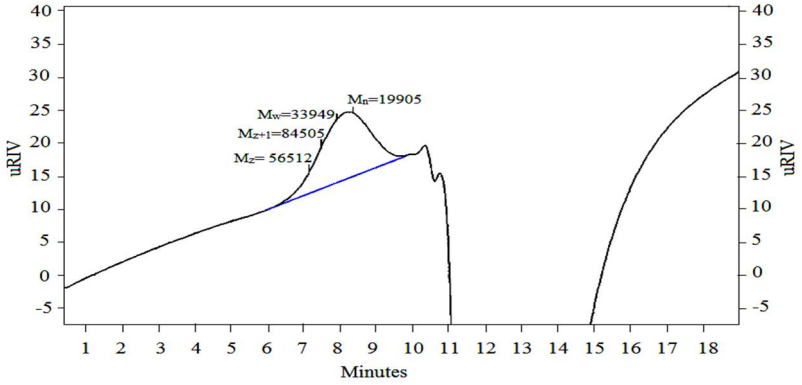

Figure 3. GPC chromatogram for the synthesized polystyrene.

Table 1. Average molecular weight and molecular weight distribution of synthesized polystyrene.

Characteristic	Amplitude
Weight average molecular weight ($\bar{M}_w$)	33,949 g mol^{-1}
Number average molecular weight ($\bar{M}_n$)	19,905 g mol^{-1}
Z average molecular weight	56,512 g mol^{-1}
Z + 1 average molecular weight	84,505 g mol^{-1}
Peak molecular weight	22,409 g mol^{-1}
Polydispersity index	1.705

3.2. The effect of additives on absorption of visible light by polyvinylpyrrolidone and polystyrene

Investigation of the additive effect on the absorption of visible waves by polystyrene composites showed that these additives have an increasing effect on the absorption of visible light by the polymer (**Figure 4**). However, it is clear that after the addition of additives to the polymer matrix, the absorption values of all the composites have increased as compared to the pure polymer. The increasing trend is also proof of the formation of composites with a uniform distribution of particles in the polymer matrix. It is obvious that in the case of composite containing carbon and ash, two peaks have been observed in the range of 400 to 450 nm, which can be due to the presence of functional groups in these additives and/or due to their different interactions with polystyrene, in comparison to PS-LP sample. The similar observations were reported for polyvinylpyrrolidone composites with *Buxus sempervirens* ingredients[1], as well as for chitosan after adding rice husk ash[4].

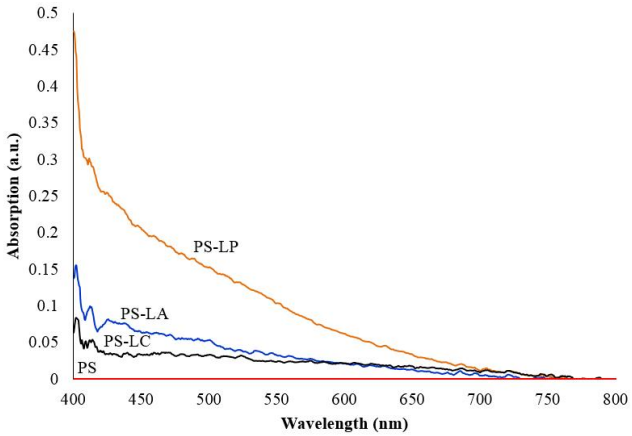

Figure 4. DRS visible spectra for polystyrene and their composites.

3.3. The effect of additives on the XRD pattern of polyvinylpyrrolidone and polystyrene

Examining the XRD results for polystyrene in **Figure 5**, shows that the additives have had significant effects on the XRD pattern of polystyrene. In other words, the addition of carbon and ash to this polymer not only caused the shift of the peak located at around 19.5° to higher degrees but also led to an increase of the full width at half maximum (*FWHM*) of the peak. In the case of PS-LP, we can see no drastic changes. All of these observations show that these additives affect the morphology and crystal structure of polystyrene. But the effects in PS-LC and PS-LA were greater compared to PS-LP, which could be due to stronger interactions and bonds between these bio-additives and the PS matrix. It is worth mentioning that the values of *d*-spacing parameter in all the composites were higher as compared to pure PSS indicating an increase in the size of crystalline particles in the semi-structured samples. It is obvious that molecular arrangement and interactions between the composite components are of the main factors controlling the polymer crystallinity. Moreover, the appearance of new peaks in the XRD patterns of the composites exhibits the creation of new crystalline area in the composites (**Table 2**). Some changes in XRD of PVP and PS have been observed after adding rice husk derivatives as can be seen in the literature [2,3].

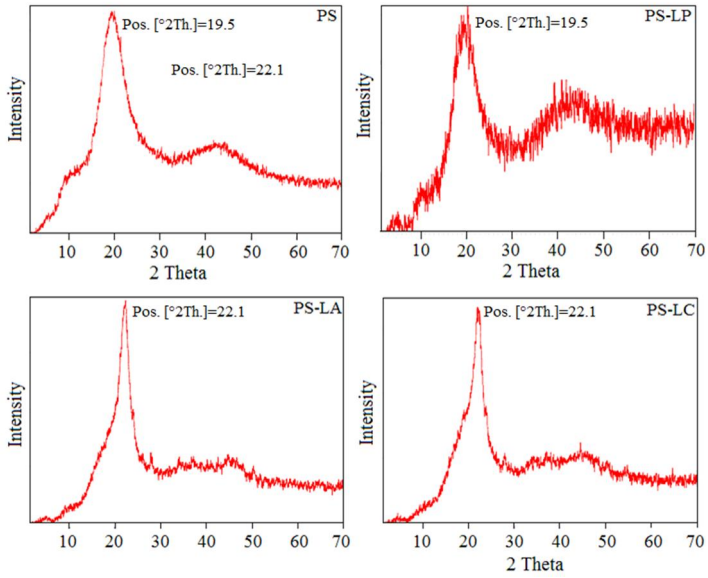

Figure 5. X-ray diffraction spectra of polystyrene and its composites.

Table 2. X-ray diffraction results of the PS samples.

	Peak	Pos. [°2Th.]	Height [cts]	FWHM [°2Th.]	*d*-spacing [Å]	Rel. Int. [%]	Tip width [°2Th.]
PS	1	9.895	86.72	1.92	8.93176	30.86	1.6
	2	23.0265	281.06	1.0184	3.86252	100	0.8487
PS-LP	2	19.743	281.1	1.0612	4.49685	100	0.8843
PS-LC	2	22.3645	1456.49	1.536	3.97203	100	1.28
PS-LA	2	22.289	1892.98	1.5744	3.98863	100	1.6

4. Conclusion

In this research study, polystyrene composites with *Buxus sempervirens* ingredients and the prepared carbon and ash materials were prepared via the solution casting method. The results of DRS and XRD investigations showed that incorporating the biomaterials into the polymer matrix leads to changes in

their spectroscopic results. For example, in the DRS spectrum, polystyrene did not show absorption in the visible region, but the composites showed more absorption compared to the parent polymer. The composites of PS-LC and PS-LA showed a peak at around 400 nm that did not appear in the case of PS-LP composite. The XRD results exhibited that these additives cause shifting of 2θ values of the PS peaks as well as changes in the width of peaks and the *d* parameter. This indicates an alteration in the size of crystals and the morphology of the polymer. The study showed that the derivatives of *Buxus sempervirens* leaf ingredient prepared by pyrolysis can lead to the observable changes in DRS and XRD spectra of polystyrene. Thus, the effects of these additives on other properties of PS and other polymers can be considered interesting studies in the future.

Conflict of interest

The author declares no conflict of interest.

References

1. Nazarpour-Fard H, Rad-Moghadam K, Shirini F. Improved hydrophobic and thermal stability of polyvinylpyrrolidone composites with the ingredients of Buxus sempervirens. *Applied Chemistry* 2018; 13(47): 69–82. doi: 10.22075/CHEM.2018.2900
2. Nazarpour-Fard H. Polyvinylpyrrolidone and polystyrene composites based on economical high quality biofillers derived from rice husk: Spectroscopic and hydrophilic investigations. *Polyolefins Journal* 2023; 10(1): 45–57. doi: 10.22063/POJ.2022.3221.1232
3. Nazarpour-Fard H. Composites of polyvinylpyrrolidone and polystyrene with rice husk ash as a bio and silica-rich material: Thermal characteristics and water vapor absorption ability. *Epitoanyag—Journal of Silicate Based and Composite Materials* 2022; 74(6). doi: 10.14382/epitoanyag-jsbcm.2022.33
4. Nazarpour-Fard H, Rad-Moghadam K, Shirini F, et al. Novel improvements in thermal and hydrophobic properties of chitosan reinforced by rice husk ash. *Polymers from Renewable Resources* 2016; 7(4): 115–133. doi: 10.1177/204124791600700401
5. Nazarpour-Fard H. Rice husk ash: Economical and high-quality natural-based reinforcing filler for linear low-density and high-density polyethylene. *Polymers from Renewable Resources* 2022; 13(4): 206–222. doi: 10.1177/20412479221128965
6. Chaudhary V, Sharma S. Suspension polymerization technique: Parameters affecting polymer properties and application in oxidation reactions. *Journal of Polymer Research* 2019; 26(5). doi: 10.1007/s10965-019-1767-8
7. Huang J, Zhao Z, Chen T, et al. Preparation of highly dispersed expandable graphite/polystyrene composite foam via suspension polymerization with enhanced fire retardation. *Carbon* 2019; 146: 503–512. doi: 10.1016/j.carbon.2019.02.029
8. Das M, Sethy PP, Sundaray B. EMI shielding performance of graphene oxide reinforced polyaniline/polystyrene solution cast thin films. *Synthetic Metals* 2023; 296: 117369. doi: 10.1016/j.synthmet.2023.117369
9. Yadav NP, Sahu BB, Mahaling RN, et al. Superior dielectric and electrical characteristics of poly(methylmethacrylate) (PMMA)-$BiFeO_3$-Polystyrene-2% divinyl benzene (PDB) composites. *Optik* 2023; 277: 170695. doi: 10.1016/j.ijleo.2023.170695
10. Bavasso I, Marzi D, Bracciale MP, et al. Plant waste as green reinforcement for polymer composites: A case study of Pteris vittata roots. *Journal of Natural Fibers* 2022; 20(1). doi: 10.1080/15440478.2022.2135669
11. Kinyanjui Muiruri J, Chee Chuan Yeo J, Yun Debbie Soo X, et al. Recent advances of sustainable short-chain length polyhydroxyalkanoates (Scl-PHAs)—Plant biomass composites. *European Polymer Journal* 2023; 187: 111882. doi: 10.1016/j.eurpolymj.2023.111882
12. Merino D, Bellassi P, Paul UC, et al. Assessment of chitosan/pectin-rich vegetable waste composites for the active packaging of dry foods. *Food Hydrocolloids* 2023; 139: 108580. doi: 10.1016/j.foodhyd.2023.108580
13. Cherkashina NI, Pavlenko ZV, Pushkarskaya DV, et al. Synthesis and properties of polystyrene composite material with hazelnut shells. *Polymers* 2023; 15(15): 3212. doi: 10.3390/polym15153212
14. Slobodian P, Pavlínek V, Lengálová A, et al. Polystyrene/multi-wall carbon nanotube composites prepared by suspension polymerization and their electrorheological behavior. *Current Applied Physics* 2009; 9(1): 184–188. doi: 10.1016/j.cap.2008.01.008

15. Chen CM, Hsieh TE, Ju MY. Effects of polydispersity index and molecular weight on crystallization kinetics of syndiotactic polystyrene (sPS). *Journal of Alloys and Compounds* 2009; 480(2): 658–661. doi: 10.1016/j.jallcom.2009.02.003

Materials Technology Reports 2023; 1(1): 103.
Review Article

A brief review on systematic approach to polymer selection for development of capillary/hollow-fibre membrane for practical applications

Vijay Suresh Mamtani[1,2], Asim Kumar Ghosh[1,2,*], Asis Kumar Adak[2]

[1] *Homi Bhabha National Institute, Anushaktinagar, Mumbai 400094, India*

[2] *Desalination & Membrane Technology Division, Bhabha Atomic Research Centre, Mumbai 400085, India*

*** Corresponding author:** Asim Kumar Ghosh, akghosh@barc.gov.in

ARTICLE INFO

Received: 29 June 2023
Accepted: 25 July 2023
Available online: 20 October 2023

doi: 10.59400/mtr.v1i1.103

ABSTRACT: Polymeric membranes are widely used for treatment of lean stream in chemical process industries. These membranes are used in different configurations such as tubular, plate & frame, disc-tube, spiral and capillary/hollow-fibre. Membrane modules with capillary/hollow-fibre configuration appears promising in ultrafiltration applications due to its relatively higher packing density, ease of backwashing, ease of cleaning and lower pressure drops since it can be operated at laminar flow regime with high cross-flow velocity. Hence, efforts are being made by researchers to make capillary/hollow-fibre membrane modules from various polymers, ranging from most hydrophilic polyacrylonitrile (PAN) to super-hydrophobic polypropylene (PP) and polytetrafluorethylene (PTFE). Here, we discuss the qualifying properties of the polymeric materials suitable to spin into capillary/hollow-fibre ultrafiltration membranes. Selection of polymers for making fibres requires in-depth knowledge of properties of base polymer and its processability/fabricability. The important properties to be considered for making capillary/hollow-fibre membrane are intrinsic structural properties of the base polymer like degree of crystallinity, tensile strength, tensile modulus, etc. The functional properties such as permeability, hydrophilicity/hydrophobicity etc. also plays role in selecting polymer for a given application. The polymer should also have appreciable dissolution in available solvents or should have degradation temperature higher than melting point so that it can be processed through appropriate membrane preparation process.

KEYWORDS: Polymers; membranes; capillary; hollow-fibre; ultrafiltration

1. Introduction

A membrane is a physical barrier that allows preferential transport of one or more specie over other, thus causing separation. The main advantages of membrane separation systems are its compact size, no additives requirement, ambient temperature operation, low specific power consumption, etc. In addition, owing to its modular nature, it can be easily scaled up and scaled down, as well as it can be easily integrated with other separation or reaction processes[1]. The polymeric membranes are widely deployed in industrial applications such as water treatment, gas separation, pretreatment of seawater, desalination using reverse osmosis membrane, fruit juice concentration using forward osmosis membrane and in separations process of the dairy, paper, textile industries, etc.[2]. It can be used in different module

configurations such as tubular, plate and frame, disc tube, spiral and capillary/hollow-fibre. The capillary/hollow-fibre module configuration has the highest packing density and thus offer more contact area per unit volume for the separation. Other advantages of capillary module are ease of backwashing and cleaning, operation in laminar flow regime to give lower pressure drop with high cross-sectional velocity.

The capillary/hollow-fibre membranes are cylindrical supportless membrane with diameter in the range of 0.5 mm to 5 mm[3]. As these are supportless membrane, it requires good mechanical strength so as to deploy in the pressurised environment when compared to the supported membranes used in other membrane module configurations. The mechanical properties of the capillary/hollow-fibre membrane depend on the mechanical properties of the polymer from which it is prepared. Polymer selection is therefore one of the important criteria for preparation of the membrane. Intrinsic structural properties of base polymer help in imparting mechanical strength to the final capillary membrane. These properties are degree of crystallinity, tensile strength, tensile modulus, etc. Polymer should also be processable i.e., it should be easily soluble in common solvents or melt before degradation. It should be chemically stable with the process fluids, that is, it should withstand operating pH condition and should not undergo degradation or oxidation. It should be thermally stable and work without degrading at required temperature condition. In addition, hydrophilicity, adsorption characteristics to avoid fouling, biocompatibility plays crucial role depending on the field of application. Systematic approach to polymer selection for development of capillary/hollow-fibre membrane for practical applications is not available in the literature.

Several polymers namely, polysulfone (PSf)[4,5], polyethersulfone (PES)[6,7], polyethylene (PE)[8,9], polyvinylchloride (PVC)[10,11], polyvinylidene difluoride (PVDF)[12,13], polypropylene (PP)[14,15], and polyacrylonitrile (PAN)[16] are presently used for making capillary/hollow-fibre membranes. Different processes viz. Non-Solvent Induced Phase Separation (NIPS), Vapour Induced Phase Separation (NIPS), Thermal Induced Phase Separation (TIPS), etc. are used for making capillary/hollow-fibre membranes.

2. Prerequisites of polymer to form a capillary/hollow-fibre membrane

Selection of the proper polymer is the first step of development of any useful membrane. A polymer should have membrane forming properties and fibre forming properties so that it can be used to make capillary/hollow-fibre membrane. In addition, also it is important to understand the polymer properties that can affect the membrane characteristics and performances. **Figure 1** gives the summary of the criteria for polymer selection to prepare capillary/hollow-fibre membranes.

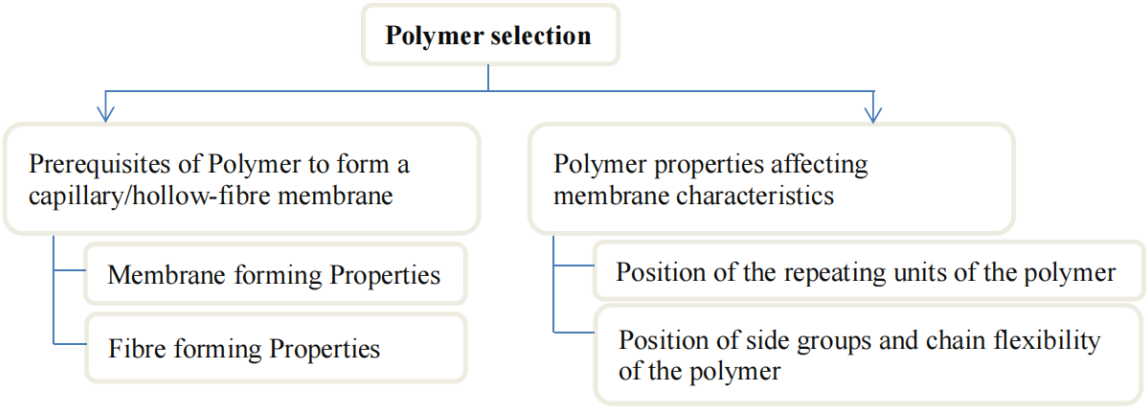

Figure 1. Criteria for polymer selection to prepare capillary/hollow-fibre membranes.

2.1. Membrane forming properties

Polymer forms a membrane film and one of the physical properties of the film formed is its mechanical strength to withstand the operating pressure. This is especially required for support-less capillary/hollow-fibre membranes. Also, the polymer chosen must be compatible and have desired properties required for the application where membrane, prepared from such polymer, is deployed. This restricts the selection of the polymer for preparing a membrane. The capillary/hollow-fibre membrane can be open porous membrane, primarily used in Ultrafiltration (UF) and Microfiltration (MF) or non-porous membranes which find application in pervaporation and gas separation[3]. For the porous membrane, the pore size of the membrane determines membrane performance. The polymer material is selected based on membrane manufacturing requirement, its mechanical strength, fouling tendency, chemical inertness, and thermal stability required in the final membrane. The selection of polymer material is not determined by separation characteristics of the membrane as the separation characteristics are tuned by the process parameters by which membranes are prepared. For example, porous membranes that are prepared by non-solvent induced phase separation (NIPS) method whose separation property is determined by the choice of solvent/nonsolvent, the rate of phase separation, presence of additives, etc.[3].

2.2. Fibre forming properties

Capillary/hollow-fibre membranes can be made from polymers having the fibre forming properties. Fibres are built up by crystallites and less ordered or amorphous regions of the polymer. The crystallites are oriented in such a manner that the molecules from which they are built are parallel with the fibre axis[17]. This orientation can also be imparted during and after the spinning of the capillary/hollow-fibre membrane. The crystallites can be regarded as the high softening reinforcing filler for the disordered regions of the drawn fibres[18]. The entropy factor presents in the macromolecules of the polymer favours return to maximum randomness, however, in the case of fibres, the forces opposing retraction are greater which causes the macromolecules to remain in the extended form which otherwise would have retracted, as in case for rubbers[18].

The polymer crystallinity determines the physical and mechanical characteristics of a fibre which is turn depends on the chemical structure of the polymer and on the manner in which the fibre is built up from the polymer[17]. The chemical structure greatly influences the intermolecular forces. Hydrogen bonding systems, strong polar groups, readily ionisable segments are responsible for inter chain attraction to further increase the crystallinity[18]. Branched-chain in the polymer may result in reducing the packing efficiency, thus reducing crystallinity and departing from fibre properties. Molecular weight also influences the properties of the final fibre formed. The molecular weight of the polymer is usually characterised in terms of intrinsic viscosity (η). Value of η should be 0.5 for most of condensation polymers for achieving fibre forming properties[17]. It should be even higher for better physical properties. Crystalline melting point is another important factor in the fibre forming properties and can be considered as a measure of the stability. Higher crystalline polymer shows higher crystalline melting point[17]. However, it may be noted that higher crystallinity of polymer will lead to difficulties in converting the polymer satisfactorily into the fibre as it may not be easily soluble in solvents for wet spinning and will require higher temperature for melt spinning. Hence, an optimum crystallinity is required for preparation of membranes with desired separation characteristics.

3. Polymer properties affecting membrane characteristics

A brief review of polymer properties affecting the characteristics of the membrane is mentioned in

this section.

3.1. Position of the repeating units of the polymer

A polymer with the same repeating units is said to be a homopolymer, whereas a polymer with different repeating unit is said to be a copolymer. However, a copolymer is considered random if it has sequence of the irregular structural units. Due to the fact that many synthetic rubbers are random copolymers, they cannot be used to prepare capillary or hollow fibres. In a block copolymer, each monomer blocks are linked together to form the chain. The free volume and thus the permeability of produced membranes will increase if the main chain is rigid and the side chains are bulky. Crosslinking of chains of polymers causes reduced solubility of the polymer. Additionally, melt casting will be challenging since it will be more difficult to slide one chain over another, resulting in mobility reduction during membrane preparation as compared to linear chain polymers. Increase in free volume brought on by chain length result in increased permeability. Linearity tends to increase close packing in the polymer material and hence tend to increase the crystallinity. The increase in close packing increases the density. Thus, higher chain length suggests higher density of the polymer and higher crystallinity[19]. The polymer's molecular weight may be used to express the chain length pretty well. Because polymers contain several chains of various lengths, their molecular weight is not uniform. The molecular weight of the polymer is expressed using the number average molecular weight (Mn) and the weight average molecular weight (Mw). The polymer's molecular weight distribution is given by its polydispersity index (PDI), which is Mw/Mn[3]. The optimum molecular weight with narrow molecular weight distribution is desired for preparation of capillary/hollow-fibre membranes with desired properties.

3.2. Position of side groups and chain flexibility of the polymer

The polymers viz. PVDF, PP, PVC, PE, PAN are basically vinyl polymers having chemical formula [–CH_2–CRR'–] repeat units with side group −R and −R' being different for different polymers as shown in **Table 1**. The position of the side group R and R' plays an important role in polymer properties. Based on the arrangement on the side group, the polymer can be classified as isotactic, atactic, syndiotactic[3]. Isotactic arrangement in a polymer is a configuration in which the main chain and the side groups are in the same side, which leads to the formation of crystalline polymers. Isotactic arrangement in a polymer is desired for making capillary fibre. In atactic arrangement in a polymer, random arrangements of side groups are present along the main chain and thus it is non-crystalline in nature. In case of syndiotactic polymer, the configuration is such that main chain and side groups are on the alternate side[3]. This kind of arrangement also gives rise to crystallinity in the polymer, making it suitable to be used in capillary fibre making. However, it must be noted that higher crystallinity reduces permeability in the membrane[20].

Table 1. Vinyl polymers with different side groups.

Polymer	–R	–R'
PE	–H	–H
PVC	–Cl	–H
PVDF	–F	–F
PP	–CH_3	–H
PAN	–CN	–H

The chain flexibility is one of the important characteristics of polymer which affects the membrane mechanical property. Character of main chain and the side chain, if present, decides chain flexibility and

thus the membrane mechanical property. Flexibility in the polymer is attained because of oscillation of atoms about its equilibrium position and because of rotation of certain parts of molecules with respect to each other. The rotation is possible in single covalent bond[21] present in the polymer. Additionally, side groups affect whether rotation around the main chain is easily achievable or difficult due to steric hindrance. Presence of aromatic or heterocyclic groups in the main chain reduces the flexibility but increase chemical and thermal stability[3] as in case of polysulfone and polyethersulfone. Higher flexibility in polymer will impart higher impact strength of the membrane but tensile strength will be lower as compared to the membrane obtained from rigid polymer[19]. The chain interaction and flexibility in the polymer determines its glass transition temperature (Tg). It is the temperature at which the polymer changes its state of amorphous polymer changes glassy to rubbery state. In glassy state, the polymer has high tensile modulus (E) whereas in the rubbery state the polymer has three to four order lower tensile modulus[3]. The polymer chain has restricted motion in glassy state and increase in temperature cause increase in motion and hardly any change in the specific volume of polymer. However, after Tg, the polymer gets converted into rubbery state in which the segments of polymer chain can rotate freely and there is increase in free and specific volume of the polymer, increasing the polymer permeability. Glassy polymers are preferred for capillary/hollow-fibre membrane preparation and most of the time the polymer casting solutions are prepared at higher temperature.

4. Common polymers used for capillary/hollow-fibre membrane preparation: Properties, preparation methods & applications

A list of polymers with their properties/characteristics used for development of useful membranes are given in **Tables 2** and **3** based on several literature search. A summary of the solvents used for dissolution of selected polymer to cast membranes and the methods used for their preparation are given in **Figures 2** and **3** respectively. Schematics of common fibre preparation techniques like nonsolvent-induced phase separation (NIPS) and melt spinning-cold stretching method (MSCS) are given in **Figure 4**.

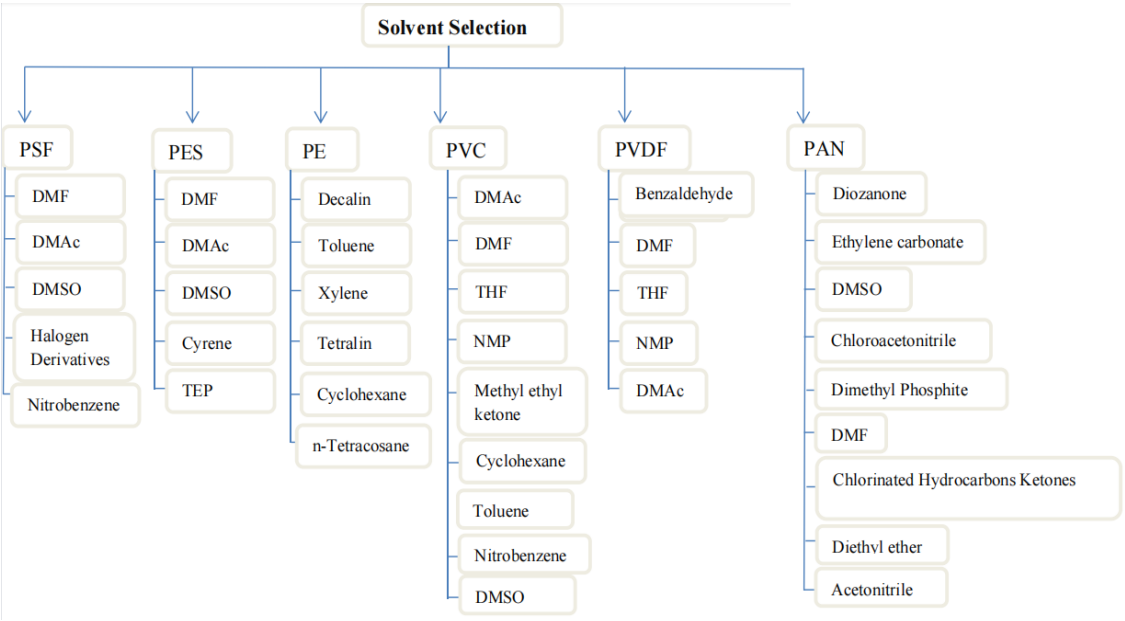

Figure 2. Solvents used for dissolution of selected polymer to prepare casting solution.

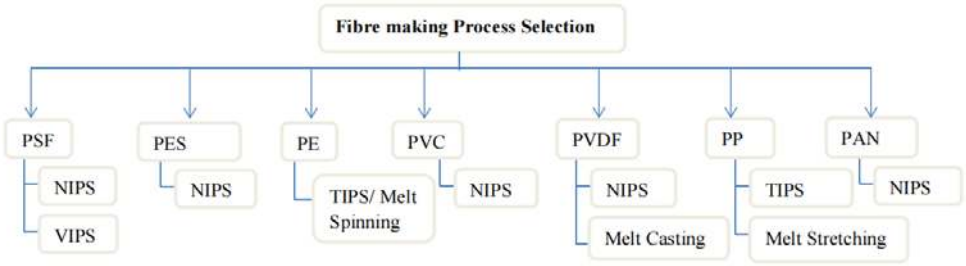

Figure 3. Summary of the methods used for preparation of membranes from selected polymers.

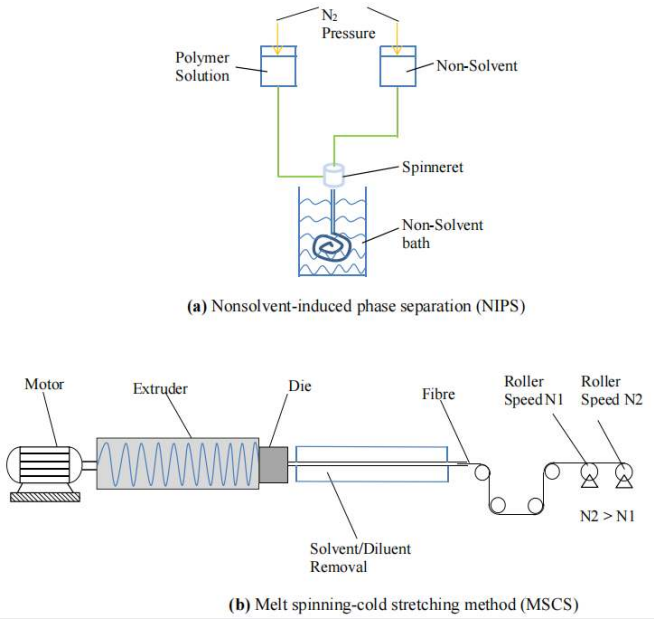

Figure 4. Schematic of **(a)** nonsolvent-induced phase separation (NIPS) and **(b)** melt spinning-cold stretching (MSCS) techniques for fibre preparation.

Table 2. Properties/characteristics of PSf, PES, PVC, PVDF & PAN polymers used to make porous membranes.

Polymer property	**PSf**	**PES**	**PVC**	**PVDF**	**PAN**
Structure	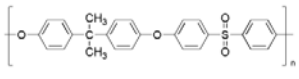	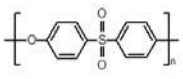	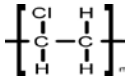	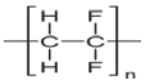	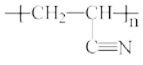
Molecular weight	17,600–58,000	26,000–49,000	43,000–126,000	300,000–700,000	70,000–400,000
Density, g/cm^3	1.24	1.37	1.388	1.675	1.184
Solubility parameter, (MPa)$^{1/2}$	23.7	23.12	19.6	19.2	26.2
Water absorption, (24 h), %	0.2–0.8	0.1–1.7	0.2–1	0.03–0.05	0.3
Tensile strength, MPa	69	82.8	55.5	43	35
Tensile modulus, MPa	2600	2777	276–75,884	1194	350
Thermal expansion coefficient, 10^{-5} K^{-1}	21	5.5	47–62	7–15	6–7
Glass transition temperature Tg, K	459	498	344	239	382
Melting point Tm, K	458–468	493–503	473–573	443–473	593

Table 3. Properties/characteristics of PE & PP polymers used to make porous membranes.

Polymer property	**PE**					**PP**			
	LHDE	LLDE	LDE	MLLDE	Elastomeric	Syndiotactic	Atactic	Elastomeric	Isotactic
Structure	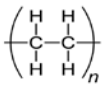					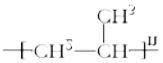			
Molecular weight	1000–8,000,000	50,000–200,000	30,000–40,000	40,000–110,000	-	127,000–290,000	-	-	12,000–585,000
Density, g/cm^3	0.92–0.99	0.912–0.930	0910–0935	-	-	0.91–0.989	0.855	0.868–0.8787	0.85–0.946
Degree of Crystallinity, %	35–90	33–53	33–53	33–53	9–21	21–29	Some/none	9–27	50–70
Solubility parameter, (MPa)$^{1/2}$	16.7	16.7	16.7	16.7	16.7	16.2	16.2	16.2	16.2
Water absorption (24 h), %	0.005–0.01	0.005–0.01	0.005–0.01	0.005–0.01	0.005–0.01	0.01	0.01	0.01	0.01
Tensile strength, MPa	10–60	9–20	9–15	30–48	-	10.85	1–2	3.2–39	23–36
Tensile modulus, MPa	60–290	137–520	102–310	4–700	1.5–12.5	483	-	23–359	482.6
Glass transition Temp. Tg, K	140–155	~193	140–170	~193	221–244	~263	260	265	275.5–283.7
Melting temp. Tm, K	391–419	378–383 & 394–398	378–388	363–398	322–349	398–421	6.1×10^{-3}–9.3×10^{-3}	316.5–433	452

4.1. Polysulfone (PSf)

Polysulfone is a thermoplastic and slightly hydrophilic polymer [water absorption (24 h) <0.3%][22]. It has excellent properties such as good solubility in a wide range of aprotic polar solvents like dimethylformamide (DMF), dimethylacetamide (DMAc), dimethylsulfoxide (DMSO), nitrobenzene etc. It has good mechanical stability of the films (tensile strength: 69 MPa, tensile modulus: 2482 MPa), good stability in oxidative environment (hydrogen peroxide 3%–5%, hypochlorite 5%–7%), good chemical stability, high thermal resistance property with glass transition temperature 'Tg' = 459 K[22] and moderate reactivity in aromatic electrophilic substitutions reactions (sulfonation, nitration, chloromethylation, acylation, etc.[23]. The aromatic ring in the chain of polysulfone gives rigidity to the polymer chain which is reflected in its higher tensile strength. PSf also has high impact strength (80.4 J/m)[22], indicating higher flexibility, and has high tensile modulus. The mechanical properties of PSf make it more resistant to fibre breakage/bursting. As a result, it can withstand higher operating pressure condition. The glass transition temperature 'Tg' is also high owing to presence of aromatic group. The operating temperature can be kept higher because of higher Tg value. However, the thermal expansion coefficient (2.1×10^{-4} K^{-1}[22]) of the PSf is relatively higher. This may decide the operating temperature while using the polymer in capillary/hollow-fibre membrane configuration. Polysulfone membrane can be prepared in fibre form both by non-solvent-induced phase separation (NIPS)[4] & vapor induced phase separation (VIPS)[5].

Common applications of PSf capillary/hollow-fibre ultrafiltration membranes are in pretreatment of seawater desalination, waste water recovery, food and beverage processing, support for thin-film composite membrane preparation etc.[24].

4.2. Polyethersulfone (PES)

Polyethersulfone is a thermoplastic polymer and is relatively more hydrophilic as compared to PSf polymer [water absorption (24 h): 0.43%[22]]. It is widely used as a membrane material for liquid and gas[6] separation processes. The polymer has aromatic ring in its chain giving rigidity to the polymer chain and it is reflected in its mechanical properties. PES polymer is soluble in N, N-dimethylformamide (DMF), N, N-dimethyl acetamide (DMAc), 1-methyl-2-pyrrolidinone (NMP), and dimethyl sulfoxide (DMSO) and also in some of the "green solvents" like Dihydrolevoglucosenone (Cyrene), triethyl phosphate etc. The mechanical properties of PES are better than PSf polymer. It has high very high tensile strength (82.8 MPa), higher tensile modulus (2482 MPa)[22], higher impact strength (85.7 J/m[22]) which will increase its ability to withstand higher operating pressure condition. The glass transition temperature (498 K) is also high due to the presence of aromatic group. It also has lower linear thermal expansion coefficient (5.5×10^{-5} K^{-1}[22]). Thus, operating at higher temperature is possible with PES capillary membrane as compared to PSf membrane. The solubility parameter of PES is 23.12 $(MPa)^{1/2}$[22] and hence it can be processed with more ease than PSf.

Polyethersulfone membrane are being prepared in fibre form by non-solvent-induced phase separation (NIPS)[6,7]. Common applications of PES capillary/hollow-fibre ultrafiltration membranes are in pretreatment of seawater desalination, hemodialysis, biomedical applications, food and beverage processing, support for thin-film composite membrane preparation etc.

4.3. Polyethylene (PE)

Polyethylene is a hydrophobic polymer (water absorption (24 h) <0.02%) and has an advantage of being cost effective polymer, flexible and tough. It offers high impact strength and chemical resistance to acids and aqueous solvents[22]. Polyethylene can be classified based on density and branching as elastomeric/linear high-density (LHD)/linear low-density (LLD)/low-density (LD)/metallocene linear low-density (MLLD). Elastomeric PE is highly branched[22]. It has low packing density and poor tensile modulus (1.5–12.5 MPa). The degree of crystallinity (9%–21%) is also low for elastomeric PE. It has low melting point (322–349 K) and thus cannot be operated at higher temperatures. Hence, it should not be preferred for making capillary/ hollow-fibre membrane. LHD PE has large range of molecular weight (1×10^3–8×10^6 g/mol) and large range of PDI (1.07– > 10^7). It has density of 0.92–0.99 g/cm^3 and has lower melting temperature (391–419 K) restricting its operational temperature range. The degree of crystallinity (35%–90%) is very high indicating very good fibre forming properties. However, the processing of the polymer is difficult. It is soluble only above 353 K in hydrocarbons such as, aromatics, ketones, halogenated hydrocarbons, higher aliphatic esters, di-n-amyl ether, etc. It shows moderate mechanical properties with average tensile modulus (60–290 MPa), average tensile strength (10–60 MPa) and excellent impact strength (30–200 J/m). LLD PE has molecular weight range of 5×10^4–20×10^4 g/mol and narrow range of PDI (4–35). It has density of 0.912–0.930 g/cm^3. It has lower melting temperature (378–398 K) restricting temperature range of operation. The degree of crystallinity (33%–

53%) is very good for forming fibre. The processing of the polymer is difficult. It is soluble in decalin, toluene at 368 K, xylene at 369 K, tetralin at 371 K, cyclohexene at 341 K, n-tetracosane at 374 K. It shows moderate mechanical properties with good tensile modulus (137–520 MPa), average tensile strength (9–20 MPa) and very good impact strength (53.0 J/m)[22].

Low density PE has molecular weight range of 3×10^4–40×10^4 g/mol and narrow range of PDI (4–30). It has density of 0.910–0.935 g/cm^3 and lower melting temperature (378–388 K) and thus restricting temperature range of operation. The degree of crystallinity (33%–53%) is very good for forming fibre. The processing of the polymer is difficult. It is soluble in decalin, toluene at 368 K, xylene at 369 K, tetralin at 371 K, cyclohexene at 341 K, n-tetracosane at 374 K[22]. It shows moderate mechanical properties with average tensile modulus (102–310 MPa) and average tensile strength (9–20 MPa). MLD PE has molecular weight range of 4×10^4–11×10^4 g/mol and narrow range of PDI (2–2.5). It has density of 0.910–0.935 g/cm^3 and has lower melting temperature (363–398 K), thus restricting temperature range of operation. The degree of crystallinity (33%–53%) is very good for forming fibre. It shows moderate mechanical properties with average tensile modulus (4–700 MPa), average tensile strength (30–48 MPa) and excellent impact strength (2500 J/m)[22].

As solubility of LHDPE, LLDPE and LDPE is only at higher temperature near to their melting point, hence melt spinning (melt-extrusion/cold-stretching methods) should be preferred to avoid any involvement of solvent or additive. LHDPE and LDPE can be used together or separately to make PE membrane in fibre form by melt spinning process or thermally induced phase separation (TIPS) method[8,9]. PE membranes are used in organic solvent filtration, sea water desalination by membrane distillation (MD), alkaline fuel cells, air filtration, environment monitoring, biomedical and biotechnology applications[25–27].

4.4. Polyvinylchloride (PVC)

PVC is a thermoplastic polymer having molecular weight in the range of 33×10^3–67×10^3 g/mol, with PDI of 2.01–2.44. It is a slightly hydrophilic polymer (water absorption (24 h) 0.03%–0.45%) and has a density of 1.26–1.5 g/cm^3[22]. It is a cheap polymer having very good mechanical strength and excellent chemical resistance towards halogens, inorganic acids, alkalis, and some of the organic solvents[10]. Some of the solvents that are used for making PVC solution are DMF, DMSO, NMP, DMAc, etc.[10,22]. Nonsolvent of PVC include alcohols, hydrocarbons, acetone, non-oxidizing acids, etc.[22]. PVC has low to very high degree of crystallinity (11.3%–84.2%). For making fibre of PVC polymer, a higher degree of crystallinity must be selected keeping processability factor in consideration. PVC has a very high melting temperature (473–573 K) but lower Tg value (344 K) and relatively high thermal expansion coefficient (4.7×10^{-4}–6.2×10^{-4} K^{-1})[22], so the operating temperature should be limited so as to avoid fibre failure. It shows good mechanical properties with average to excellent tensile modulus (276–75,884 MPa) and good tensile strength (55.5 MPa) making it suitable to deploy in applications requiring relatively high operating pressure[22].

PVC membrane in fibre form is prepared by non-solvent-induced phase separation (NIPS)[10,11]. PVC membrane in fibre form can be used in water treatment, oil-water separation and gas separation applications[11,28–30].

4.5. Polyvinylidene difluoride (PVDF)

PVDF is a thermoplastic fluoropolymer. The molecular weight of the polymer is 3.4×10^4–40×10^4 g/mol and PDI is 1.62–2.14. It is slightly hydrophollic polymer (water absorption (24 h) <0.04%; contact

angle with water 82°)[22]. It is highly resistance to chemicals with no effect of inorganic acids; halogens; oxidants; weak bases; chlorinated solvents, etc.[22]. Common solvents of PVDF include benzaldehyde, DMF, THF, NMP, DMAc, etc. PVDF has high degree of crystallinity (50%)[22] which is desirable for making fibre. PVDF has high melting temperature (443–473 K) with low thermal expansion coefficient (0.7×10^{-4}–1.5×10^{-4} K^{-1}) and so operating at relatively higher temperature is possible. It shows good mechanical properties with moderate tensile modulus (1194 MPa) and average tensile strength (43 MPa). Thus, use of PVDF should be limited to applications requiring moderate operating pressure.

PVDF membranes in fibre form are prepared mostly by non-solvent-induced phase separation (NIPS)[12,13], and sometime using melt spinning method[31]. PVDF membrane in fibre form are used in vacuum membrane distillation (VMD)[12], water treatment, non-aqueous ultrafiltration applications, etc.[32,33].

4.6. Polypropylene (PP)

Polypropylene is a thermoplastic & hydrophobic polymer (water absorption (24 h): 0.01%, advancing contact angle for isotactic PP: H_2O; 116° at 298 K). It is a low-cost polymer having moderate mechanical strength and excellent chemicals resistance[22]. No common solvent can dissolve PP at room temperature and hence melt spinning process is usually used to prepare PP capillary/hollow-fibre membrane. PP can be of syndiotactic, atactic, elastomeric or isotactic macromolecular configuration. Atactic PP has some/none crystallinity and has poor mechanical properties with tensile strength: 1–2 MPa[22]. Hence atactic PP can't be used as it is to prepare membrane in fibre form but can be used along with syndiotactic or isotactic PP[14]. Atactic PP has a density of 0.855 g/cm^3 whereas syndiotactic PP has density in range of 0.91–0.989 g/cm^3. Syndiotactic PP has moderate degree of crystallinity (21%–27%) and hence can be used to prepare membrane in fibre form. It has melting temperature in the range of 398–421 K and has average tensile modulus (483 MPa). Thus, it can be operated at moderately high temperature and at moderate operating pressure. Elastomeric PP has density in range of 0.8683–0.8787g/cm^3 with low to moderate degree of crystallinity (9%–27%). Elastomeric PP has melting temperature in the range of 316.5–433 K which is low to moderate range and is influenced by the degree of crystallinity (as the degree of crystallinity increases it increases melting temperature of the polymer). It has average tensile modulus (23–359 MPa) and average tensile strength (3.2–39 MPa). Hence a proper choice of elastomeric PP having relatively higher degree of crystallinity should be made so as to obtain membrane in fibre form having good mechanical properties. Isotactic PP has density in range of 0.85–0.946 g/cm^3. It has very high degree of crystallinity (50%–70%) and hence is best suited for making membrane in fibre form but the pore sizes created will be expected to be smaller as compared to elastomeric or syndiotactic PP membrane. It has melting temperature in the range of 433–439 K which is quite high and has low thermal expansion coefficient (6.5×10^{-5}–14×10^{-5} K^{-1}). Thus, the membranes can be operated at higher temperature range. It has average tensile strength (23–36 MPa) with very low impact strength (23–36 J/m) and thus operating pressure has to be limited for applications involving PP membrane in fibre form.

At present, PP capillary/hollow-fibre membranes are prepared by the melt spinning-cold stretching method (MSCS) and thermally induced phase separation method (TIPS) methods[34,35]. PP membranes in fibre form are used in membrane contactors, supported liquid membranes, gas separations, pervaporation, ultrafiltration, and microfiltration etc.[14,25,36].

4.7. Polyacrylonitrile (PAN)

Polyacrylonitrile is a thermoplastic and semi crystalline organic polymer. Although it is a thermoplastic polymer, it degrades before melting and hence melt spinning can never be used for preparing PAN membrane in fibre form. Common solvents of PAN include NMP, DMF, dioxanone, ethylene carbonate, DMSO, sulfuric acid, nitric acid, etc. PAN has moderate degree of crystallinity (18%–30%)[37] which is desirable for making fibre. PAN has high melting temperature (593 K)[22], but it degrades at lower temperature and hence operation temperature is restricted by degradation temperature of PAN. It has average tensile modulus (350 MPa) with average tensile strength (35 MPa)[27] and thus operation of the fibre made of PAN should be limited to moderate operating pressure. Due to the presence of highly reactive-CN group, the synthetic modification via post functionalization of PAN is an additional freedom for incorporation of improved properties in the membrane which can increase the number of targeted applications. The synthetic modifications can be the reactions such as nucleophilic addition, cycloaddition, and hydrolysis using various reagents.

PAN membrane in fibre form can be prepared by non-solvent-induced phase separation (NIPS)[16]. As polyacrylonitrile membranes are more hydrophilic compared to common polymeric membranes such as PVDF, PE, PP and PSf, they are less prone to fouling in aqueous solutions. PAN membrane in fibre form is used in pervaporation process, treatment of industrial wastewater, fabrication of the substrate of composite membranes and air filtration[38].

5. Summary & conclusions

Even though it was developed as early as 1960 s, but capillary/hollow fibres membranes have been prepared using a limited number of polymeric materials as on today. Various polymers namely, polysulfone (PSf), polyethersulfone (PES), polyethylene (PE), polyvinylchloride (PVC), polyvinylidene difluoride (PVDF), polypropylene (PP) and polyacrylonitrile (PAN) that are commonly used for preparing capillary/hollow-fibre membrane were reviewed with respect to their properties which qualifies them to be selected for making useful membrane along with their process of making and application areas. The membrane forming and the fibre forming properties of the polymer are essential for qualifying a polymer to be selected for making capillary/hollow-fibre membranes. The mechanical and physical properties of the polymer which are essential for forming fibre are directly influenced by crystallinity of the polymer which in turn is dependent on the chemical structure of the polymer. A general observation from the 'degree of crystallinity' data of selected polymers, which are presently used for preparing capillary membranes, suggests that the degree of crystallinity should be between 20%–50%. Lower value of degree of crystallinity may not lead to fibre formation while higher value may cause difficulties in fabrication. Higher values of tensile strength and tensile modulus of a polymer suggest better mechanical properties, which is desirable for making capillary membrane. From the observation of data of selected polymer, it can be concluded that the gross values of tensile strength should be more than 30 MPa and tensile modulus should be more than 150 MPa for making capillary/hollow-fibre membrane useful to operate at high pressure range. In addition to mechanical and physical properties of the polymer, thermal stability, chemical stability, hydrophilicity, etc. are also important parameters to be considered before selecting a polymer for making capillary/hollow-fibre membrane for a particular application. Based on the properties of the polymers, different methods are used for preparation of capillary/hollow-fibre membranes. Non-solvent-induced phase separation (NIPS) method is used for PSf, PES, PVC, PVDF & PAN membranes whereas PSf & PES membranes are prepared by vapor induced phase separation (VIPS)

methods also. Thermally induced phase separation (TIPS) and melt-stretching method (MS) methods are used for PE & PP membranes.

Conflict of interest

The authors declare no conflict of interest.

References

1. Ahmed I, Yusof ZAM, Beg M. Fabrication of polymer-based mix matrix membrane—A short review. *International Journal of Basic & Applied Sciences* 2010; 10(2): 17–27.
2. Prabhakar S, Ghosh AK, Bindal RC, Tewari PK. Outside skin tubular ultrafiltration membranes for separation of proteins and polysaccharides and removal of turbidity from seawater. *Desalination and Water Treatment* 2011; 27(1–3): 231–236. doi: 10.5004/dwt.2011.2578
3. Mulder M. *Basic Principles of Membrane Technology*, 2nd ed. Springer; 1996.
4. Anokhina T, Raeva A, Makaev S, et al. Express method of preparation of hollow fiber membrane samples for spinning solution optimization: Polysulfone as example. *Membranes* 2021; 11(6): 396. doi: 10.3390/membranes11060396
5. Plisko TV, Bildyukevich AV, Zhao L, et al. Formation of polysulfone hollow fiber membranes using the systems with lower critical solution temperature. *Fibers* 2021; 9(5): 28. doi: 10.3390/fib9050028
6. Alsalhy QF, Salih AH, Simone S, et al. Poly(ether sulfone) (PES) hollow-fiber membranes prepared from various spinning parameters. *Desalination* 2014; 345: 21–35. doi: 10.1016/j.desal.2014.04.029
7. Uebele S, Johann KS, Goetz T, et al. Poly(ether sulfone) hollow fiber membranes prepared via nonsolvent-induced phase separation using the green solvent Agnique® AMD 3 L. *Journal of Applied Polymer Science* 2021; 138(37): e50935. doi: 10.1002/app.50935
8. Matsuyama H, Hayashi K, Maki T, et al. Effect of polymer density on polyethylene hollow fiber membrane formation via thermally induced phase separation. *Journal of Applied Polymer Science* 2004; 93(1): 471–474. doi: 10.1002/app.20461
9. Kim J, Kim SS, Park M, Jang M. Effects of precursor properties on the preparation of polyethylene hollow fiber membranes by stretching. *Journal of Membrane Science* 2008; 318(1–2): 201–209. doi: 10.1016/j.memsci.2008.02.050
10. Mei S, Xiao C, Hu X. Preparation of porous PVC membrane via a phase inversion method from PVC/DMAc/water/additives. *Journal of Applied Polymer Science* 2011; 120(1): 557–562. doi: 10.1002/app.33219
11. Lu F, Liu H, Xiao C, et al. Effect of on-line stretching treatment on the structure and performance of polyvinyl chloride hollow fiber membranes. *RSC Advances* 2019; 9(12): 6699–6707. doi: 10.1039/c9ra00265k
12. Yan J, Xiao C, Ji D. Robust preparation and reinforcement mechanism study of PVDF hollow fiber membrane with homogeneous fibers. *Polymer Testing* 2022; 108: 107488. doi: 10.1016/j.polymertesting.2022.107488
13. Ji D, Gao Y, Wang W, et al. Green preparation of PVDF hollow fiber membranes with multiple pore structure via melt spinning method for oil/water separation. *Journal of Environmental Chemical Engineering* 2022; 10(5): 108337. doi: 10.1016/j.jece.2022.108337
14. Gu B, Du Q, Yang Y. Microporous hollow fiber membranes formed from blends of isotactic and atactic polypropylene. *Journal of Membrane Science* 2000; 164(1–2): 59–65. doi: 10.1016/S0376-7388(99)00204-5
15. Qiu Z, He C. Polypropylene hollow-fiber membrane made using the dissolution-induced pores method. *Membranes* 2022; 12(4): 384. doi: 10.3390/membranes12040384
16. Nouri M, Abbasi M, Aghebati T, Shirzadkhan M. Preparation and characterization of nanoclay loaded polyacrylonitrile hollow fiber membranes. *The Journal of the Textile Institute* 2022; 113(5): 952—960. doi: 10.1080/00405000.2021.1909862
17. Hill R, Walker EE. Polymer constitution and fiber properties. *Journal of Polymer Science* 1948; 3(5): 609–630. doi: 10.1002/pol.1948.120030501
18. Rein H. Fibres from synthetic polymers, herausgeg. von R. Hill. Elsevier Publishing Comp. Amsterdam, 1953, 1. Aufl. XV, 554 S., 179 Abb. gebd. sh. 80. *Angewandte Chemie* 1954; 66(4): 120. doi: 10.1002/ange.19540660415
19. Sinha R. *Outlines of Polymer Technology: Manufacture of Polymers*. PHI Learning Private Limited; 2004.
20. Perepechkin LP. Methods for obtaining polymeric membranes. *Russian Chemical Reviews* 1988; 57(6): 539. doi: 10.1070/RC1988v057n06ABEH003370

21. Grosberg AY, Khokhlow AR, de Gennes PG. *Giant Molecules: Here, There, and Everywhere*, 2nd ed. World Scientific Publishing; 2010.
22. Mark JE. *Polymer Data Handbook*, 2nd ed. Oxford University; 1999.
23. Voicu ŞI, Aldea F, Radut M, Nechifor G. Nanostructured polysulfone composite membranes. *UPB Scientific Bulletin, Series B: Chemistry and Materials Science* 2008; 70(3): 39–46.
24. Kheirieh S, Asghari M, Afsari M. Application and modification of polysulfone membranes. *Reviews in Chemical Engineering* 2017; 34(5): 657–693. doi: 10.1515/revce-2017-0011
25. Scott K. *Handbook of Industrial Membranes*, 2nd ed. Elsevier Science; 1995.
26. Sherazi TA, Sohn JY, Lee YM, Guiver MD. Polyethylene-based radiation grafted anion-exchange membranes for alkaline fuel cells. *Journal of Membrane Science* 2013; 441: 148–157. doi: 10.1016/j.memsci.2013.03.053
27. Zuo J, Bonyadi S, Chung TS. Exploring the potential of commercial polyethylene membranes for desalination by membrane distillation. *Journal of Membrane Science* 2016; 497: 239–247. doi: 10.1016/j.memsci.2015.09.038
28. Behboudi A, Ghiasi S, Mohammadi T, Ulbricht M. Preparation and characterization of asymmetric hollow fiber polyvinyl chloride (PVC) membrane for forward osmosis application. *Separation and Purification Technology* 2021; 270: 118801. doi: 10.1016/j.seppur.2021.118801
29. Bhran A, Shoaib A, Elsadeq D, et al. Preparation of PVC/PVP composite polymer membranes via phase inversion process for water treatment purposes. *Chinese Journal of Chemical Engineering* 2018; 26(4): 715–722. doi: 10.1016/j.cjche.2017.09.003
30. Ghosh AK, Mamtani VS, Adak AK. Carbon based nanofillers embedded fouling resistant polyvinyl chloride nanocomposite membranes for oil-water separation. *International Journal of Scientific Research in Science, Engineering and Technology* 2023; 10(3): 394–398.
31. Ji D, Gao Y, Wang W, et al. Green preparation of PVDF hollow fiber membranes with multiple pore structure via melt spinning method for oil/water separation. *Journal of Environmental Chemical Engineering* 2022; 10(5): 108337. doi: 10.1016/j.jece.2022.108337
32. Maiboroda AB, Petrov DV, Kichik VA, Starikov EN. Polyvinylidene fluoride hollow fiber membrane and its use for treatment of natural water. *Petroleum Chemistry* 2014; 54(7): 562–567. doi: 10.1134/S0965544114070081
33. Li Y, Nulens I, Verbeke R, et al. Tuning the porosity of asymmetric membranes via simple post-synthesis solvent-treatment for non-aqueous applications. *Separation and Purification Technology* 2019; 217: 147–153. doi: 10.1016/j.seppur.2019.02.012
34. Shao H, Wei F, Wu B, et al. Effects of annealing stress field on the structure and properties of polypropylene hollow fiber membranes made by stretching. *RSC Advances* 2016; 6(6): 4271–4279. doi: 10.1039/C5RA21785G
35. Yan SY, Wang YJ, Mao H, Zhao ZP. Fabrication of PP hollow fiber membrane via TIPS using environmentally friendly diluents and its CO_2 degassing performance. *RSC Advances* 2019; 9(33): 19164–19170. doi: 10.1039/C9RA02766A
36. Guo X, Li Y, Liu Z, Xiao C. A new superhydrophobic polypropylene hollow fiber membrane preparation method and its application in the treatment of brine with high salt concentration. *Journal of Environmental Chemical Engineering* 2023; 11(1): 109054. doi: 10.1016/j.jece.2022.109054
37. Beevers RB. The physical properties of polyacrylonitrile and its copolymers. *Journal of Polymer Science: Macromolecular Reviews* 2003; 3(1): 113–254. doi: 10.1002/pol.1968.230030103
38. Wang LY, Yu LE, Lai JY, Chung TS. Effects of Pluronic F127 on phase inversion and membrane formation of PAN hollow fibers for air filtration. *Journal of Membrane Science* 2019; 584: 137–147. doi: 10.1016/j.memsci.2019.05.001

Materials Technology Reports 2023; 1(1): 124.
Review Article

From desolvation-induced self-organization on the MALDI anchor target chip surfaces to laser-induced self-organization in MALDI techniques: Correlation-spectral analysis and complex wavelet analysis of tesiographic spots on the anchor chips

Theodor K. Orekhov*, Oleg V. Gradov

Institute of Energy Problems for Chemical Physics RAS, N. N. Semenov Federal Research Center for Chemical Physics of the Russian Academy of Sciences (FRC CP RAS), 119991 Moscow, Russia

*** Corresponding author:** Theodor K. Orekhov, theorehov@gmail.com

ARTICLE INFO

Received: 13 July 2023
Accepted: 16 August 2023
Available online: 10 November 2023

doi: 10.59400/mtr.v1i1.124

ABSTRACT: This article proposes to analyze the formation and "morphogenesis" during desolvation of drops on MALDI targets and target chips using 2D correlation spectral analysis based on the two-dimensional Fourier transform and wavelet spectroscopy methods in the real and imaginary regions. The results of the correlation-spectral and wavelet analysis are shown in the illustrations in the text of the article.

KEYWORDS: desolvation; dehydration; LDI MS; MALDI; LAMMA; anchor chips

1. Introduction

It is well known, that MALDI MS frequently used for analysis of biological complex mixtures[1–15]. The applicability of Matrix Assisted Laser Desorption/Ionization methods (MALDI) in computer-assisted identification of different biochemical constituents on ahcnor chips (also known as MALDI target plates, including barcoded machine-readable ones)[16–18] with areas on which the corresponding samples for identification are pipetted is a matter of common knowledge. Pipetting of the sample onto the target plates/anchor chips can be performed manually with a glass or plastic tip (in the latter case, the probability of contamination of the sample with organic contaminants is often significantly increased) or automatically with special devices[19–29]. Literature on MALDI sampling is extremely large[30–49].

Ideally, if the goal is not just detection but specific quantitative or semi-quantitative data collection on the content of target substances in samples, the drops should be similar in volume and microrheological properties, which is not always possible with manual dosing on the plate. Identical drops are identically desolvated and crystallized however, drops applied at intervals in time, at any time after their pipetting (see **Figure 1**) have different optical and recrystallometric, desolvated and microrheological characteristics. From the standpoint of statistical data analysis and metrology, this can result in heteroscedasticity in the sample statistics associated with the difference in the size of drops and the completeness of filling the wells on the plate (MALDI target plates/anchor chips) after manual dosing. This problem is particularly evident when the types of wells geometries differ. In essence, the products of analyte dehydration/crystallization, both colloidal and macromolecular (e.g., polypeptide) in nature, from the standpoint of nonlinear physics, are self-organization products[50–61] that are formed in

the presence of the corresponding energy conditions/gradients, including laser-induced desolvated (dehydrated) self-organization. Therefore, the form of such self-organizing structures strongly depends on the medium conditions and the experimental protocol.

For both colloidal and supramolecular structures, the statements about the dependence of the structure on the preparation conditions are true. The transition from manual dosing to automatic pipettes for applying "spots" (also known as MALDI spotter), although it leads to the improvement of the reproducibility of dosing and uniformity of the plate in volume filling, does not lead to the elimination of the physical causes of desolvated heterogeneity. Therefore, when measuring native samples by direct mass spectrometry uniformity of spots is often neglected and the performance of a specific quantitative analysis is not considered, with the only purpose to identify the presence of a particular compound/chemical agent in the analyzed sample, or chemical identification of an unidentified sample, collected directly in the natural conditions, according to its MALDI mass spectra without an extremely complicated sample preparation, associated with chemical separation of the biological sample into elementary identifiable molecular components (lipids, proteins, etc.).

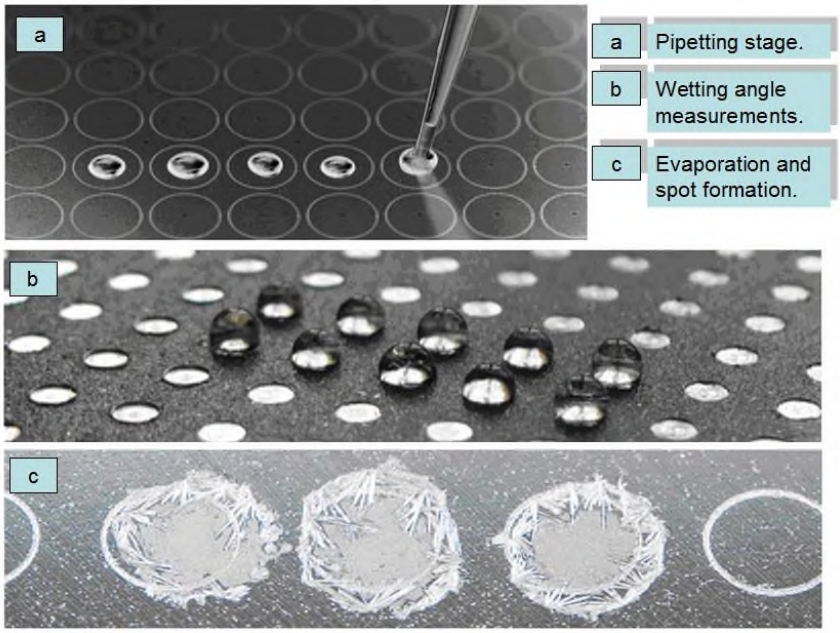

Figure 1. Stages of the liquid droplet desolvation and pattern formation in the self-organization on MALDI.

2. Methods

For a serial comparative analysis of stain dehydration patterns on MALDI chips, it was proposed to use the Fourier transform of stain images. At the same time, with the help of a neural network, each chemism of spots could be associated with a certain complex of descriptors of chemical and physical genesis. As a tool for express Fourier spectral analytics, the QAVIS software package was used, which generated IFCs and ISCs (Integral Frequency Characteristics and Integral Spatial Characteristics) based on the two-dimensional Fourier transform of the image of a spot, a drop on a chip. This complex was developed at the POI FEB RAS by the group of Fishchenko and Goncharova[62–65]. It is based on the FFTW library and was previously used for various tasks[66–72].

This technique of comparative Fourier measurements was named correlation-spectral analysis by the authors of the software package themselves.

Wavelet analysis was performed using the QAVIS program in real and imaginary coordinates.

3. Results

The results of the correlation-spectral Fourier analysis of various forms of desolvation in drops are shown in **Figures 2**–**4**. The results of wavelet correlation-spectral analysis of different forms of desolvation in drops (with separate analysis in three image fragments—on three scan strips of a photo of a drop) are shown in **Figures 5**–**7**. It can be seen that both the Fourier method and the wavelet method can distinguish between different forms of desolvation and shaping/crystallization/reaction-diffusion mophogenesis during the transition to the solid phase. This is characteristic, since when pipetting onto MALDI substrates, one can observe heteroscedasticity of samples of morphometric characteristics of droplets and patterns of their dehydration or desolvation (see **Figure 8**).

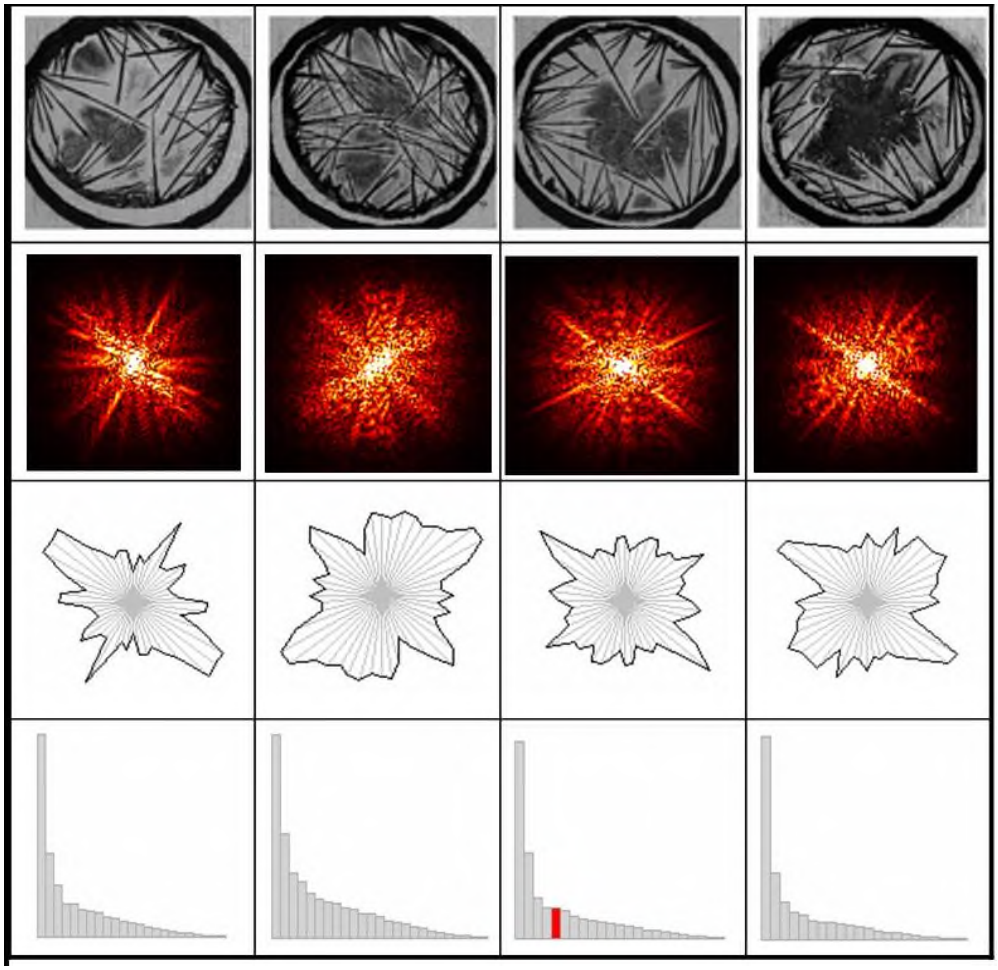

Figure 2. Comparative 2D FFT correlation-spectral analysis of droplets; example of image processing from the old presentation in Moscow State University.

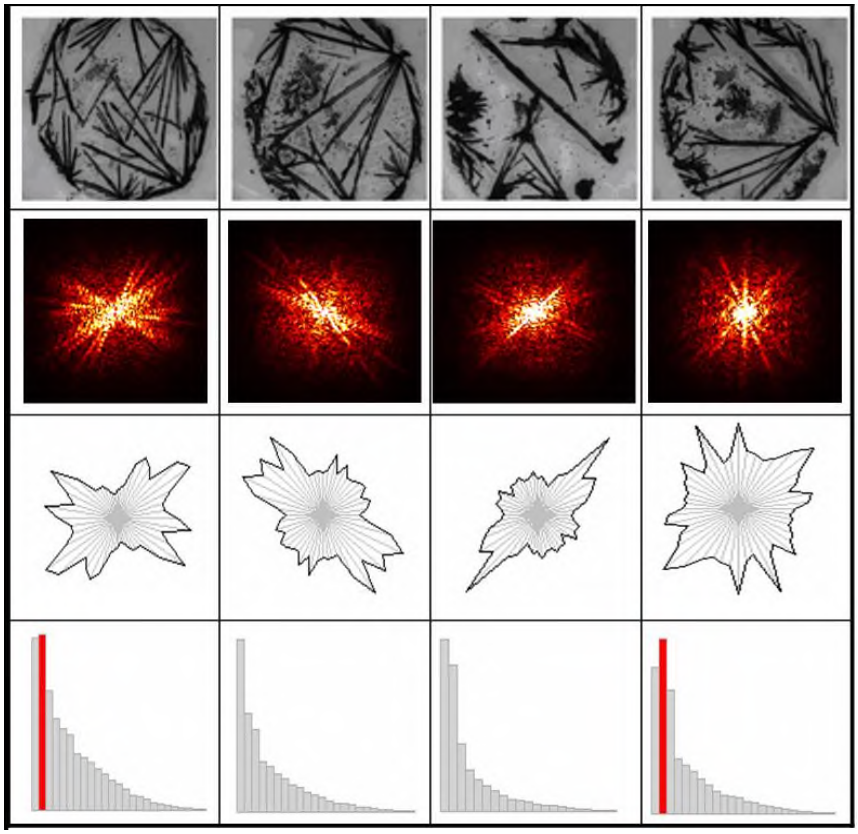

Figure 3. Comparative 2D FFT correlation-spectral analysis of droplets; example of image processing from the old presentation in Moscow State University.

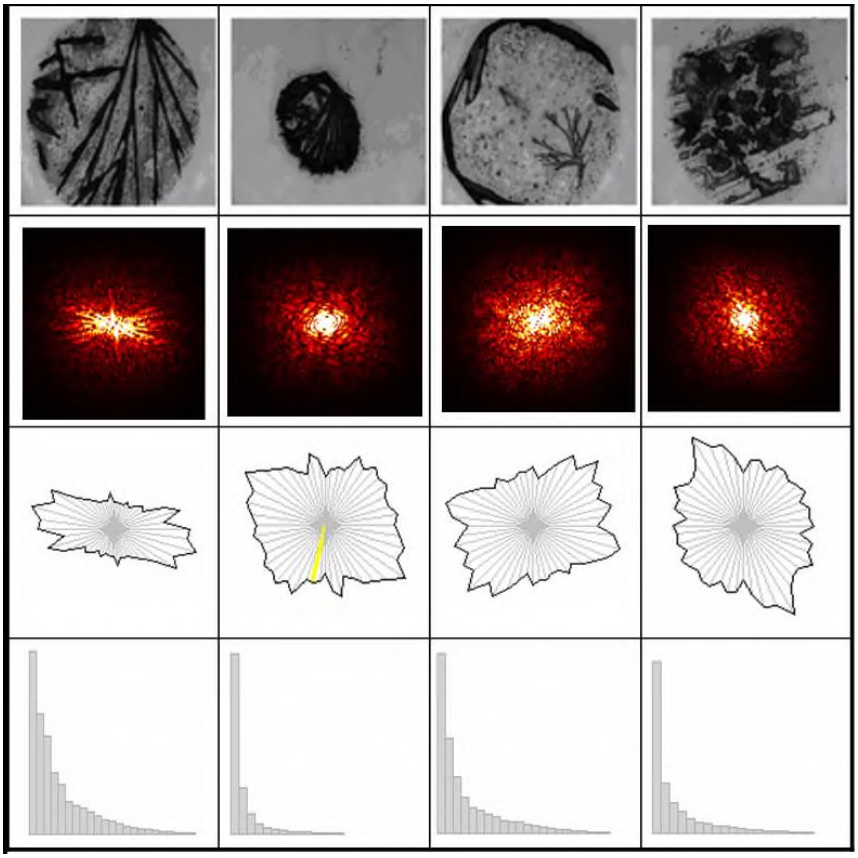

Figure 4. Comparative 2D FFT correlation-spectral analysis of droplets; example of image processing from the old presentation in Moscow State University.

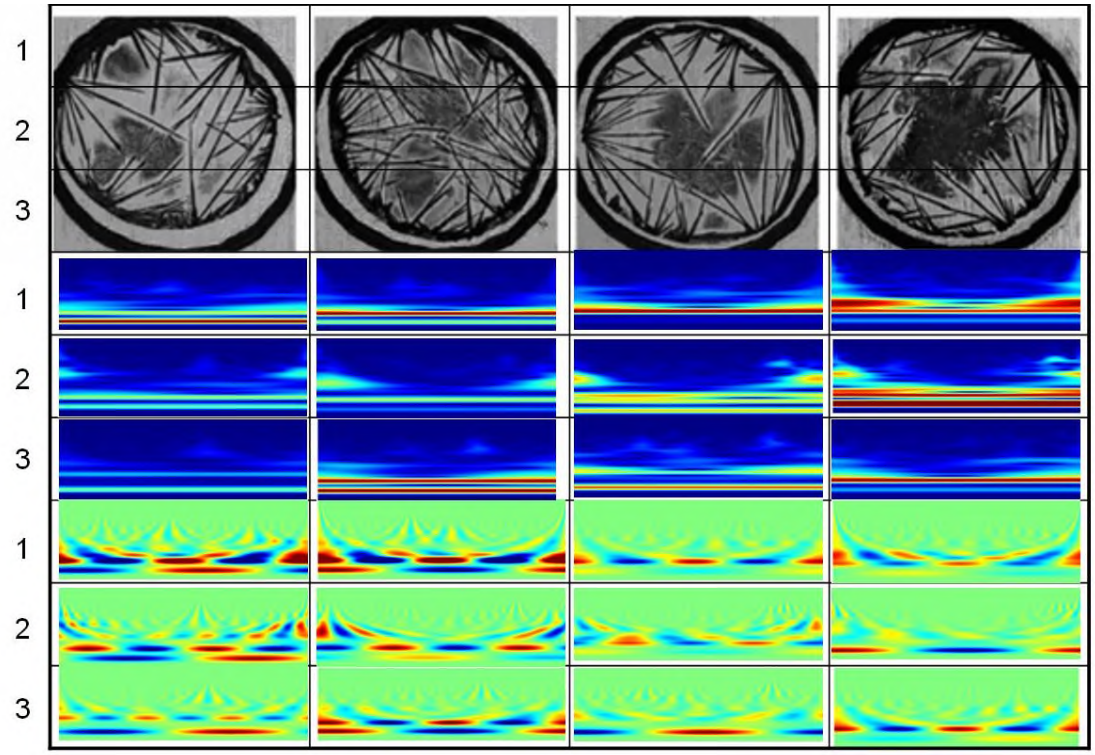

Figure 5. Comparative wavelet correlation-spectral analysis of droplet images; example of image processing from the old presentation in Moscow State University.

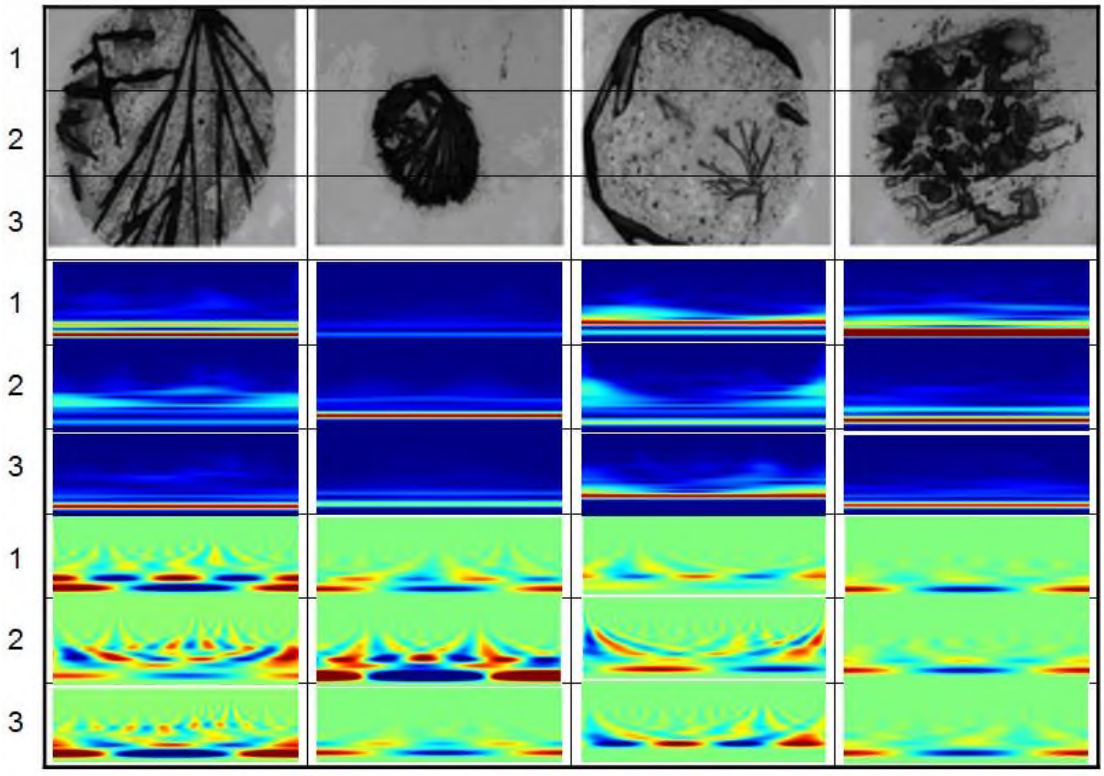

Figure 6. Comparative wavelet correlation-spectral analysis of droplet (Ibid.).

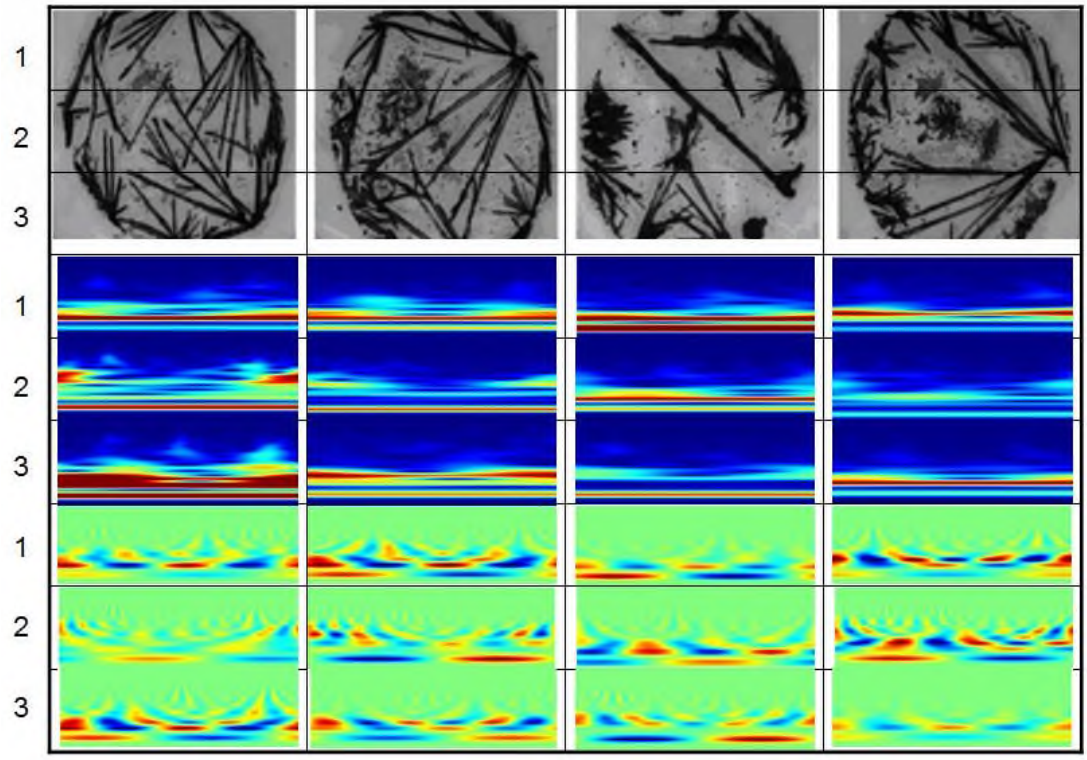

Figure 7. Comparative wavelet correlation-spectral analysis of droplet; example of image processing from the old presentation in Moscow State University.

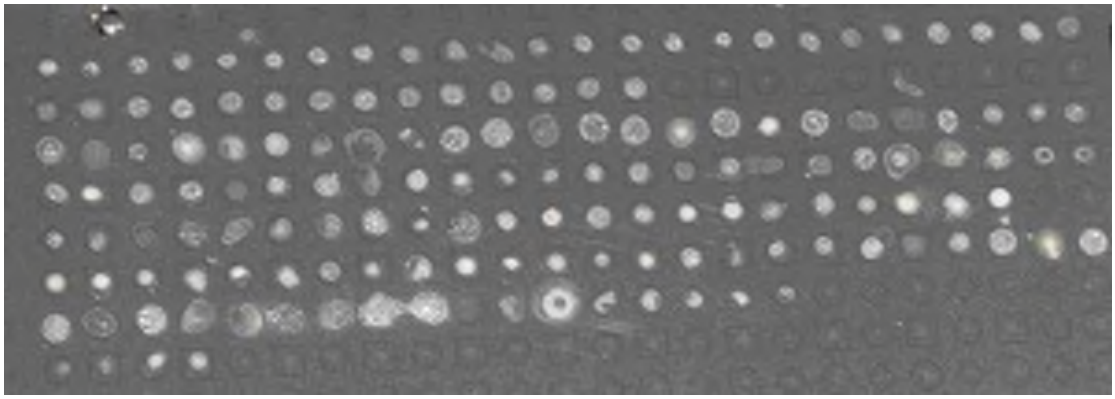

Figure 8. Comparative 2D FFT correlation-spectral analysis of droplets; example of image processing from the old presentation in Moscow State University.

4. Conclusion

So, as a result of testing the methods of Fourier analysis and wavelet analysis of cracking of drops during drying or laser drying on MALDI chips, it was shown that such methods give very well distinguishable pictures of qualitative differences between drops. This allows us to speak about the applicability of this method as a method of qualimetry in analytical chemistry and thesiography of biological fluids with MALDI analysis.

Conflict of interest

The authors declare no conflict of interest.

References

1. Ropartz D, Lemoine J, Giuliani A, et al. Deciphering the structure of isomeric oligosaccharides in a complex mixture by tandem mass spectrometry: Photon activation with vacuum ultra-violet brings unique information and enables definitive structure assignment. *Analytica Chimica Acta* 2014; 807: 84–95. doi: 10.1016/j.aca.2013.11.018
2. Sleat DE, Lackland H, Wang Y, et al. The human brain mannose 6-phosphate glycoproteome: A complex mixture composed of multiple isoforms of many soluble lysosomal proteins. *Proteomics* 2005; 5(6): 1520–1532. doi: 10.1002/pmic.200401054
3. Börnsen KO. Influence of salts, buffers, detergents, solvents, and matrices on MALDI-MS protein analysis in complex mixtures. *Methods in Molecular Biology* 2000; 146: 387–404. doi: 10.1385/1-59259-045-4:387
4. Shalayel I, Leqraa N, Blandin V, Vallée Y. Straightforward creation of possibly prebiotic complex mixtures of Thiol-Rich peptides. *Life (Basel)* 2023; 13(4): 983. doi: 10.3390/life13040983
5. Haebel S, Bahrke S, Peter MG. Quantitative sequencing of complex mixtures of heterochitooligosaccharides by vMALDI-linear ion trap mass spectrometry. *Analytical Chemistry* 2007; 79(15): 5557–5566. doi: 10.1021/ac062254u
6. Salwiński A, Da Silva D, Delépée R, Maunit B. Enzyme-coupled nanoparticles-assisted laser desorption ionization mass spectrometry for searching for low-mass inhibitors of enzymes in complex mixtures. *Journal of the American Society for Mass Spectrometry* 2014; 25(4): 538–547. doi: 10.1007/s13361-014-0826-y
7. Meng F, Cargile BJ, Patrie SM, et al. Processing complex mixtures of intact proteins for direct analysis by mass spectrometry. *Analytical Chemistry* 2002; 74(13): 2923–2929. doi: 10.1021/ac020049i
8. Quinton L, Demeure K, Dobson R, et al. New method for characterizing highly disulfide-bridged peptides in complex mixtures: Application to toxin identification from crude venoms. *Journal of Proteome Research* 2007; 6(8): 3216–3223. doi: 10.1021/pr070142t
9. Fernández-de-Cossio J, Gonzalez LJ, Satomi Y, et al. Automated interpretation of mass spectra of complex mixtures by matching of isotope peak distributions. *Rapid Communications in Mass Spectrometr: RCM* 2004; 18(20): 2465–2472. doi: 10.1002/rcm.1647
10. Schmitt-Kopplin P, Englmann M, Rossello-Mora R, et al. Combining chip-ESI with APLI (cESILI) as a multimode source for analysis of complex mixtures with ultrahigh-resolution mass spectrometry. *Analytical and Bioanalytical Chemistry* 2008; 391(8): 2803–2809. doi: 10.1007/s00216-008-2211-9
11. Perkins JR, Smith B, Gallagher RT, et al. Application of electrospray mass spectrometry and matrix-assisted laser desorption ionization time-of-flight mass spectrometry for molecular weight assignment of peptides in complex mixtures. *Journal of the American Society for Mass Spectrometry* 1993; 4(8): 670–684. doi: 10.1016/1044-0305(93)85032-S
12. Vallone PM, Devaney JM, Marino MA, Butler JM. A strategy for examining complex mixtures of deoxyoligonucleotides using ion-pair-reverse-phase high-performance liquid chromatography, matrix-assisted laser desorption ionization time-of-flight mass spectrometry, and informatics. *Analytical Biochemistry* 2002; 304(2): 257–265. doi: 10.1006/abio.2002.5641
13. Tolmachev AV, Monroe ME, Jaitly N, et al. Mass measurement accuracy in analyses of highly complex mixtures based upon multidimensional recalibration. *Analytical Chemistry* 2006; 78(24): 8374–8385. doi: 10.1021/ac0606251
14. Whitin JC, Rangan S, Cohen HJ. Identifying technical aliases in SELDI mass spectra of complex mixtures of proteins. *BMC Research Notes* 2013; 6: 358. doi: 10.1186/1756-0500-6-358
15. Beaufour M, Ginguené D, Le Meur R, et al. Liquid native MALDI mass spectrometry for the detection of protein-protein complexes. *Journal of the American Society for Mass Spectrometry* 2018; 29(10): 1981–1994. doi: 10.1007/s13361-018-2015-x
16. Sjödahl J, Kempka M, Hermansson K, et al. Chip with twin anchors for reduced ion suppression and improved mass accuracy in MALDI-TOF mass spectrometry. *Analytical Chemistry* 2005; 77(3): 827–832. doi: 10.1021/ac0400966
17. Grasso G, Fragai M, Rizzarelli E, et al. In situ AP/MALDI-MS characterization of anchored matrix metalloproteinases. *Journal of Mass Spectrometry: JMS* 2006; 41(12): 1561–1569. doi: 10.1002/jms.1126
18. Krásný L, Pompach P, Strohalm M, et al. In-situ enrichment of phosphopeptides on MALDI plates modified by ambient ion landing. *Journal of Mass Spectrometry: JMS* 2012; 47(10): 1294–1302. doi: 10.1002/jms.3081
19. Molin L, Cristoni S, Crotti S, et al. Sieve-based device for MALDI sample preparation. I. Influence of sample deposition conditions in oligonucleotide analysis to achieve significant increases in both sensitivity and resolution. *Journal of Mass Spectrometry: JMS* 2008; 43(11): 1512–1520. doi: 10.1002/jms.1428
20. Cristoni S, Molin L, Crotti S, et al. Sieve-based device for MALDI sample preparation. II. Instrumental parameterization. *Journal of Mass Spectrometry: JMS* 2009; 44(11): 1579–1586. doi: 10.1002/jms.1637
21. Molin L, Cristoni S, Seraglia R, Traldi P. Sieve-based device for MALDI sample preparation. III. Its power for

quantitative measurements. *Journal of Mass Spectrometry: JMS* 2011; 46(2): 230–236. doi: 10.1002/jms.1885
22. Hoteling AJ, Erb WJ, Tyson RJ, Owens KG. Exploring the importance of the relative solubility of matrix and analyte in MALDI sample preparation using HPLC. *Analytical Chemistry* 2004; 76(17): 5157–5164. doi: 10.1021/ac049566m
23. Hanton SD, Parees DM. Extending the solvent-free MALDI sample preparation method. *Journal of the American Society for Mass Spectrometry* 2005; 16(1): 90–93. doi: 10.1016/j.jasms.2004.09.019
24. Cho Y, Kim E, Han SK, et al. Rapid identification of vibrio species isolated from the southern coastal regions of Korea by MALDI-TOF mass spectrometry and comparison of MALDI sample preparation methods. *Journal of Microbiology and Biotechnology* 2017; 27(9): 1593–1601. doi: 10.4014/jmb.1704.04056
25. Skelton R, Dubois F, Zenobi R. A MALDI sample preparation method suitable for insoluble polymers. *Analytical Chemistry* 2000; 72(7): 1707–1710. doi: 10.1021/ac991181u
26. Aerni HR, Cornett DS, Caprioli RM. Automated acoustic matrix deposition for MALDI sample preparation. *Analytical Chemistry* 2006; 78(3): 827–834. doi: 10.1021/ac051534r
27. Fenyo D, Wang Q, DeGrasse JA, et al. MALDI sample preparation: The ultra thin layer method. *Journal of Visualized Experiments: JoVE* 2007; 3(3): 192. doi: 10.3791/192
28. Andersson T, Johansson M, Bolmsjö G, James P. Automating MALDI sample plate loading. *Journal of Proteome Research* 2007; 6(2): 894–896. doi: 10.1021/pr0603607
29. Patil AA, Chiang CK, Wen CH, Peng WP. Forced dried droplet method for MALDI sample preparation. *Analytica Chimica Acta* 2018; 1031: 128–133. doi: 10.1016/j.aca.2018.05.056
30. Gholipour Y, Erra-Balsells R, Nonami H. In situ pressure probe sampling and UV-MALDI MS for profiling metabolites in living single cells. *Mass Spectrometry (Tokyo, Japan)* 2012; 1(1): A0003. doi: 10.5702/massspectrometry.A0003
31. Chen B, Vavrek M, Gundersdorf R, et al. Combining MALDI mass spectrometry imaging and droplet-base surface sampling analysis for tissue distribution, metabolite profiling, and relative quantification of cyclic peptide melanotan II. *Analytica Chimica Acta* 2020; 1125: 279–287. doi: 10.1016/j.aca.2020.05.050
32. Wong KFC, Greatorex RE, Gidman CE, et al. Surface-sampling mass spectrometry to study proteins and protein complexes. *Essays in Biochemistry* 2023; 67(2): 229–241. doi: 10.1042/EBC20220191
33. Wang Y, Schneider BB, Covey TR, Pawliszyn J. High-performance SPME/AP MALDI system for high-throughput sampling and determination of peptides. *Analytical Chemistry* 2005; 77(24): 8095–8101. doi: 10.1021/ac051222o
34. Fu Q, Tang J, Cui M, et al. Application of porous metal enrichment probe sampling to single cell analysis using matrix-assisted laser desorption ionization time of flight mass spectrometry (MALDI-TOF-MS). *Journal of Mass Spectrometry: JMS* 2016; 51(1): 62–68. doi: 10.1002/jms.3729
35. Haidas D, Napiorkowska M, Schmitt S, Dittrich PS. Parallel sampling of nanoliter droplet arrays for noninvasive protein analysis in discrete yeast cultivations by MALDI-MS. *Analytical Chemistry* 2020; 92(5): 3810–3818. doi: 10.1021/acs.analchem.9b05235
36. Taguchi Y, Ishida Y, Ohtani H, Matsubara H. Direct analysis of an oligomeric hindered amine light stabilizer in polypropylene materials by MALDI-MS using a solid sampling technique to study its photostabilizing action. *Analytical Chemistry* 2004; 76(3): 697–703. doi: 10.1021/ac030270a
37. Shiau KJ, Hung SU, Lee HW, Wu CC. Nanodiamond-based two-step sampling of multiply and singly phosphorylated peptides for MALDI-TOF mass spectrometry analysis. *The Analyst* 2011; 136(9): 1922–1927. doi: 10.1039/c0an01046d
38. Mess A, Enthaler B, Fischer M, et al. A novel sampling method for identification of endogenous skin surface compounds by use of DART-MS and MALDI-MS. *Talanta* 2013; 103: 398–402. doi: 10.1016/j.talanta.2012.10.073
39. Pereira I, Banstola B, Wang K, et al. Matrix-assisted laser desorption ionization imaging and laser ablation sampling for analysis of fungicide distribution in apples. *Analytical Chemistry* 2019; 91(9): 6051–6056. doi: 10.1021/acs.analchem.9b00566
40. Lawal RO, Richardson LT, Dong C, et al. Deep-ultraviolet laser ablation sampling for proteomic analysis of tissue. *Analytica Chimica Acta* 2021; 1184: 339021. doi: 10.1016/j.aca.2021.339021
41. Chen C, Huang Y, Wu P, et al. In vivo microcapillary sampling coupled with matrix-assisted laser desorption/ionization fourier transform ion cyclotron resonance mass spectrometry for real-time monitoring of paraquat and diquat in living vegetables. *Food Chemistry* 2022; 388: 132998. doi: 10.1016/j.foodchem.2022.132998
42. Sun S, Tang W, Li B. Authentication of single herbal powders enabled by microscopy-guided in situ auto-sampling combined with matrix-assisted laser desorption/ionization mass spectrometry. *Analytical Chemistry* 2023; 95(19): 7512–7518. doi: 10.1021/acs.analchem.2c05517
43. Chen X, Gao J, Wang T, et al. Hepatocarcinoma discrimination by ratiometric lipid profiles using tip-contact sampling/ionization mass spectrometry. *Analytical Chemistry* 2019; 91(16): 10376–10380. doi:

10.1021/acs.analchem.9b02623
44. Donnarumma F, Camp EE, Cao F, Murray KK. Infrared laser ablation with vacuum capture for fingermark sampling. *Journal of the American Society for Mass Spectrometry* 2017; 28(9): 1958–1964. doi: 10.1007/s13361-017-1703-2
45. Zhang H, Zhang C, Lajoie GA, Yeung KK. Selective sampling of phosphopeptides for detection by MALDI mass spectrometry. *Analytical Chemistry* 2005; 77(18): 6078–6084. doi: 10.1021/ac050565j
46. Ishida Y, Kitagawa K, Goto K, Ohtani H. Solid sampling technique for direct detection of condensed tannins in bark by matrix-assisted laser desorption/ionization mass spectrometry. *Rapid Communications in Mass Spectrometry: RCM* 2005; 19(5): 706–710. doi: 10.1002/rcm.1845
47. Pelzer AE, Feuerstein I, Fuchsberger C, et al. Influence of blood sampling on protein profiling and pattern analysis using matrix-assisted laser desorption/ionisation mass spectrometry. *BJU International* 2007; 99(3): 658–662. doi: 10.1111/j.1464-410X.2006.06678.x
48. Xiang P, Lin P. Solid sampling technique for direct detection of condensed tannins in bark by matrix-assisted laser desorption/ionization mass spectrometry. *Rapid Communications in Mass Spectrometry* 2006; 20(3): 521. doi: 10.1002/rcm.2291
49. Taguchi Y, Ishida Y, Matsubara H, Ohtani H. Quantitative analysis of an oligomeric hindered amine light stabilizer in polypropylene by matrix-assisted laser desorption/ionization mass spectrometry using a solid sampling technique. *Rapid Communications in Mass Spectrometry* 2006; 20(8): 1345–1350. doi: 10.1002/rcm.2452
50. Rapis EG, Gasanova G. Autowave process in the dynamics of phase transition in a protein film. *Technical Physics* 1991; 36(4): 406–412.
51. Rapis EG. The self-organization of protein. *Technical Physics Letters* 1995; 21(5): 321-324.
52. Rapis EG. Self-assembly of cluster protein films (allotropic nonequilibrium noncrystalline modification) during the process or their condensation. *Technical Physics* 2000; 45(1): 121–131. doi: 10.1134/1.1259582
53. Rapis E. Properties and symmetry of the solid cluster phase of protein. *Technical Physics* 2001; 46: 1307–1313. doi: 10.1134/1.1412069
54. Rapis E. A change in the physical state of a nonequilibrium blood plasma protein film in patients with carcinoma. *Technical Physics* 2002; 47: 510–512. doi: 10.1134/1.1470608
55. Golbraikh E, Rapis EG, Moiseev SS. On the crack pattern formation in a freely drying protein film. *Technical Physics* 2003; 48: 1333–1337. doi: 10.1134/1.1620131
56. Rapis E. Self-organization and supramolecular chemistry of protein films from the nano-to the macroscale. *Technical Physics* 2004; 49: 494–498. doi: 10.1134/1.1736921
57. Rapis E. On the problem of nucleation (cell formation) in self-organization of protein nanostructures in vitro and in vivo. *Technical Physics* 2005; 50: 780–786. doi: 10.1134/1.1947357
58. Rapis E. Relaxation of the energy of the protein colloidal solution arising at drying in open and closed systems. *Technical Physics* 2005; 50: 1236–1238. doi: 10.1134/1.2051470
59. Rapis E. Nonequilibrium state of self-organized protein nanostructures. *Technical Physics* 2006; 51: 268–273. doi: 10.1134/S1063784206020198
60. Rapis E. On the nonequilibrium phase transition in protein. *Technical Physics* 2007; 52: 787–792. doi: 10.1134/S1063784207060199
61. Rapis E. Evolutionary aspect of protein self-organization. *Technical Physics* 2008; 53: 783–788. doi: 10.1134/S1063784208060182
62. Fishchenko VK, Goncharova AA, Dolgikh GI, et al. Express image and video analysis technology QAVIS: Application in system for video monitoring of Peter the Great Bay (Sea of Japan/East Sea). *Journal of Marine Science and Engineering* 2021; 9(10): 1073. doi: 10.3390/jmse9101073
63. Fischenko V, Mitnik L, Dolgikh G, et al. QAVIS technology: Measuring wave processes in coastal zones based on the analysis of internet video broadcast. In: Proceedings of the IGARSS 2022-2022 IEEE International Geoscience and Remote Sensing Symposium; 17–22 July 2022; Kuala Lumpur, Malaysia. pp. 6801–6804.
64. Goncharova AA, Fischenko VK, Dubina VA. Use the express-analysis program QAVIS for the satellite monitoring. *Current Problems in Remote Sensing of the Earth from Space* 2012; 9(3): 293–298.
65. Goncharova AA, Fischenko VK. QAVIS—Program for quick image and video analysis. In: Proceedings of 8th Open German-Russian Workshop on Pattern Recognition and Image Understanding (OGRW-8 2011). p. 85.
66. Fishchenko VK, Dolgikh GI, Zimin PS, Subote AE. Some results of oceanological video monitoring. *Doklady Earth Sciences* 2018; 482: 1244–1247. doi: 10.1134/S1028334X18090283
67. Dolgikh GI, Fishchenko VK, Goncharova AA. Potential for recording of waves and sea level fluctuations in the world ocean coastal areas by internet video analysis. *Doklady Earth Sciences* 2019; 488: 1264–1267. doi: 10.1134/S1028334X19100209
68. Dolgikh GI, Fishchenko VK, Goncharova AA. About the possibility of registration of waves and sea level fluctuations in coastal areas of the World Ocean based on analysis of video on the Internet. *Doklady Earth*

Sciences 2019; 488(6): 667–672. doi: 10.31857/S0869-56524886667-672
69. Gradov OV, Aleksandrov PL, Gradova MA. Study of mineral samples relevant for desert locations using software correlation spectral analysis of scanning electron microscopy registers: From 2D Fourier spectra to online analysis of statistics of integral spatial characteristics. *Software Systems and Computational Methods* 2019; 4: 125–171. doi: 10.7256/2454-0714.2019.4.31379
70. Gradov OV, Gradova MA, Maklakova IA, Kholuiskaya SN. Towards electron-beam-driven soft/polymer fiber microrobotics for vacuum conditions. *Materials Research Proceedings* 2022; 21: 370–383. doi: 10.21741/9781644901755-64
71. Skrynnik AA, Oganessian VA, Jablokov AG, Gradov OV. System for semiautomatic tissue classification based on optical diffractometer for biopolymer structure analysis. *Morphologia* 2018; 12(3): 164–171. doi: 10.26641/1997-9665.2018.3.164-171
72. Adamovich E, Buryanskaya E, Elfimov A, et al. Towards Femtoscan-assisted analysis of liquid crystal self-organization on different polymer and glass surfaces for lab-on-a-chip and lab-on-a-dish applications, including optofluidic and flexoelectric ones. *Recent Progress in Materials* 2023; 5: 1–20.

Materials Technology Reports 2023; 1(1): 135.
Review Article

Reaction-diffusion effects and spatiotemporal oscillations under SEM, STM and AFM-assisted charging in fiber-like and wire-like systems: From molecular and quantum wires to cooperative ferroelectric nanofibers and microfibers

Eugene D. Adamovich, Eugenia L. Buryanskaya, Margaret A. Gradova, Oleg V. Gradov*

CHEMBIO Department, Semenov Federal Research Center for Chemical Physics of the Russian Academy of Sciences (FRC CP RAS), 119991 Moscow, Russian Federation

*** Corresponding author:** Oleg V. Gradov, o.v.gradov@gmail.com

ARTICLE INFO

Received: 20 July 2023
Accepted: 3 August 2023
Available online: 27 November 2023

doi: 10.59400/mtr.v1i1.135

ABSTRACT: This review addresses the problem of reaction-diffusion effects and spatiotemporal oscillations in fiber-like and wire-like systems under the electron beam in SEM and in the presence of electric field in some special AFM techniques, such as current sensing atomic force microscopy (CS-AFM)/conductive atomic force microscopy (C-AFM), electrostatic force microscopy (EFM) and Kelvin probe force microscopy (KPFM) also known as surface potential microscopy. Some similar reaction-diffusion effects also can be observed in scanning capacitance microscopy (SCM), scanning gate microscopy (SGM), scanning voltage microscopy (SVM) and piezoresponse force microscopy (PFM). At the end of this paper the authors provide analysis of their own results and approaches. In particular, the possibility of achieving the ion transfer controlled growth of cells along the ion concentration gradients in reaction-diffusion fibers and actuators is indicated. This fundamental idea is discussed within the framework of the implantable fiber "bioiontronics" and "neuroiontronics" controlled by acoustic and electrical signals that regulate the reaction-diffusion or chemical oscillation activity of such fiber structures as reaction-diffusion actuators and sensors. The literature review includes more than 130 references.

KEYWORDS: dielectric charging; reaction-diffusion; iontronics; nanofibers and microfibers

1. Introduction

Effects of incremental charging of molecules and supramolecular structures under the tip of the scanning tunnelling microscope are well known since 1990s[1]. Such effects (taking into account Coulomb interaction of electrons) are the basis of the theory of quantum wire states[2]. Sablikov et al.[3], write that, "The chemical potential difference that exists between a decoupled, isolated quantum wire and the reservoirs gives rise to charge transfer in the coupled system… the quantum wire can be charged positively or negatively or remain neutral as a whole, depending on such factors as the wire radius and the background charge density in the wire. The magnitude of the charge and its sign are to a large extent determined by the exchange interaction of the electrons in the wire… The period of the oscillations depends on the charge acquired by the wire and the exchange energy[3]." Consequently, the effect of incremental charging of the quantum wires in various conditions can be interpreted as the

reaction-diffusion process with many possible oscillation regimes. Despite the fact that, "The linear conductance is… a function of the chemical potential", the authors write, "The nonadiabatic transition from the reservoirs to the wire leads to conductance oscillations caused by multiple scattering of electron waves… and the exchange interaction strongly enhances the Friedel oscillations near the contacts."[3] The charging effect can be visualized not only at the repolarizable/resonant quantum wires with bistability[4] (when "the system becomes unstable with respect to fluctuations of the electric potential and the electron density"[3] and instabilities are the result of multistable electron states), but also in semiconductor quantum dot and wire arrays[5,6]. Only the background of the surface physics for low-dimensional systems (for example—1D metallic segments at the quantum wire[7] or 0D quantum dots) can be used for the description of charging and transport in the quantum or molecular wire systems, including very complex multiterminal and fractal-like branched ones[8]. Models of such phenomena must be multiphysical[9,10], because they must consider all types of interactions (including non-covalent ones) and forces at the surfaces of quantum or molecular wires, which must be spatially colocalized with conduction maps[11]. In the ideal case of a time-resolved (4D) approach in the analysis of charging of 1D systems the charge pattern must be colocalized with nanomechanics and mobility/motility of the "wires" at the time-resolved ("time-lapse") multilayer map for different forces and levels of energy/charging[12,13].

A crucial problem of the wire theory application in the past twenty years is its focusing only on the nanoscale phenomena and misuse of the terms "nano-" or "nanowire" in some situations, which blurs the meaning of the terms when they are inapplicable or beyond the technical level of the experiment. This terminological confusion blurs the distinctions between the real nanoscale wires, where quantum effects are observed, and microscale wires, where they can be neglected/ignored. However, from the precision Si nanosensors[14] and single electron charging nanowire quantum dots[15] to macroscopic lithium-ion batteries or supercapacitors[16–22] "charging nanowires" are widely used as a term. At the same time, it is quite obvious that "charging nanowires" in the case of supercapacitors and lithium-ion batteries can be replaced by "microwires" without changing the term meaning and physical sense of the effects observed[23,24]. As it is known, the influence of quantum effects and the importance of "quantization" increases inversely with the nanowire diameter for a given material. When comparing different materials, the significance of quantization depends on their electronic properties, in particular on the effective mass of electrons. This means that the significance will depend on "how the conduction electrons interact with the atoms within the analyzed material". In practice, semiconductors start to exhibit a clear effect of conductance quantization at sufficiently large transverse wire dimensions (100 nm), since their electronic levels already increase at such parameters due to the spatial restrictions. As a result, the Fermi wavelength of the electrons increases and splitting of the energy levels with sufficiently low energies occurs. This means that they can only occur at cryogenic (several K) temperatures, when the thermal excitation energy is lower than the energy of transitions between states. A quantum wire is just a conductive wire in which quantum effects influence the transport phenomena. Due to quantum restrictions on the conduction electrons in the transverse direction of wires, their transverse energy is quantized into a number of discrete values. In other cases, nanowires as well as supramolecular or molecular wires may not be considered as the quantum wires.

We proceed from the fact that it is difficult to work with single quantum wires and nanowires due to both physical and technical limitations. Therefore, we firstly do not consider oscillations and reaction-diffusion processes for nanowires, and secondly, we carry out modeling using rechargeable and repolarizable microwire-like polymer ferroelectrics. For the above reasons, we move from the methods of

tunneling microscopy to the SEM (scanning electron microscopy) methods in different specific operation modes, including YMD.

The local dielectric charging induced by the line scanning during SEM observation is a well known phenomenon, which can be simulated using simple mathematical/statistical physical approaches[25,26] (including those approved by the standards of NIST (National Institute of Standards and Technology[27])). The electric charging of electron microscopic specimens has been actively studied from 1960s or 1970s[28,29]. Initially, this effect was perceived only as an obstacle to obtaining high quality SEM images. "The elimination of charging artifacts in the scanning electron microscope" was the main aim of SEM-assisted sample charging investigations at the earliest years of SEM development[30,31]. Such artifacts can be detected not only by the SEM image drift/defocusing induced by charging during observation[32], but also by the signals of X-ray analysis[33], particularly in ESEM and variable pressure scanning electron microscopes[34]. According to Miller[33], "The effects of charging of uncoated, highly resistive samples of energy-dispersive X-ray spectra are examined. It is observed that as sample charging increases, the continuum background and characteristic peaks at higher X-ray energies diminish. Modelling of the continuum background has allowed this effect to be related to the development of a surface potential on the sample." And, "This potential reduces the effective accelerating voltage of the electrons and results in a decreased overvoltage necessary for excitation of higher-energy X-rays. This artifact may lead to erroneous results in compositional analysis based on such charging-affected spectra."

There are many methods for suppressing and elimination of the charging artifacts, such as random or pseudo-random scanning[35], vector scanning[36] and Rayleigh contrast stretching method[37]. There are also many approaches that uniquely identify and compensate the charging signal[38]. However, such methods for identifying the charging signal without its suppression and compensation also have significant methodical value, since they allow to study only the sample charging signals without taking into account another basic components of the microscopic image signals. For correct interpretation of the identified microsample charging signal it is necessary to consider its physical mechanism rather than formally filtered, eliminated (by identification and subsequent matched filtering of the signal) images/signal features spaces.

It is well known that after the first observations of the surface charging using scanning electron microscopes[39] (which can be interpreted as the starting point for the development of the stroboscopic electron microscopy at MSU by G. V. Spivak and the prerequisites for the EBIC/EMF technique development) the surface charging of different chemical compounds was proposed as a characterization method of their surfaces (since 1970s till now, from inorganic to polymeric samples[40–43]). Therefore, for spatiotemporal charging analysis not only inorganic, but also polymeric samples can be investigated. Since they are dielectrics, insulators in a primitive representation, elements of physics of the charging dielectrics under the electron beam are applicable to them in a certain approximation[44,45].

Instead of analyzing the quantized charging of the quantum wires/nanowires, we will consider the analysis of charging of fibrous polymeric ferroelectric or piezoelectric composites. They clearly demonstrate the effects of the charge wandering, polarization/repolarization, as well as electromechanical dynamics under the electron beam. Many effects characteristic for the conductor-insulator composites, semiconducting and percolating samples can be observed on the developed surface of polymeric ferroelectrics and composites based on organic ferroelectric materials (compare with the study of Campbell et al.[46] and Barkay et al.[47]). Note that charging of ferroelectrics and piezoelectrics in SEMs (for example, TGS) has been studied since 1988[48] and (corresponding to their generation modes) a metastable surface-acoustic wave contrast observed in a scanning electron

microscope has been also described in 1988[49]. Accordingly, using the analysis of histograms (and possibly their central moments) from the SEM charging images[50], one can perform mapping of the ferroelectric or piezoelectric properties of such complex polymeric samples. It can be implemented not only in the case of the negative charging, but also in the case of a positive charge[51,52], which can be colocalized not only with the electron concentrations but also with the proton concentration in polymeric ferroelectrics (such as proton conductivity of PVDF[53–62]). Of particular interest is the case of charging under the electron beam, taking into account the plasma emerging under the action of the electron beam[63]. Note that the effects observed in this case are multiphysical and are not reducible to the simpler machinery of the nanowire charging in collisionless plasma[64].

As for the study of polymer ferroelectrics for space applications[65–76], it should be noted that the processes similar to those during the polymer irradiation under an electron beam in a vacuum SEM chamber can also be observed in real outer space conditions when spacecrafts are bombarded with the particles (electrons, ions) of galactic and solar origin[77,78]. Even more interesting phenomena requiring surface charge compensation (including electromechanical ones) occur when observing dielectric samples in ESEM[79,80] and CryoEM (in particular, hydrocolloids or biological samples[81]). The mechanisms underlying such phenomena of the sample surface charging can lead to the shift in the accuracy of X-ray spectral analysis and chemical element map quality deviation in variable pressure scanning electron microscopy[82,83]. None of the methods of local ("topical") controlling over the surface charging by other chemical agents or labels can be used in the case of position sensitive chemical mapping (since it can be the source of metrological artifacts itself)[84]. Consequently, the charging effect metrology in SEM can be based not only on the physical signal changes[85], but also on the qualimetry of the shift of calibration curves or chemical distribution curves and spectra. A situation can often arise when hardware suppression of the parasitic charging signals does not lead to the improvement in chemical metrology, since there is no improvement in charging at the level of the samples and detectors that record its signals in the X-ray spectral range[86].

Both nanotechnologists and users of nanotechnology-related equipment have a question: Why SEM is the best tool to study the charging of fibers, wires, linear structures in comparison with tunneling microscopy and AFM? Indeed, some AFM methods have been used to analyze the local ("topical") charging of nanostructured samples since the 1990s, despite the fact that most of such results are classified as artifacts[87]. However, the geometric requirements for the linearity or planarity of the sample in this case are extremely important/obligate. The possibility of the single particle (or nanocrystal) studying or single molecule measurements is the "reverse side of the coin" for the impossibility of analyzing three-dimensional geometrically complex samples with a mesoscopically developed surface. It is possible to study/measure the charging of single semiconductor nanocrystals[88,89], inorganic 2D layers[90,91], self-assembled monolayers[92,93] and nanolithography-level 2D polymeric surfaces[94] (using special amplitude modulated techniques). It is possible to measure not only contact charging of bulk or 2D planar layer insulator surfaces[95], but also single particle electrostatic charging[96], single molecule charging by atomic force microscopes[97,98], including regular, periodic charging of individual molecules coupled to the motions of an atomic force microscopy tips[99]. But it is impossible to measure dynamic electromechanical coupling in 3D oscillating and strictionable piezoelectric polymer microwire systems in 3D space by AFM. In AFM one can measure only single electron charging effects for nanosystems[100–103], but can not measure synchronous cooperative electron transfer or transport of the charge gradients along the complex fiber. This is also true for quantum wires, because the simplest quantum wires can be made from metallic carbon nanotubes, which can be investigated by AFMs. It is

well known that it is possible to create macroscopic quantum wires based on carbon nanotubes, since in complex carbon nanotube filaments there is no need for each individual fiber to pass along the entire length of the wire due to the quantum tunneling of electrons, which creates tunnel transition from strand to strand. At the same time, it is obvious that AFMs cannot be used for the synchronous analysis of charging or charge transfer in such complex structures, while electron microscopy methods can be used for these purposes (since 1950s when specimen charging for latex particles was registered by TEM electron microscopes[104]). SEM techniques can be used for the analysis of charging of macroscopic complex and cooperative fibers up to the micron- and decamicron-scale radius fibers (e.g., hair[105–107]) (while AFMs can analyze the hair charging only at nanoscales, and not in a complex and mutual dependence of the charging of different hair fibers on each other[108,109]). Consequently, SEM technique is more optimal for the analysis of cooperatively driven ferroelectric fibers then AFM. It is quite obvious that oscillations observed in such systems are oscillations in distributed systems, and the corresponding models of the dynamics of reaction-diffusion processes in such systems should be interpreted as the models of 3D (4D) processes in distributed systems with spatiotemporal reactions under the electron beam, which is a control agent for the wave or pulse propagation with different charges and polarities (as Turing activators and inhibitors in the classical approaches[110–121]).

Further presentation of the experimental data obtained on bioferroelectric PHB fibers will be based on the approaches and assumptions described above.

2. Results and prospects

Figures 1 and **2** show dielectric charging of ferroelectric polymer fibers taking into account the action of the electric double layer[122,123]. The discrete and pulsating kinetics of the charge wandering along the fiber is observed, which corresponds to the reaction-diffusion model with the wandering waves. In the case of ionic or proton conductivity, rather than the conventional charge wandering, this system can be considered as a quasi-chemical ion-exchange system[124]. The effects of ionic conduction can be of great importance for biomedical iontronics and the creation of active implants, which can be stimulated and perform ion exchange with the environment during conduction of biological autowaves and chemical oscillations (for example, in cardiomyocytes and neuronal fibers)[125–128]. Moreover, despite the apparent homogeneity of the fibers, in fact they can be microheterogeneous, which corresponds to a different surface distribution of the charge/electric double layer. As a result, the charge wave propagation will be inhomogeneous even over the single fiber surface. Examples of this phenomenon from our work[129] are shown in **Figures 3–5**.

Many of these waves are associated with acoustic and mechanical vibrations of the fibers induced by the electron beam. Therefore, it is possible to develop the principles of design of the reaction-diffusion and autowave fiber systems. In such systems (potential scaffolds taking into account their biophysical biocompatibility) it is possible to achieve the ion transfer and controlled growth of cells along the ion concentration gradients during ion transfer and ion exchange (ion conductivity, including proton conductivity). In other words, not only implantable acoustofluidics based on such filamentous microfluidic structures can be implemented in the future, but also implantable "bioiontronics" and "neuroiontronics" controlled by the acoustic and electrical signals that regulate the reaction-diffusion or chemical oscillation activity of such fiber structures as reaction-diffusion actuators and sensors[130–133].

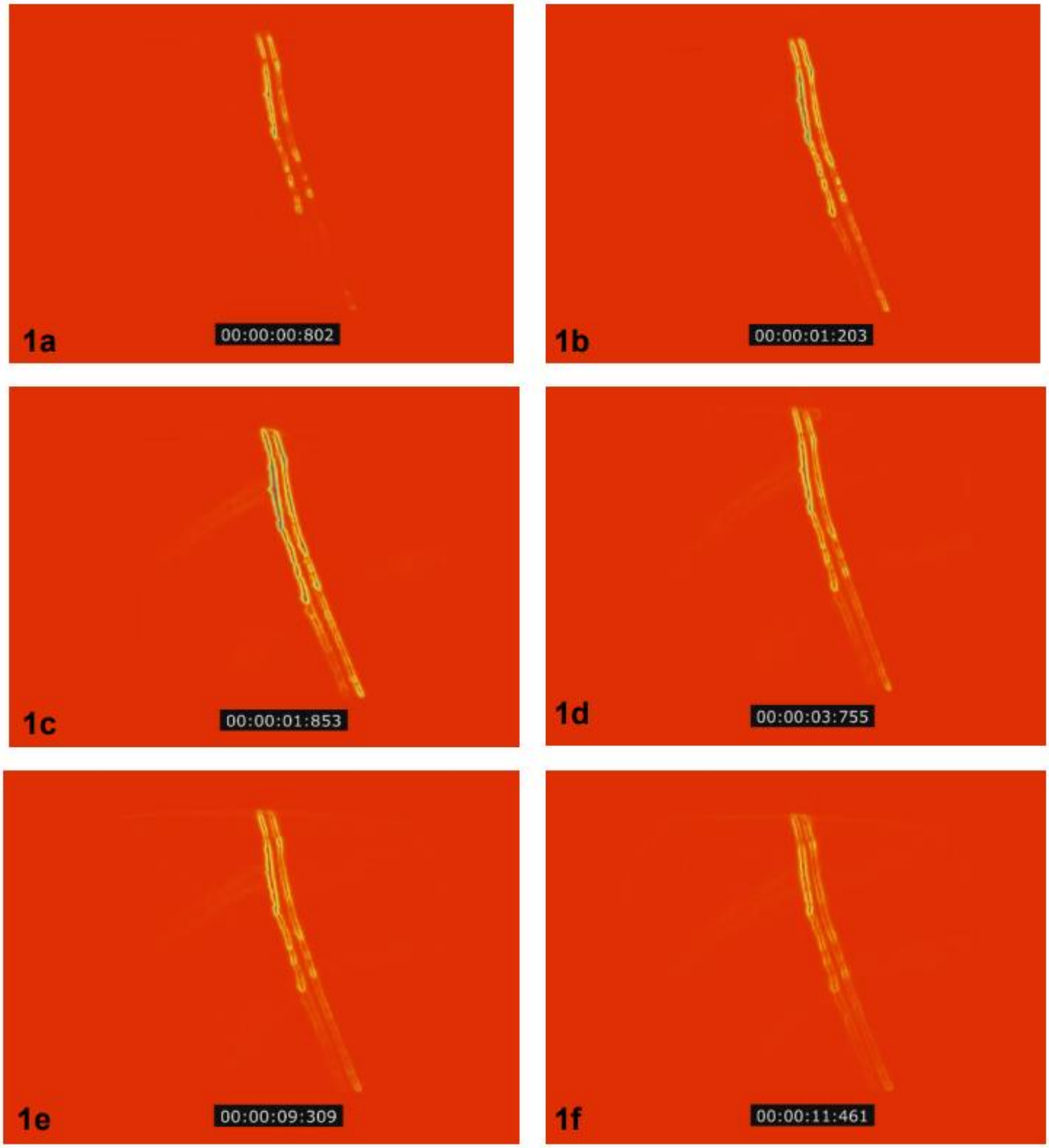

Figure 1. Dynamic images of the electric double layer charge propagation under electron beam at 500x magnification.

It can be seen that the charge isoline positions change in time and the charge propagation occurs cyclically, but not periodically, and the charge often accumulates on the heterogeneities of the fiber structure which prevent its further propagation[122].

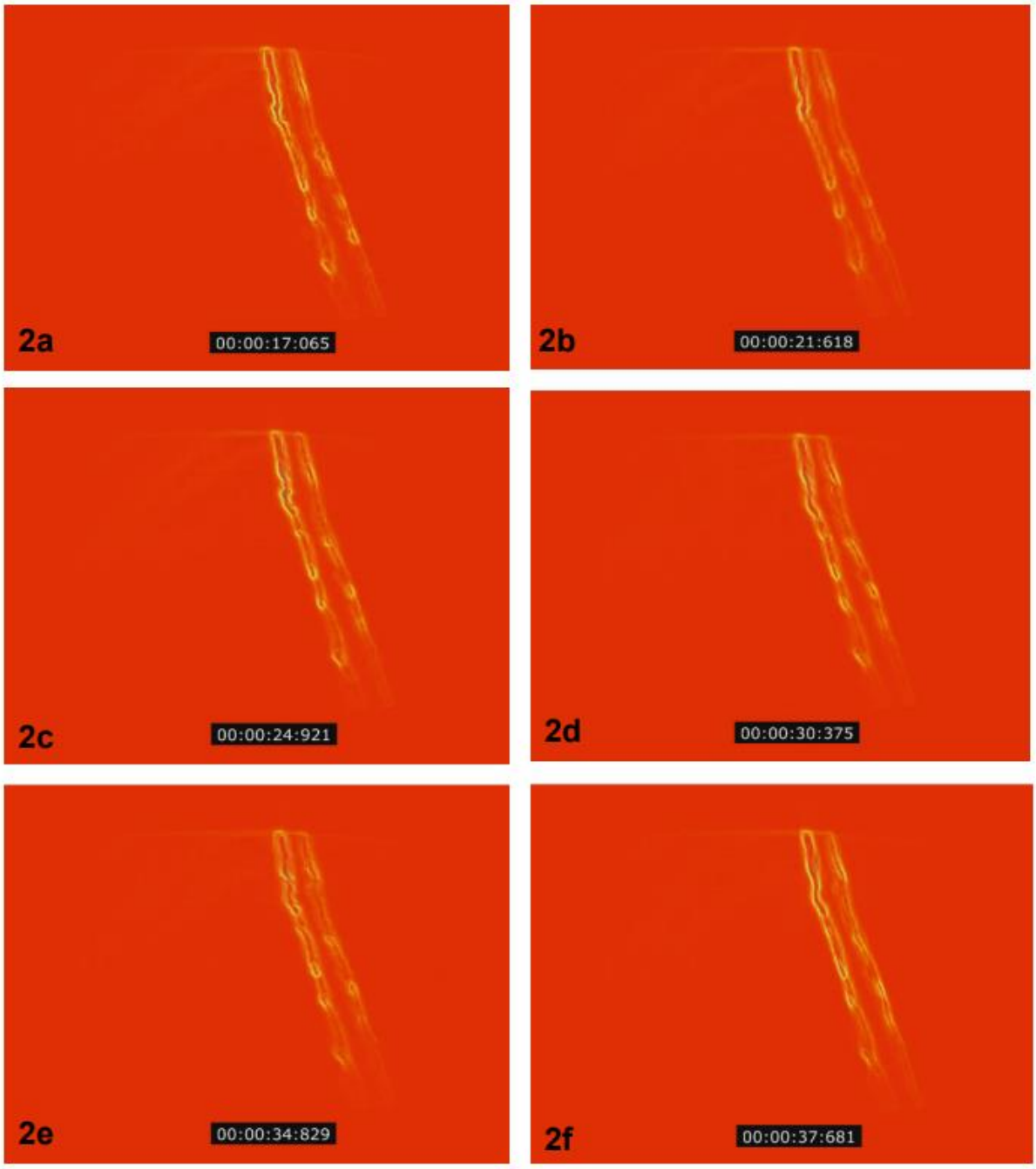

Figure 2. Dynamic images of the electric double layer charge distribution and propagation under the electron beam at 1000x magnification.

Perturbation of the double layer charge often influences the local fiber micromorphology[122].

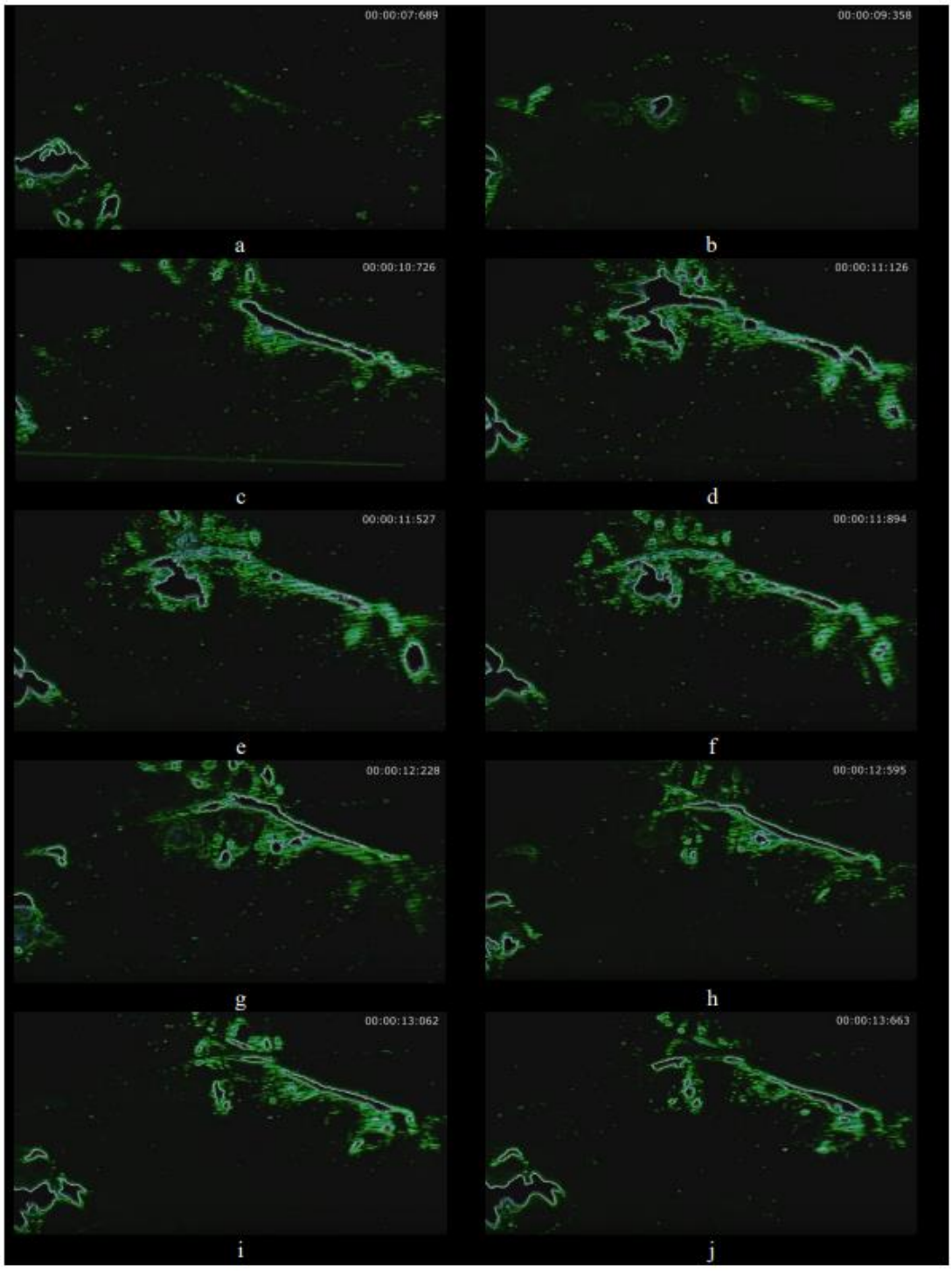

Figure 3. Singular branched fiber with traveling charge waves on the surface (YMD micrographs after Sobel-Feldman operator visualizing isopotential lines of the electron beam induced emission)[129].

Figure 4. Charging isolines (isopotential lines obtained by Sobel filter) colocalized with SEM maps[129].

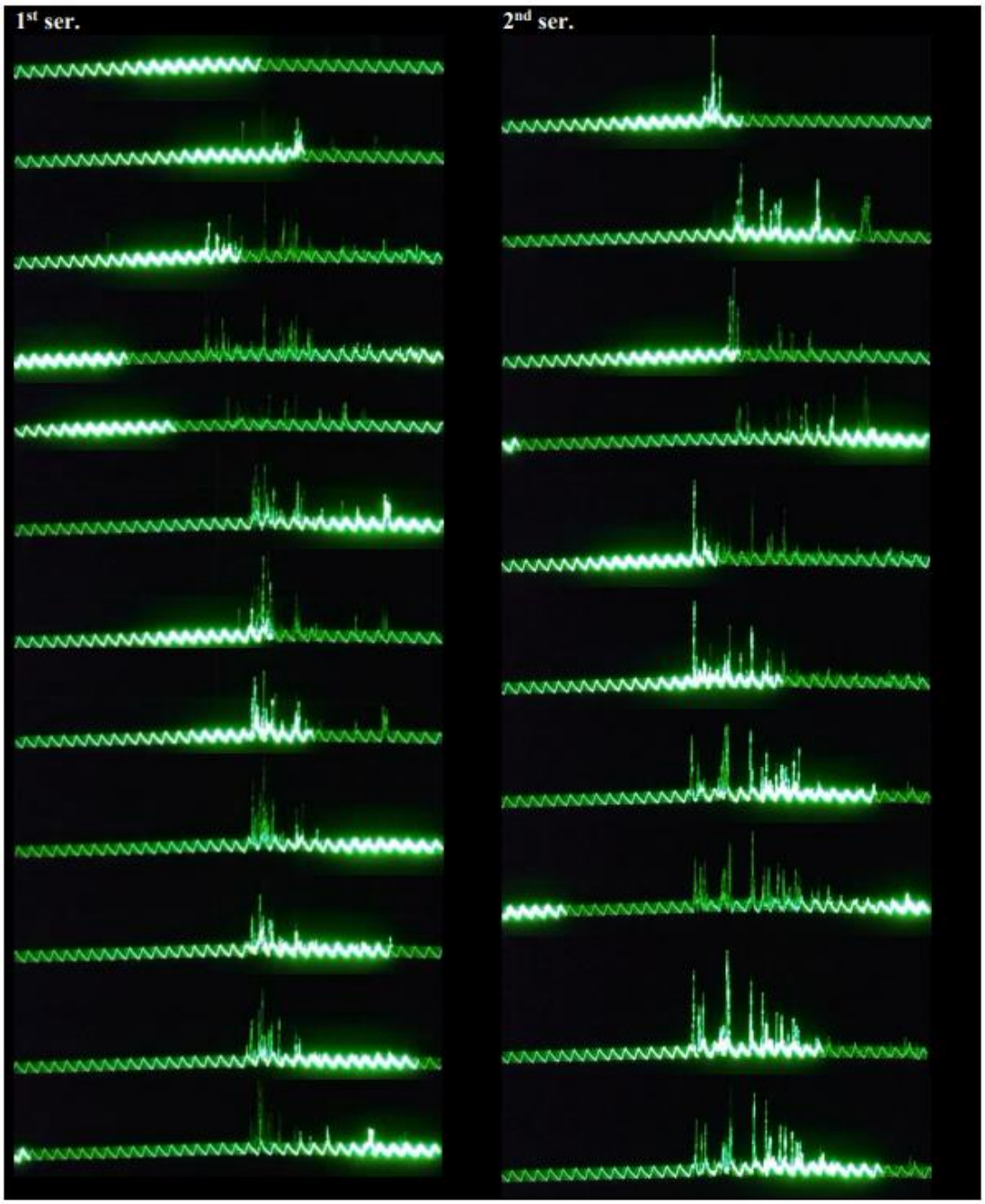

Figure 5. Oscilloscopic sectioning visualization of the surface charge propagation process performed in YMD-compatible registration mode (Y-modulation and raster carrier wave).

It is the point effect on the acute angle (or "arris") of the fiber sample[129].

Conflict of interest

The authors declare no conflict of interest.

References

1. Nejoh H. Incremental charging of a molecule at room temperature using the scanning tunnelling microscope. *Nature* 1991; 353(6345): 640–642. doi: 10.1038/353640a0
2. Sablikov VA, Polyakov SV, Shchamkhalova BS. Coulomb interaction and charging effects in conductance of mesoscopic quantum wire structures. In: Proceedings of the Physics and Technology International

Symposium [6th]; 22–26 June 1998; Petersburg, Russia. pp. 86–90.
3. Sablikov VA, Polyakov SV, Büttiker M. Charging effects in a quantum wire with leads. *Physical Review B* 2000; 61: 13763–13773. doi: 10.1103/PhysRevB.61.13763
4. Zozulenko I. Charging effects and bistability in resonant quantum wire structures. *Journal of Physics: Condensed Matter* 1994; 6(28): 5507. doi: 10.1088/0953-8984/6/28/023
5. Kouklin N, Menon L, Bandyopadhyay S. Room-temperature single-electron charging in electrochemically synthesized semiconductor quantum dot and wire array. *Applied Physics Letters* 2002; 80: 1649–1651. doi: 10.1063/1.1458683
6. Richter A, Yamaguchi M, Akazaki T, et al. Single-electron charging effects in a semiconductor quantum wire with side-coupled quantum dot. *Japanese Journal of Applied Physics* 2004; 43: 7144. doi: 10.1143/JJAP.43.7144
7. Available online: https://flux.aps.org/meetings/YR03/MAR03/baps/abs/S5470.html#SP27.010 (accessed on 14 September 2023).
8. Emberly EG, Kirczenow G. Multiterminal molecular wire systems: A self-consistent theory and computer simulations of charging and transport. *Physical Review B* 2000; 62(15): 10451. doi: 10.1103/PhysRevB.62.10451
9. Keyes DE, McInnes LC, Woodward C, et al. Multiphysics simulations: Challenges and opportunities. *The International Journal of High Performance Computing Applications* 2013; 27(1): 4–83. doi: 10.1177/109434201246818
10. Michopoulos JG, Farhat C, Fish J. Modeling and simulation of multiphysics systems. *Journal of Computing and Information Science in Engineering* 2005; 5(3): 198–213. doi: 10.1115/1.2031269
11. Emberly EG, Kirczenow G. Charging effects, forces, and conduction in molecular wire systems. *Annals of the New York Academy of Sciences* 2002; 960(1): 131–142. doi: 10.1111/j.1749-6632.2002.tb03028.x
12. Matsukawa T, Kanemaru S, Masahara M, et al. Silicon nanowire memory using surface charging and its operation analysis by scanning Maxwell-stress microcopy (SMM). In: Proceedings of the 2001 International Semiconductor Device Research Symposium. Symposium Proceedings (Cat. No. 01EX497); 5–7 December 2001; Washington, DC, USA. pp. 364–367.
13. Zhang LQ, Liu XH, Liu Y, et al. Controlling the lithiation-induced strain and charging rate in nanowire electrodes by coating. *ACS Nano* 2011; 5(6): 4800–4809. doi: 10.1021/nn200770p
14. Chen MC, Chen HC, Lee TH, et al. Estimating the detection stability of a Si nanowire sensor using an additional charging electrode. In: Proceedings of the 2013 IEEE International Reliability Physics Symposium (IRPS); 14–18 April 2013; Monterey, CA, USA. pp. ME.1.1–ME.1.4.
15. van Kouwen MP, Reimer ME, Hidma AW, et al. Single electron charging in optically active nanowire quantum dots. *Nano Letters* 2010; 10(5): 1817–1822. doi: 10.1021/nl100520r
16. Liu XH, Zhong L, Zhang LQ, et al. Lithium fiber growth on the anode in a nanowire lithium ion battery during charging. *Applied Physics Letters* 2011; 98(18): 183107. doi: 10.1063/1.3585655
17. Zankowski SP, Vanpaemel J, Vereecken PM. Interconnected Ni Nanowire scaffolds for fast-charging 3D thin-film Lithium-Ion batteries. In: Proceedings of the Electrochemical Society Meeting Abstracts MA2016-02; 2–7 October 2016; Honolulu, HI, USA. pp. 459–459.
18. Yin Z, Cho S, You DJ, et al. Copper nanowire/multi-walled carbon nanotube composites as all-nanowire flexible electrode for fast-charging/discharging lithium-ion battery. *Nano Research* 2018; 11: 769–779. doi: 10.1007/s12274-017-1686-0
19. Gao F, Nebel CE. Diamond nanowire forest decorated with nickel hydroxide as a pseudocapacitive material for fast charging-discharging. *Physica Status Solidi (a)* 2015; 212(11): 2533–2538. doi: 10.1002/pssa.201532131
20. Mirvakili SM, Hunter IW. Vertically aligned niobium nanowire arrays for fast-charging micro-supercapacitors. *Advanced Materials* 2017; 29(27): 1700671. doi: 10.1002/adma.201700671
21. Liu R, Wang J, Sun T, et al. Silicon nanowire/polymer hybrid solar cell-supercapacitor: A self-charging power unit with a total efficiency of 10.5%. *Nano Letters* 2017; 17(7): 4240–4247. doi: 10.1021/acs.nanolett.7b01154
22. Liu H, Li M, Kaner RB, et al. Monolithically integrated self-charging power pack consisting of a silicon nanowire array/conductive polymer hybrid solar cell and a laser-scribed graphene supercapacitor. *ACS Applied Materials & Interfaces* 2018; 10(18): 15609–15615. doi: 10.1021/acsami.8b00014
23. Quiroga-González E, Carstensen J, Föll H. Structural and electrochemical investigation during the first charging cycles of silicon microwire array anodes for high capacity lithium ion batteries. *Materials* 2013; 6(2): 626–636. doi: 10.3390/ma6020626
24. Quiroga-González E, Carstensen J, Föll H. Optimal conditions for fast charging and long cycling stability of silicon microwire anodes for lithium ion batteries, and comparison with the performance of other Si anode concepts. *Energies* 2013; 6(10): 5145–5156. doi: 10.3390/en6105145
25. Cheng ZH, Koyama H, Kimura Y, et al. Modeling of local dielectric charging induced by line scan during SEM observation. *Journal of Vacuum Science & Technology B* 2015; 33(6): 06FL02. doi: 10.1116/1.4936069
26. Arat KT, Klimpel T, Hagen CW. Model improvements to simulate charging in scanning electron microscope.

Journal of Micro/Nanolithography, MEMS, and MOEMS 2019; 18(4): 044003. doi: 10.1117/1.JMM.18.4.044003
27. Villarrubia JS. Modeling scanning electron microscope measurements with charging. In: Proceedings of the Frontiers of Characterization and Metrology for Nanoelectronics; 25–28 March 2013; Gaithersburg, MD.
28. Curtis GH, Ferrier RP. The electric charging of electron-microscope specimens. *Journal of Physics D: Applied Physics* 1969; 2(7): 1035. doi: 10.1088/0022-3727/2/7/312
29. Shaffner TJ, Van Veld RD. 'Charging' effects in the scanning electron microscope. *Journal of Physics E: Scientific Instruments* 1971; 4: 633. doi: 10.1088/0022-3735/4/9/002
30. Pawley JB. Charging artifacts in the scanning electron microscope (Japenese). *Scanning Electron Microscopy* 1972; Part Ⅰ: 153–160.
31. Robinson VNE. The elimination of charging artefacts in the scanning electron microscope. *Journal of Physics E: Scientific Instruments* 1975; 8: 638. doi: 10.1088/0022-3735/8/8/009
32. Okai N, Sohda Y. Study on image drift induced by charging during observation by scanning electron microscope. *Japanese Journal of Applied Physics* 2012; 51: 06FB11. doi: 10.1143/JJAP.51.06FB11
33. Miller DJ. Artifacts of specimen charging in X-ray microanalysis in the scanning electron microscope. *Ultramicroscopy* 1991; 35(3–4): 357–366. doi: 10.1016/0304-3991(91)90088-N
34. Le Berre JF, Gauvin R, Demopoulos GP. Charging: A limitation to perform X-ray microanalysis in the variable pressure scanning electron microscope. *Microscopy and Microanalysis* 2005; 11(S02): 410–411. doi: 10.1017/S1431927605502757
35. Lee KW. *Reduction of Charging Effects Using Pseudo-Random Scanning in the Scanning Electron Microscope* [PhD thesis]. National University of Singapore; 2000.
36. Thong JTL, Lee KW, Wong WK. Reduction of charging effects using vector scanning in the scanning electron microscope. *Scanning* 2001; 23(6): 395–402. doi: 10.1002/sca.4950230606
37. Wan Ismail WZ, Sim KS, Tso CP, Ting HY. Reducing charging effects in scanning electron microscope images by Rayleigh contrast stretching method (RCS). *Scanning* 2011; 33(4): 233–251. doi: 10.1002/sca.20237
38. Wong WK, Thong JTL, Phang JCH. Charging identification and compensation in the scanning electron microscope. In: Proceedings of the 1997 6th International Symposium on the Physical and Failure Analysis of Integrated Circuits; 25 July 1997; Singapore. pp. 97–102.
39. Saparin GV, Spivak GV. Observation of the process of surface charging of dielectrics by means of a scanning electron microscope (Russian). *Bulletin of the Russian Academy of Sciences: Physics* 1966; 30: 816–818.
40. Hieber H, Erdmann-Jesnitzer F. Electron-microscope and magnetic examination of the formation of cleavage cracks in low-C Fe after electrolytic charging with H (German). *Arch Eisnhuttenwesen* 1971; 42(5): 359–364.
41. Kokhanchik LS. Use of the effects of specimen charging in diagnosing dielectric inhomogeneities in lithium niobate films in a scanning electron microscope. *Industrial Laboratory* 1995; 61(6): 339–341.
42. Rondot S, Jbara O, Fakhfakh S, et al. Effect of surface mechanical finishes on charging ability of electron irradiated PMMA in a scanning electron microscope. *Nuclear Instruments and Methods in Physics Research Section B: Beam Interactions with Materials and Atoms* 2011; 269(19): 2117–2123. doi: 10.1016/j.nimb.2011.07.001
43. Bradley GF. *Electron Beam Charging of Polymers in A Scanning Electron Microscope* [PhD thesis]. University of Tennessee, Knoxville; 1992.
44. Blaise G, Braga D. Investigation of insulator charging properties with a scanning electron microscope: Dose and current density effects. *Physical Chemistry News* 2003; 10: 1–4.
45. Rau EI, Tatarintsev AA, Kupreenko SY, et al. Comparative analysis of methods for measurement of the surface potential of dielectrics charging under electron-beam irradiation in a scanning electron microscope. *Journal of Surface Investigation: X-ray, Synchrotron and Neutron Techniques* 2017; 11: 1062–1068. doi: 10.1134/S1027451017050354
46. Campbell ER, Reisner JH, Chung KT. Charging phenomenon in conductor-insulator composites as displayed by the scanning electron microscope. *Journal of Applied Physics* 1983; 54(2): 1133–1134. doi: 10.1063/1.332132
47. Barkay Z, Dwir B, Deutscher G, Grünbaum E. Electrical charging of percolating samples in the scanning electron microscope. *Applied Physics Letters* 1989; 55(26): 2787–2789. doi: 10.1063/1.101909
48. Le Bihan R, Boudjema EH. Study of the charging of TGS crystals during direct observation in a scanning electron microscope. *Ferroelectrics* 1988; 81(1): 119–122. doi: 10.1080/00150198808008825
49. Dremova NN, Erko AI, Roshchupkin DV. Charging mechanism for the formation of a metastable surface-acoustic-wave potential contrast observed in a scanning electron microscope. *Technical Physics* 1988; 33: 1066–1068.
50. Tan YY, Sim KS, Tso CP. A study on central moments of the histograms from scanning electron microscope charging images. *Scanning* 2007; 29(5): 211–218. doi: 10.1002/sca.20065
51. Koike T, Ikeda T, Miyoshi M, et al. Accuracy of overlay metrology with nonp-enetrating and negative-charging electron beam of the scanning electron microscope. *Japanese Journal of Applied Physics* 2002; 41: 915. doi: 10.1143/JJAP.41.915
52. Miyoshi M, Ura K. Negative charging-up contrast formation of multilayered structures with a nonpenetrating

electron beam in scanning-electron microscope. *Journal of Vacuum Science & Technology B: Microelectronics and Nanometer Structures Processing, Measurement, and Phenomena* 2005; 23(6): 2763–2768. doi: 10.1116/1.2101757
53. Singh HP, Sekhon SS. Conductivity behaviour of proton conducting polymer gel electrolytes with PVdF-HFP. *European Polymer Journal* 2003; 39(1): 93–98. doi: 10.1016/S0014-3057(02)00172-6
54. Yang Y, Shi Z, Holdcroft S. Synthesis of sulfonated polysulfone-b lock-PVDF copolymers: enhancement of proton conductivity in low ion exchange capacity membranes. *Macromolecules* 2004; 37(5): 1678–1681. doi: 10.1021/ma035659e
55. Ju YW, Lee YH, Kim C, et al. Preparation and proton conductivity of sulfonated-(PVDF-hfp/SEBS) composite membrane. *Applied Chemistry* 2004; 8: 510–513.
56. Shen J, Qiu X, Li Y, et al. Effect of alkaline treatment of PVDF membranes on preparation of proton exchange membranes with high conductivity. *Acta Chimica Sinica* 2005; 63(13): 1187–1192.
57. Sinirlioglu D, Muftuoglu AE, Golcuk K, Bozkurt A. Investigation of proton conductivity of anhydrous proton exchange membranes prepared via grafting vinyltriazole onto alkaline-treated PVDF. *Journal of Polymer Science Part A: Polymer Chemistry* 2014; 52(13): 1885–1897. doi: 10.1002/pola.27197
58. Sinirlioglu D, Muftuoglu AE. Investigation of proton conductivity of PVDF based anhydrous proton exchange membranes (PEMs) obtained via a facile "Grafting Through" strategy. *Journal of Polymer Research* 2015; 22: 232. doi: 10.1007/s10965-015-0868-2
59. Sadeghi S, Şanlı LI, Güler E, Gürsel SA. Enhancing proton conductivity via sub-micron structures in proton conducting membranes originating from sulfonated PVDF powder by radiation-induced grafting. *Solid State Ionics* 2018; 314: 66–73. doi: 10.1016/j.ssi.2017.11.017
60. Ahmadian-Alam L, Mahdavi H. Preparation and characterization of PVDF-based blend membranes as polymer electrolyte membranes in fuel cells: Study of factor affecting the proton conductivity behavior. *Polymers for Advanced Technologies* 2018; 29(8): 2287–2299. doi: 10.1002/pat.4340
61. Sun L, Gu Q, Wang H, et al. Anhydrous proton conductivity of electrospun phosphoric acid-doped PVP-PVDF nanofibers and composite membranes containing MOF fillers. *RSC Advances* 2021; 11(47): 29527–29536. doi: 10.1039/D1RA04307B
62. Rath R, Kumar P, Rana D, et al. Sulfonated PVDF nanocomposite membranes tailored with graphene oxide nanoparticles: Improved proton conductivity and membrane selectivity thereof. *Journal of Materials Science* 2022; 57: 3565–3585. doi: 10.1007/s10853-021-06803-3
63. Gradov OV, Gradova MA, Kholuiskaya SN, Olkhov AA. Electron plasma charging effects on the biocompatible electrospun dielectric fibers. *IEEE Transactions on Plasma Science* 2021; 50(1): 178–186. doi: 10.1109/TPS.2021.3130854
64. Shahravan A, Lucas C, Matsoukas T. Nanowire charging in collisionless plasma. *Journal of Applied Physics* 2010; 108(8): 083303. doi: 10.1063/1.3483300
65. Simpson JA, Rabinowitz D, Tuzzolino AJ. Cosmic dust investigations: I. PVDF detector signal dependence on mass and velocity for penetrating particles. *Nuclear Instruments and Methods in Physics Research Section A: Accelerators, Spectrometers, Detectors and Associated Equipment* 1989; 279(3): 611–624. doi: 10.1016/0168-9002(89)91311-9
66. Simpson JA, Tuzzolino AJ. Cosmic dust investigations: II. Instruments for measurement of particle trajectory, velocity and mass. *Nuclear Instruments and Methods in Physics Research Section A: Accelerators, Spectrometers, Detectors and Associated Equipment* 1989; 279(3): 625–639. doi: 10.1016/0168-9002(89)91312-0
67. Simpson JA, Tuzzolino AJ. Polarized polymer films as electronic pulse detectors of cosmic dust particles. *Nuclear Instruments and Methods in Physics Research Section A: Accelerators, Spectrometers, Detectors and Associated Equipment* 1985; 236(1): 187–202. doi: 10.1016/0168-9002(85)90145-7
68. Tuzzolino AJ. Applications of PVDF dust sensor systems in space. *Advances in Space Research* 1996; 17(12): 123–132. doi: 10.1016/0273-1177(95)00769-B
69. Shu A, Bugiel S, Grün E, et al. Cratering studies in polyvinylidene fluoride (PVDF) thin films. *Planetary and Space Science* 2013; 89: 29–35. doi: 10.1016/j.pss.2013.05.001
70. Jones GD, Assink RA, Dargaville TR, et al. *Characterization, Performance and Optimization of PVDF as A Piezoelectric Film for Advanced Space Mirror Concepts.* Sandia National Laboratories; 2005.
71. Dargaville TR, Celina M, Martin JW, Banks BA. Evaluation of piezoelectric PVDF polymers for use in space environments. II. Effects of atomic oxygen and vacuum UV exposure. *Journal of Polymer Science Part B: Polymer Physics* 2005; 43(18): 2503–2513. doi: 10.1002/polb.20549
72. Dargaville TR, Elliott JM, Celina M. Evaluation of piezoelectric PVDF polymers for use in space environments. III. Comparison of the effects of vacuum UV and gamma radiation. *Journal of Polymer Science Part B: Polymer Physics* 2006; 44(22): 3253–3264. doi: 10.1002/polb.20966
73. Celina MC, Dargaville TR, Chaplya PM, Clough RL. Piezoelectric PVDF materials performance and operation limits in space environments. *MRS Online Proceedings Library (OPL)* 2004; 851: NN9.11. doi: 10.1557/PROC-851-NN9.11

74. Bai Y, Xiao C, Wei Z, Yin L. Study on structure health monitoring method of space vehicle based on PVDF piezoelectric film. *Journal of Physics: Conference Series* 2023; 2479: 012022. doi: 10.1088/1742-6596/2479/1/012022
75. Ivanov NN, Ivanov AN. A sensor for the spatial registration and measurement of particles parameters in near and deep space—Experimental investigation of SiO_2-aerogel characteristics. *Solar System Research* 2014; 48: 549–554. doi: 10.1134/S0038094614070090
76. Dargaville T, Celina M, Chaplya P, Assink R. Evaluation of piezoelectric PVDF polymers for use in space environments. In: Proceedings of the 45th AIAA/ASME/ASCE/AHS/ASC Structures, Structural Dynamics & Materials Conference; 19–22 April 2004; Palm Springs, California, USA. p. 1547.
77. Balmain KG. Charging of spacecraft materials simulated in a scanning electron microscope. *Electronics Letters* 1973; 9(23): 544–546. doi: 10.1049/el:19730401
78. Czeremuszkin G, Latreche M, Wertheimer MR. Charging/discharge events in coated spacecraft polymers during electron beam irradiation in a scanning electron microscope. *Nuclear Instruments and Methods in Physics Research Section B: Beam Interactions with Materials and Atoms* 2001; 185(1–4): 88–99. doi: 10.1016/S0168-583X(01)00836-9
79. Quan X, Ji Y, Zhang H, et al. Charging compensation of alumina samples by using an oxygen microinjector in the environmental scanning electron microscope. *Scanning* 2006; 28(5): 289–293. doi: 10.1002/sca.4950280508
80. Wan D, Deng Y, Meling JIH, et al. Hydrogen-enhanced fatigue crack growth in a single-edge notched tensile specimen under in-situ hydrogen charging inside an environmental scanning electron microscope. *Acta Materialia* 2019; 170: 87–99. doi: 10.1016/j.actamat.2019.03.032
81. Brink J, Sherman M, Berriman J, Chiu W. Charging phenomena observed on biological specimens in a 400-KV electron cryo-microscope. In: Proceedings of the 52nd Annual Meeting of the Microscopy Society of America; 31 July–5 August 1994; New Orleans, LA, USA. pp. 118–119.
82. Le Berre JF, Demers H, Demopoulos GP, Gauvin R. Examples of charging effects on the spectral quality of X-ray microanalysis on a glass sample using the variable pressure scanning electron microscope. *Scanning* 2007; 29(6): 270–279. doi: 10.1002/sca.20071
83. Le Berre JF, Demopoulos G, Gauvin R. Charging effects on the spectral quality of X-ray microanalysis using the variable pressure scanning electron microscope. *Microscopy and Microanalysis* 2007; 13(S02): 1478–1479. doi: 10.1017/S1431927607073849
84. Marcinko T. Technique for controlling surface charging of plastic and ceramic IC packages in the scanning electron microscope by the use of topical antistats. In: Electrical Overstress/Electrostatic Discharge Symposium Proceedings (EOS-14); 16–18 September 1992; Dallas, TX, USA. p. 5.
85. Brunner M, Schmid R. Charging effects in low-voltage scanning electron microscope metrology. *Scanning Electron Microscopy* 1986; (2): 377–382.
86. Zobačová J, Frank L. Specimen charging and detection of signal from non-conductors in a cathode lens-equipped scanning electron microscope. *Scanning* 2003; 25(3): 150–156. doi: 10.1002/sca.4950250307
87. Emerson L, Cox G. Charging artefacts in atomic force microscopy. *Micron* 1994; 25(3): 267–269. doi: 10.1016/0968-4328(94)90032-9
88. Boer EA, Bell LD, Brongersma ML, et al. Charging of single Si nanocrystals by atomic force microscopy. *Applied Physics Letters* 2001; 78: 3133–3135.
89. Nahum E, Ebenstein Y, Aharoni A, et al. Transport and charging in single semiconductor nanocrystals studied by conductance atomic force microscopy. *Nano Letters* 2004; 4(1): 103–108. doi: 10.1021/nl034928b
90. Pang CL, Ashworth TV, Raza H, et al. A non-contact atomic force microscopy and 'force spectroscopy' study of charging on oxide surfaces. *Nanotechnology* 2004; 15(7): 862. doi: 10.1088/0957-4484/15/7/027
91. Zaghloul U, Papaioannou GJ, Bhushan B, et al. Effect of deposition gas ratio, RF power, and substrate temperature on the charging/discharging processes in PECVD silicon nitride films for electrostatic NEMS/MEMS reliability using atomic force microscopy. *Journal of Microelectromechanical Systems* 2011; 20(6): 1395–1418. doi: 10.1109/JMEMS.2011.2167670
92. Cui XD, Zarate X, Tomfohr J, et al. Bias-induced forces in conducting atomic force microscopy and contact charging of organic monolayers. *Ultramicroscopy* 2002; 92(2): 67–76. doi: 10.1016/s0304-3991(02)00069-4
93. Tivanski AV, Walker GC. Ferrocenylundecanethiol self-assembled monolayer charging correlates with negative differential resistance measured by conducting probe atomic force microscopy. *Journal of the American Chemical Society* 2005; 127(20): 7647–7653. doi: 10.1021/ja0514491
94. Reagan MA, Kashyn D, Juhl S, et al. Electric charging and nanostructure formation in polymeric films using combined amplitude-modulated atomic force microscopy-assisted electrostatic nanolithography and electric force microscopy. *Applied Physics Letters* 2008; 93(3): 033109. doi: 10.1063/1.2957985
95. Mirkowska M, Kratzer M, Teichert C, Flachberger H. The contact charging of insulators by atomic force microscopy. In: Proceedings of the 62nd Annual Meeting of the Austrian Physical Society; 18–21 September

2012; Graz, Austria. p. 171.
96. Bunker MJ, Davies MC, James MB, Roberts CJ. Direct observation of single particle electrostatic charging by atomic force microscopy. *Pharmaceutical Research* 2007; 24(6): 1165–1169. doi: 10.1007/s11095-006-9230-z
97. Chotsuwan C, Blackstock SC. Single molecule charging by atomic force microscopy. *Journal of the American Chemical Society* 2008; 130(38): 12556–12557. doi: 10.1021/ja802419y
98. Fatayer S, Schuler B, Steurer W, et al. Reorganization energy upon charging a single molecule on an insulator measured by atomic force microscopy. *Nature Nanotechnology* 2018; 13(5): 376–380. doi: 10.1038/s41565-018-0087-1
99. Kocic N, Weiderer P, Keller S, et al. Periodic charging of individual molecules coupled to the motion of an atomic force microscopy tip. *Nano Letters* 2015; 15(7): 4406–4411. doi: 10.1021/acs.nanolett.5b00711
100. Otobe M, Yajima H, Oda S. Observation of the single electron charging effect in nanocrystalline silicon at room temperature using atomic force microscopy. *Applied Physics Letters* 1998; 72(9): 1089–1091. doi: 10.1063/1.120973
101. Stomp R, Miyahara Y, Schaer S, et al. Detection of single-electron charging in an individual InAs quantum dot by noncontact atomic-force microscopy. *Physical Review Letters* 2005; 94(5): 56802. doi: 10.1103/PhysRevLett.94.056802
102. Tekiel A. *Ultra-high Vacuum Fabrication of Nanoscale Systems for Studying Single-electron Charging by Room-temperature Atomic Force Microscopy* [PhD thesis]. McGill University Libraries; 2013.
103. Roy-Gobeil A. *Single-electron Charging Using Atomic Force Microscopy* [PhD thesis]. McGill University Libraries; 2017.
104. Ellis SG. Specimen charging in the electron microscope and some observations on the size of polystyrene latex particles. *Journal of Applied Physics* 1952; 23(7): 728–732. doi: 10.1063/1.1702291
105. Jachowicz J, Garcia M, Wis-Surel G. Relationship between triboelectric charging and surface modification of human hair. *Journal of the Society of Cosmetic Chemists* 1984; 35(6): 339–340.
106. Jachowicz J, Garcia M, Wis-Surel G. Relationship between triboelectric charging and surface. *Journal of the Society of Cosmetic Chemists* 1985; 36: 189–212.
107. Jachowicz J, Garcia M, Wis-Surel G. Relationship between triboelectric charging and surface modification of human hair: Polymeric versus monomeric long alkyl chain quaternary ammonium salts. *Textile Research Journal* 1987; 57(9): 543–548. doi: 10.1177/004051758705700910
108. Seshadri IP, Bhushan B. Effect of rubbing load on nanoscale charging characteristics of human hair characterized by AFM based Kelvin probe. *Journal of Colloid and Interface Science* 2008; 325(2): 580–587. doi: 10.1016/j.jcis.2008.06.015
109. Walter M. *In-situ Tensile Deformation and Surface Charging Characterization of Human Hair with Atomic Force Microscopy* [PhD thesis]. Ohio State University; 2008.
110. Stephenson LE, Wollkind DJ. Weakly nonlinear stability analyses of one-dimensional Turing pattern formation in activator-inhibitor/immobilizer model systems. *Journal of Mathematical Biology* 1995; 33: 771–815. doi: 10.1007/BF00187282
111. Henry BI, Langlands TAM, Wearne SL. Turing pattern formation in fractional activator-inhibitor systems. *Physical Review E* 2005; 72(2): 026101. doi: 10.1103/PhysRevE.72.026101
112. Nakao H, Mikhailov AS. Turing patterns in network-organized activator-inhibitor systems. *Nature Physics* 2010; 6(7): 544–550. doi: 10.1038/nphys1651
113. Hata S, Nakao H, Mikhailov AS. Global feedback control of Turing patterns in network-organized activator-inhibitor systems. *Europhysics Letters* 2012; 98: 64004. doi: 10.1209/0295-5075/98/64004
114. Zhang L, Tian C. Turing pattern dynamics in an activator-inhibitor system with superdiffusion. *Physical Review E: Statistical, Nonlinear, and Soft Matter Physics* 2014; 90(6): 062915. doi: 10.1103/PhysRevE.90.062915
115. dos S. Silva FA, Viana RL, Lopes SR. Pattern formation and Turing instability in an activator-inhibitor system with power-law coupling. *Physica A: Statistical Mechanics and its Applications* 2015; 419: 487–497. doi: 10.1016/j.physa.2014.09.059
116. Wu R, Zhou Y, Shao Y, Chen L. Bifurcation and Turing patterns of reaction-diffusion activator-inhibitor model. *Physica A: Statistical Mechanics and its Applications* 2017; 482: 597–610. doi: 10.1016/j.physa.2017.04.053
117. Wang J, Li Y, Hou X. Supercritical Hopf bifurcation and Turing patterns for an activator and inhibitor model with different sources. *Advances in Difference Equations* 2018; 2018(1): 241. doi: 10.1186/s13662-018-1697-5
118. Talukdar D, Dutta K. Decaying localized structures beyond Turing space in an activator-inhibitor system. *The European Physical Journal Plus* 2020; 135(1): 53. doi: 10.1140/epjp/s13360-019-00063-6
119. Yochelis A. The nonlinear initiation of side-branching by activator-inhibitor-substrate (Turing) morphogenesis. *Chaos* 2021; 31(5): 051102. doi: 10.1063/5.0050630
120. Kato Y, Nakao H. Turing instability in quantum activator-inhibitor systems. *Scientific Reports* 2022; 12(1): 15573. doi: 10.1038/s41598-022-19010-0
121. Kato Y, Nakao H. Turing instability of activator-inhibitor units in open quantum systems. *Bulletin of the*

American Physical Society 2023; in press.
122. Gradov OV, Gradova MA, Iordanskii AL, et al. Isopotential mapping of electron beam induced dielectric charging of the PHB nonwoven fabric structures using sobel-feldman gradient operator. In: Proceedings of the 2020 7th International Congress on Energy Fluxes and Radiation Effects (EFRE); 14–26 September 2020; Tomsk, Russia. pp. 662–665.
123. Gradov OV, Gradova MA, Maklakova IA, Kholuiskaya SN. Towards electron-beam-driven soft/polymer fiber microrobotics for vacuum conditions. *Materials Research Proceedings* 2022; 21: 370–383. doi: 10.21741/9781644901755-64
124. Adamoviz ED, Buryanskaya E, Gradov O. Membrane-mimetic proton-exchange structures as components of complex scaffolds with metastable nanochannels (Russian). *Genes and Cells* 2022; 17(3): 9. doi: 10.23868/gc121899
125. Kochervinskii VV, Gradov OV, Gradova MA. Fluorine-containing ferroelectric polymers: applications in engineering and biomedicine. *Russian Chemical Reviews* 2022; 91(11): RCR5037. doi: 10.57634/RCR5037
126. Gradov O, Gradova M, Kochervinskii V. Biocompatible biomimetic polymer structures with an active response for implantology and regenerative medicine Part I. Basic principles of the active implant's biocompatibility. *Siberian Journal of Life Sciences and Agriculture* 2023; 15(1): 346-377. doi: 10.12731/2658-6649-2023-15-1-346-377
127. Gradov OV, Gradova MA, Kochervinskii VV. Biomimetic biocompatible ferroelectric polymer materials with an active response for implantology and regenerative medicine. In: *Organic Ferroelectric Materials and Applications.* Elsevier; 2022. pp. 571–619.
128. Bur'yanskaya EL, Gradov OV, Gradova MA, et al. Biomedical applications of ferroelectric polymers based on vinylidene fluoride in regenerative medicine (Russian). *Genes and Cells* 2022; 17(3): 39. doi: 10.23868/gc122163
129. Gradov OV, Gradova MA, Olkhov AA, Iordanskiy AL. Charge propagation along the polymer fiber of polyhydroxybutyrate: Is it possible to apply the cable model? *Key Engineering Materials* 2020; 869: 246–258. doi: 10.4028/www.scientific.net/KEM.869.246
130. Dubljevic S. Constraints-driven optimal actuation policies for diffusion-reaction processes with collocated actuators and sensors. *Industrial & Engineering Chemistry Research* 2008; 47(1): 105–115. doi: 10.1021/ie070546v
131. Li J, Wu Z, Wen C. Adaptive stabilization for a reaction-diffusion equation with uncertain nonlinear actuator dynamics. *Automatica* 2021; 128: 109594. doi: 10.1016/j.automatica.2021.109594
132. Zhang XW, Wu HN, Wang JL, et al. Membership-function-dependent fuzzy control of reaction-diffusion memristive neural networks with a finite number of actuators and sensors. *Neurocomputing* 2022; 514: 94–100. doi: 10.1016/j.neucom.2022.09.126
133. Buryanskaya EL, Gradov OV, Gradova MA, et al. Time-resolved multifractal analysis of electron beam induced piezoelectric polymer fiber dynamics: Towards multiscale thread-based microfluidics or acoustofludics. In: Altenbach H, Bruno G, Eremeyev VA, et al. (editors). *Mechanics of Heterogeneous Materials.* Springer, Cham; 2023. Volume 195. pp. 35–58.

Academic Publishing Pte. Ltd.

Add: 73 Upper Paya Lebar Road #07-02B-01 Centro Bianco Singapore 534818

Tel: +65 83184869

E-mail: editorial_office@acad-pub.com

Web: http://ojs.acad-pub.com/